The Dissertation Committee for Xiaoyu Wu
Certifies that this is the approved version of the following dissertation:

Development and Applications of Microwave Impedance Microscopy for Imaging Emergent Properties in Quantum Materials

APPROVED BY
SUPERVISING COMMITTEE:

Keji Lai, Supervisor

Alex de Lozanne

Alexander A. Demkov

Chih-Kang Shih

Jianshi Zhou

Development and Applications of Microwave Impedance Microscopy for Imaging Emergent Properties in Quantum Materials

by

Xiaoyu Wu

Dissertation

Presented to the Faculty of the Graduate School of

The University of Texas at Austin

in Partial Fulfillment

of the Requirements

for the Degree of

Doctor of Philosophy

The University of Texas at Austin

May 2018

To my parents, Xiao Wu and Qi Zhou

For their constant support in my life and my career.

To my wife, Cheng Xue

For her love, support, patience, laughter, and being in my life.

To my son, Abel Yi-Ming Wu

Welcome to this wonderful world! Happy exploring!

Acknowledgements

"Why does it thunder and rain? Why are there winter and summer? Nature lay hid in mist. Its law is elegant but never simple." These are the lyrics from a song I learned when I was a kid and even today I sing it to myself whenever I find something amazing in scientific research or daily life. The song demonstrates human being's perpetual curiosity about the marvelous world and always encourages me to pursue the truth. Inspired by such spirit and supported by many people, I chose to be trained as a physicist so that I can master the scientific method to understand the ultimate causes of phenomena. After going through a journey full of excitement and disappointment, confidence and self-doubt, happiness and sadness, now I found myself about to conclude my PhD years and review my humble contributions to human being's understanding of the world.

At this special moment, I would like to thank many important peoples in this memorable experience. The first person I would like to thank is my advisor, Prof. Keji Lai. It is an honor for me to be his first graduate student. He patiently supported me to go through every single phase of scientific research. I was encouraged to start with exploratory experiments, to dig into interesting phenomena through systematic studies, to summarize my findings into graphs and words, and to get my results published. If I got stuck at whatever stage, which happened a lot, I could always reach him for helpful discussion. As we worked closely setting up the lab in UT Austin, Keji has influenced me with not only his knowledge but also his professional style in every detail, from building scientific apparatus, to carrying out research, to communicating results with other researchers. From time to time, I inspect my own work according to his standard as a method to encourage myself.

Many thanks to my colleagues in the Lai's lab. Dr. Yuan Ren and I were the only members in the Lai's group during the first year. He is an experienced physicist and my experience with hardware programming started with his guidance. Thanks to other members Dr. Di Wu, Dr. Lan Luan, Lu Zheng, Zhanzhi Jiang, and Zhaodong Chu for their help in my research at different points and their comments on my work. Thanks to visiting students and scholars, Zhenqi Hao, Zhiran Zhang, He Liu, Yen-Lin Huang, and Xiaodong Zhou for bring in their own expertise.

Thanks to my collaborators. Prof. Sang-Wook Cheong and his group members, Dr. Rongwei Hu and Dr. Kai Du, from Rutgers University keep providing us with high-quality crystalline samples with interesting physics, including hexagonal manganites and ferrites. Prof. Jeremy Levy and his postdoc, Dr. Guanglei Chen, from University of Pittsburg helped us start the project on writing conductive structures at the interface of LAO and STO. Dr. Hongtao Yuan (now Prof. Yuan at Nanjing University), Prof. Yi Cui, and Prof. Harold Hwang from Stanford University provided us with the ion-gel-gated transistors. Eric Ma and Dr. Yongtao Cui provided helpful suggestion during the setup of my tuning fork-based MIM.

I also want to thank my parents, Xiao Wu and Qi Zhou, for supporting me to pursue a PhD degree. Whenever I feel frustrated in research and in life, they help me restore my inner peace through listening. While I am thousands of miles away from home, they take good care of every family member and let me focus on my research and not worry about issues in life.

I am a lucky man to have my wife, Cheng Xue, being in my life and supporting me all these years. Everything is just better with her beside me: trees are greener, roses are redder, and laughter becomes louder. I vividly remember that, at some point of my PhD, I had to work till late night and she just stayed quietly in my office waiting for me to go

home. She never complained about my experiment schedule and asked for nothing except burgers, fries, and iced Coke on our way home.

My son, Abel Yi-Ming Wu, was born during the last year of my PhD. And I would like to present this dissertation to him as a gift, not in hope that he can understand the specific physics inside, but to inspire him to ask questions about this wonderful world and to enjoy the exciting journey of finding the answers.

Abstract

Development and Applications of Microwave Impedance Microscopy for Imaging Emergent Properties in Quantum Materials

Xiaoyu Wu, Ph.D.

The University of Texas at Austin, 2018

Supervisor: Keji Lai

Near-field scanning microwave microscopy (NSMM) detects local physical properties of materials through electromagnetic interaction between the tip and the sample at a length scale much smaller than the freespace wavelength of the microwave radiation. However, previous implementations of NSMM have suffered from poor resolutions, low sensitivity, and unreliable tip-sample contact conditions.

In this dissertation, I will first briefly review the prior research of NSMM (Chapter 1) and then naturally move on to the main theme — the basic principles and technical details of the recently developed microwave impedance microscope (MIM) (Chapter 2). I will present the development of MIM instrumentation including quantitative measurement with tuning-fork-based probes, broadband impedance microcopy, and implementation in cryogenic environment (Chapter 3), which are utilized in research described in the following chapters. The application of MIM will be demonstrated by a number of scientific studies in two general categories, emergent phenomena at ferroelectric domain walls and electrical inhomogeneity in nanodevices. Chapter 4 describes the discovery of low-energy structural dynamics of ferroelectric domain walls in hexagonal rare-earth manganites (h-

RMnO_3) by broadband impedance microscopy. Chapter 5 includes direct visualization of sketched conductive nanostructures at the $LaAlO_3/SrTiO_3$ heterostructure and nanoscale conductance evolution in ion-gel-gated oxide transistors, demonstrating the capability of MIM to image buried structures. I will conclude the dissertation with a short summary and outlook for the future.

Table of Contents

List of Figures

Chapter 1: Introduction

The ability to see things at smaller scales has always been the dream of human beings. The use of water-filled spheres for magnification dated back to almost the very beginning of human history. The invention of modern compound optical microscope in the 17th century made a huge impact to the scientific community by impressive visualization of biological ultrastructure. However, the maximum resolution of an optical system is limited by diffraction to be $d = \frac{\lambda}{2NA}$, where λ is the wavelength of light and NA is the numerical aperture. To reach higher resolution than optical microscopes, two branches of microscopes were developed — electron microscopes and scanning probe microscopes. The former, including transmission electron microscope (TEM) and scanning electron microscope (SEM), follows principles similar to optical microscopes but replaces photons with electrons, which in turn deliver much higher resolution. The latter, exemplified by scanning tunneling microscope (STM) and atomic force microscope (AFM), generates images by scanning the surface of a sample using an extremely sharp probe whose height is delicately controlled by monitoring the tip-sample interaction. Scientists who invented the above techniques were awarded the Nobel Prize in Physics (1986) in recognition of their contribution pushing the boundary of spatial resolution.

While the diffraction limit is correct for far-field microscopy, it can be surpassed by exploiting the near-field interaction of evanescent waves generated by passing electromagnetic waves through an aperture much smaller than the excitation wavelength. In addition to the enhanced resolution, information about physical properties of a specimen can also be inferred from characteristic near-field interaction, indicating great potential of near-field microscopy in material characterization. The original idea of near-field microscopy was proposed by Synge[1, 2] in 1928 and 1931 in which super resolution can be

achieved by scanning a subwavelength-sized hole in a metal film in close distance of an illuminated sample. Decades after the conception of near-field microscopy, its first implementation was demonstrated at radio frequency where subwavelength apertures are easier to fabricate. The instrument of a microwave magnetic microscope, designed by Soohoo[3] in 1962, could investigate spatial variation of magnetic resonance using a microwave cavity with a small hole exposed to a small section of sample. In 1972, profound impact was made by the work of Ash and Nicholls[4], which nicely imaged the conductivity and dielectric contrast on patterned samples with a resolution of $\lambda/60$ using aperture-confined microwaves 3 cm in wavelength. Although the stability and sensitivity of such a setup was limited by unsatisfactory control of probe-sample separation and large background signal induced by fringing field, essential components of a modern near-field microwave microscopy can already be found in this system: a miniature probe delivering microwave for near-field interaction and a circuit of microwave electronics to detect evanescent microwave after interaction, which carries the information of local physical properties.

Later development of near-field scanning microwave microscope benefits from the advent of SPM and nanofabrication techniques. Measurements with consistent signals were made possible through stable control of tip-sample distance from STM and AFM. Tip-sample interaction can be precisely controlled by carefully designed and fabricated probes. Motivated by appealing applications in material characterization and integrated circuit testing, a wide range of NSMM has been invented, providing unique approaches to a great number of problems that are hard to address by other techniques.

In this chapter, I will briefly review the history of NSMM with an emphasis on probe design, probe-sample interaction, detection electronics and scientific applications. The aim of this review is firstly to give readers a historical perspective of NSMM

instrumentation, secondly to bring readers' attention to most important aspects in the design of a NSMM, and finally to make the context for microwave impedance microscopy (MIM) in the following chapters. The last section will describe the structure of this dissertation, including our development of MIM and applications of this technique in the studies of novel quantum materials.

1.1 Probe Design for Near-field Microwave Microscopy

Performance of a microwave microscope largely relies on the design of its probe. The dimensions and geometry of a probe determine its resolution and sensitivity while the measurable physical properties are decided by the specific probe-sample interaction, or specifically, the distribution of electromagnetic fields around the probe. NSMM probes can be categorized into two branches — broadband and resonant. Broadband probes are essentially waveguides allowing operation at any frequency lower than its cutoff frequency, while resonant probes can be regarded as resonators coupled to probe-sample interaction. Sensitivity is usually higher for resonant probes, but the operation is limited to discrete frequencies (fundamental mode and its higher harmonics). On the other hand, the advantage of broadband probes is that they are naturally compatible with spectroscopy measurements.

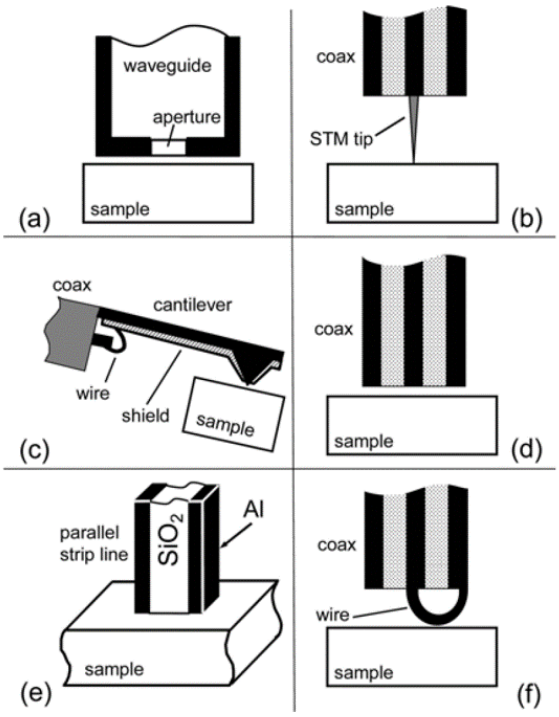

Figure 1.1: Typical probe designs for NSMM. Adapted from Ref. 5.

Probes for NSMM can vary greatly in specific forms and some representative designs are included in Fig. 1.1. Miniature apertures (Fig. 1.1a) are used in early attempts of NSMM[3, 4, 6] to confine the section of tip-sample interaction but they suffer from power loss in the cutoff region. For more efficient energy transmission, probes are based on transmission line structures (Fig. 1.1d) and a tapered apex or an extremely thin cable can be employed to enhance the resolution.[7, 8] As the resolution is presumably determined by the size of the inner conductor, it can be further improved to micrometer or even nanometer scales by attaching a sharpened tip to the center conductor of the transmission line (Fig. 1.1b) which concentrates microwave fields.[9-12] The open-ended probe has a maximized electric field but a minimized magnetic field, ideal for electrical property detection. Different electromagnetic field distribution at the tip apex for probing other properties can

be achieved with different transmission line geometry such as stripline[13-15] (Fig. 1.1e) and shunted center conductor[16, 17] (Fig. 1.1f). Both aperture-based and transmission-line-based probes support a range of operation frequency and thus are broadband probes. For enhanced sensitivity, they can be incorporated into a resonant structure like RLC circuit.[18]

The development of AFM-compatible tips (Fig. 1.1c) is a milestone in the history of NSMM. Near-field interaction strongly depends on probe-sample distance and the sensitivity of NSMM can be significantly enhanced when the probe is brought very close to or even in contact with the sample surface. On the other hand, in a spatially resolved image, signal measured at different locations should be comparable, which also requires stable control of the probe-sample distance. Therefore, it is highly desired to combine localized microwave probes with scanning probe techniques, leading to the vibrant development of AFM-compatible probes. As the conducting metal (cantilever) is brought close to the sample during scan, shielding is required to minimize the parasitic coupling capacitance between the cantilever and the sample, which induces large background noise for NSMM measurements.[19] Due to its complex geometry, AFM-compatible tips cannot cover a continuous range of operation frequency and have to be implemented in a resonant circuit.

1.2 Modeling of Tip-sample Interaction

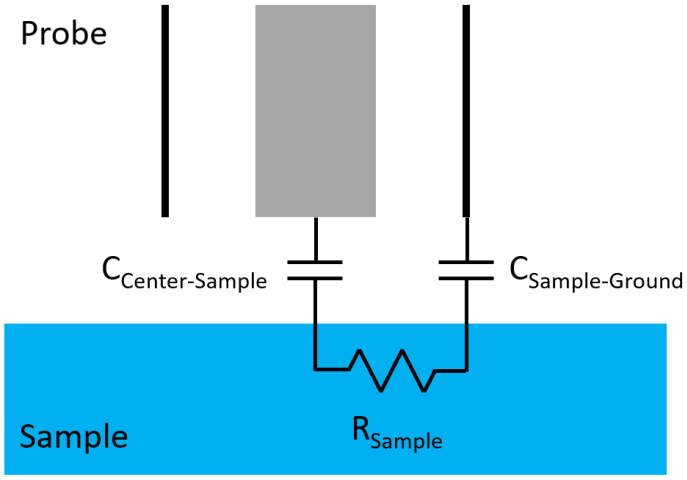

Figure 1.2: Tip-sample interaction modeled as lumped elements.

Regardless of specific probe designs, the tip-sample interaction can be modeled as an interconnection of lumped elements such as capacitor, resistor, and inductor whose values and equivalent circuit are determined by local physical properties and detailed probe geometry. For example, in Fig.1.2 the probe is capacitively coupled to the sample while the sample itself can be characterized by its local resistance.[18] Therefore, the total tip-sample interaction can be represented by two capacitors and one resistor in series with a total impedance $Z_{\text{tip-sample}} = \frac{1}{i\omega C_{\text{Center-Sample}}} + R_{\text{Sample}} + \frac{1}{i\omega C_{\text{Sample-Ground}}}$. Spatial variation of sample properties will influence $Z_{\text{tip-sample}}$ or the admittance of tip-sample interaction ($Y_{\text{tip-sample}} = 1/Z_{\text{tip-sample}}$), giving rise to change of microwave signals monitored by the probe.

As is well known in classical electromagnetic theory, when the length scale of near-field interaction between tip and sample is much smaller than the wavelength of microwave, the electromagnetic field can be treated as quasi-static[20], which greatly simplifies analysis. Specifically, $Z_{\text{tip-sample}}$ or $Y_{\text{tip-sample}}$ can be calculated either analytically or using Finite Element Analysis (FEA) method.

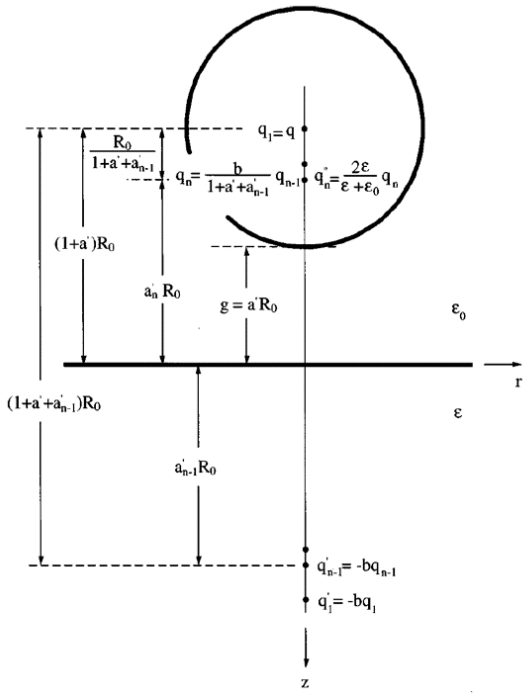

Figure 1.3: Analytical analysis of field distribution between a spherical tip and a dielectric sample. Adapted from Ref. 21.

Analytical calculation is usually based on assumptions of simplified probe geometry like spheres and analytical expression of field distribution are only available for specific ideal samples such as perfect metal or uniform dielectrics. In Fig.1.3, the peak electric field between a spherical tip and a dielectric sample can be calculated as a superposition of electric fields generated by a series of point image charges.[21] While analytical solvable scenarios are rare, such analysis offers insight about dependence of NSMM signal on sample properties and provides a method to interpret the measured signal.

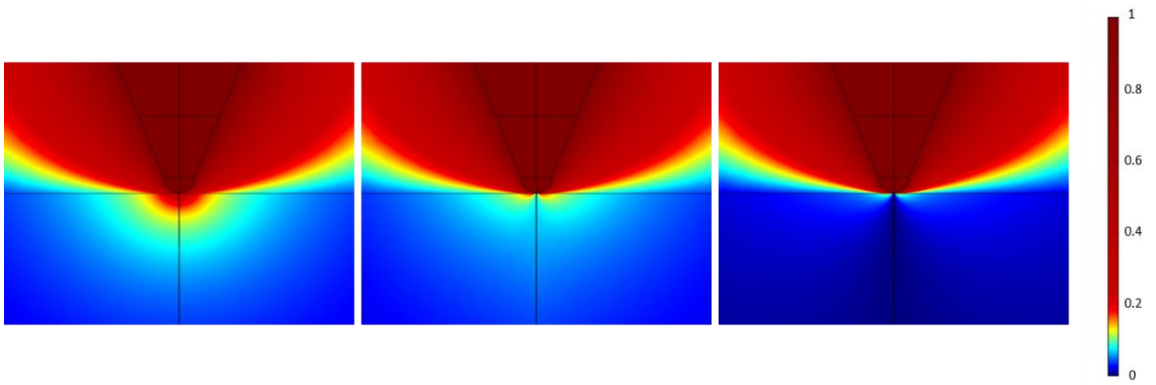

Figure 1.4: Quasi-static field distribution simulated using commercial software COMSOL Multiphysics.

For more complicated probe and sample configuration, numerical solution can be obtained using FEA. FEA solves partial differential equations (Maxwell's equations in this case) with boundary condition by calculating approximate values at subdivided small portions of the whole system. With specified probe-sample geometry and assigned electromagnetic properties, FEA can simulate the distribution of electromagnetic fields (as shown in Fig. 1.4), based on which the admittance (current divided by voltage) between probe and sample can be deduced. Furthermore, dependence of $Y_{\text{tip}-\text{sample}}$ on specific property such as conductivity or permittivity can be readily investigated by varying the value assigned in the FEA model, which will be discussed in later chapters.

1.3 Detection Electronics of Near-field Microwave Microscopy

When a microwave probe is coupled to a confined area of the sample, its change in microwave response is monitored by detection electronics, which usually consists of RF and dc circuits converting microwave signals to dc voltages. From the perspective of microwave engineering, the probe along with the impedance between probe and sample can be generalized as a network of lumped elements with one or two ports, depending on whether reflected or transmitted signal is measured.

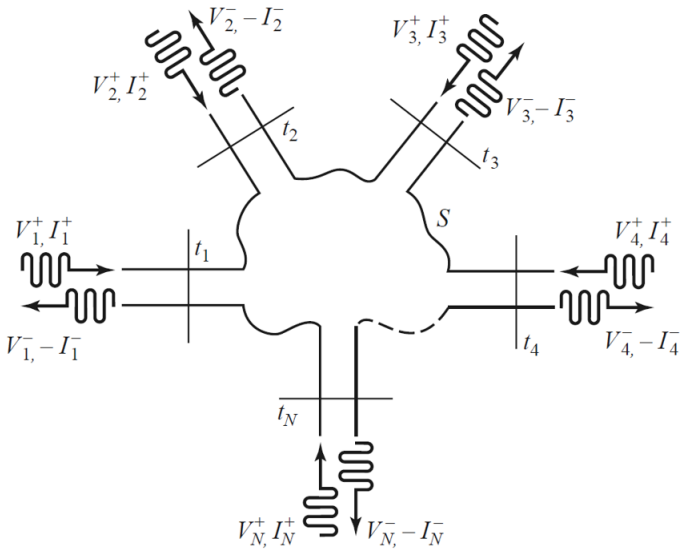

Figure 1.5: An arbitrary N-port network. Adapted from Ref. 22.

To characterize an arbitrary N-port network shown in Fig 1.5, a common representation of the scattering matrix is as follows:

$$\begin{bmatrix} V_1^- \\ \vdots \\ V_N^- \end{bmatrix} = \begin{bmatrix} S_{11} & \cdots & S_{1N} \\ \vdots & \ddots & \vdots \\ S_{N1} & \cdots & S_{NN} \end{bmatrix} \begin{bmatrix} V_1^+ \\ \vdots \\ V_N^+ \end{bmatrix},$$

where V_N^+ is the amplitude of the voltage wave incident on port N, V_N^- is the amplitude of the voltage reflected from port N, and the scattering matrix relates the output voltage waves with the input ones. For reflection measurements, the above formula is simplified to the one-port case with $V_1^- = S_{11} \cdot V_1^+$; for transmission measurements, assuming incident wave only through port 2 (i.e. $V_1^+ = 0$), $V_1^- = S_{12} \cdot V_2^+$. As transmission happens between an excitation electrode and a sensing one that are spatially separated, the data analysis is rather complicated. Therefore, while transmitted signal can be interesting in certain cases[23], the majority of research effort is focused on reflection measurement.

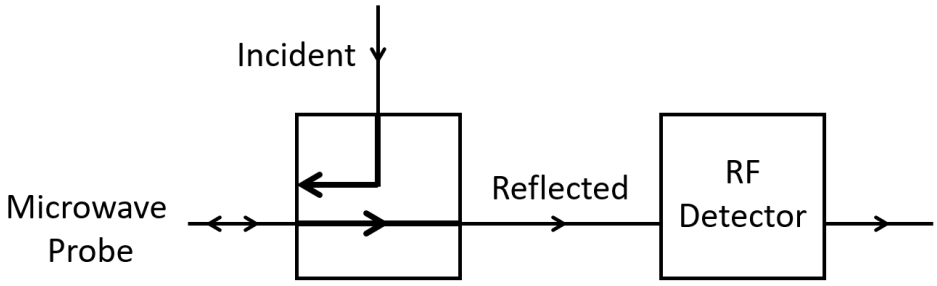

Figure 1.6: A generalized sketch for S_{11} measurement in NSMM.

To measure S_{11} that carries the information of tip-sample interaction, a microwave signal with fixed power level is generated by a microwave source and directed to the probe. A circulator or a directional coupler is usually used to separate the incident microwave with the reflected one. Early designs of NSMM use a diode to detect the power or amplitude of reflected signal.[8, 13, 24] For resonant probes, amplitude change in reflected signal is a convolution of change in both resonant frequency f_R and quality factor Q of the microwave resonator. Therefore, feedback loops are often used to track the resonant frequency and the output will be the frequency shift Δf_R and the quality factor Q, whose value can be interpreted using the theory of a perturbed resonator.[16, 18] The complex S_{11} can also be resolved with both amplitude and phase utilizing a vector network analyzer (VNA).[10, 25, 26]

A resonant probe has its own advantage for more accurate measurements of tip-sample interaction. As waveguide-based probes are typically terminated with open or short circuit, such impedance mismatch leads to a reflection coefficient S_{11} or Γ close to 1 since $\Gamma = \frac{Z_L - Z_0}{Z_L - Z_0}$ where Z_0 is the characteristic impedance of the transmission line, typically 50 Ω, and Z_L is the load impedance. $Z_L \gg 1$ for open end; $Z_L \sim 0$ for short end. The existence of tip-sample interaction will affect Z_L by a small amount, thus slightly changing the reflection coefficient. With the reflected signal dominated by a large

background, it is obvious that sensitivity of waveguide-based probes will be limited. On the other hand, resonant probes are usually operated at frequencies with effective impedance of probes matched with transmission lines ($Z_L \sim Z_0$). Therefore, the reflection coefficient from probe will be very close to 0, making it sensitive to the minute change of tip-sample interaction. A RF amplifier can further amplify the weak reflection for enhanced signal strength.

Another typical technique to further increase the signal to noise ratio (SNR) is modulation, including amplitude modulation of exciting RF signal[19], probe-sample distance modulation[4], external electric/magnetic field intensity modulation[3, 27]. While SNR is indeed enhanced through such method, the periodically varied tip-sample interaction may cause complication for data interpretation.

1.4 Applications of Near-field Microwave Microscopy

A broad spectrum of topics has been investigated using near-field microwave microscopy, facilitating material characterization and offering insights that are unavailable through other techniques. In essence, NSMM measures sample properties by monitoring the change of electromagnetic filed around the microwave probe, which can be induced by mechanisms such as fields generated by active devices[23, 26, 28] and intrinsic variation of conductivity and permittivity[4, 11, 17, 21, 29-31]. Results of such studies are usually presented as images of NSMM signals (reflection/transmission coefficient, frequency shift and Q of resonant probes) which can be correlated to specific physical properties through comparison with standard samples.

NSMM can also be applied to investigate many other phenomena that are accompanied with conductivity change, such as photoconductivity[17, 32], thermometry[33], gas

sensing[34], metal-insulator transition[35], dopant profiling of semiconductor devices[36], Hall effect[37], etc.

Besides electromagnetic field perturbation caused by conductivity and permittivity, energy absorption can be another cause of contrast in NSMM images. Specific examples include electron spin resonance (ESR) or electron paramagnetic resonance (EPR)[38] and response from biological samples like cells[19] and DNA[39].

1.5 Dissertation Outline

With the history of near-field microwave microscopy briefly reviewed, the following chapters of this dissertation will introduce the microwave microscopy I have been developing during my graduate research, namely microwave impedance microscope (MIM), and demonstrate its application in the study of novel quantum materials. For each category of materials, a short introduction will be included as the necessary background information.

Chapter 2 of this dissertation covers the fundamentals of MIM. The working mechanism will be explained from individual components to signal interpretation. Development of MIM will be discussed in Chapter 3, including efforts for quantitative measurements, expanded bandwidth for spectroscopy measurement, implementation in continuous flow and dry cryogenic systems, and other improvements.

Chapter 4 explores the application of MIM for investigation of emergent phenomena at ferroelectric domain walls. Specifically, I will demonstrate the capability of MIM in detecting ultralow-energy structural dynamics at these nanoscale entities.

Chapter 5 demonstrates the results of nanodevice imaging using MIM. I will emphasize the advantage of MIM in characterization of nanodevices with a variety of examples inaccessible by other techniques.

Chapter 6 will conclude the dissertation and give the outlook for the future.

Chapter 2: Microwave Impedance Microscopy

As one of the latest advances in near-field scanning microwave microscopy, microwave impedance microscopy (MIM) benefits from advanced nanofabrication techniques for probes, unprecedented computation power for tip-sample interaction, well-developed microwave technology and devices, and optimized electronics for both enhanced sensitivity and ease of data interpretation. Since its debut in 2008, MIM has made significant impact in condensed matter physics[40-43], material science[44-46], photovoltaics[47-49], device engineering[50, 51], and biological science[52, 53], with an ever-increasing list in the near future. Therefore, an introduction to MIM, capturing both the big picture and the technical details, is highly desired for researchers to better interpret and appreciate the diverse results acquired by MIM, both in this dissertation and in other journal articles. In this chapter, I will first walk through the working principles of MIM, then scrutinize every important section of the instrument, and finally summarize the workflow of a MIM experiment. Here I will restrict the discussion to the standard MIM setup that is most widely used and now commercially available. Development of MIM including new probe design and advanced operation modes will be described in the following chapter.

2.1 MIM in a Nutshell

MIM is a scanning probe microscope (SPM) that measures the admittance (inversion of impedance) between a sharp conductive tip and the sample underneath at radio / microwave frequency (~1 MHz to 10 GHz). The measured admittance is correlated with the local complex permittivity ε and conductivity σ of the material and is represented by the two output channels of the instrument — MIM-Im & MIM-Re. These two orthogonal outputs, after proper calibration, should be proportional to the imaginary and real parts of the tip-sample admittance respectively. Based on a platform of an atomic

force microscope (AFM), MIM-Im/Re signals are recorded point by point, line by line as the probe scan across the sample surface in contact mode and results are frequently displayed as false color images, visualizing the spatial variation of electrical properties.

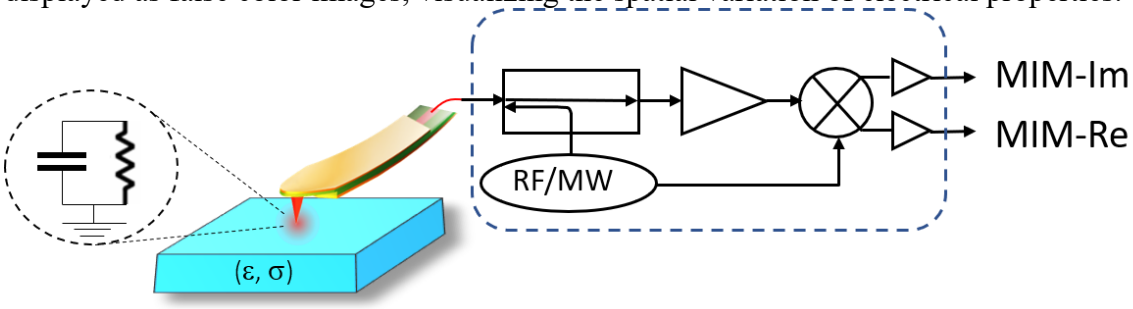

Figure 2.1: Sketched setup of MIM.

As AFM can control tip position with sub-nanometer precision in both horizontal and vertical directions, MIM can reach a maximum resolution of nanometer scale, mainly limited by the size of tip apex (from ~10 nm to more than 100 nm in diameter). Using customized MIM electronics, admittance change of sub-attofarad (aF) level can be readily detected at the GHz frequency. Since the tip-sample admittance is measured through ac coupling, MIM requires neither extra electrodes on the sample nor ohmic contacts between tip and sample. Therefore, samples need no excessive preparation and can be readily tested with a standard MIM in ambient condition. For more delicate experimental conditions, MIM experiment can be conducted in customized apparatus accordingly.

2.2 Probe Design

Microwave probe is the enabling part of microwave microscopy and successful design of a MIM probe is based on some general principles described below. The probe needs to be AFM-compatible in order to take full advantage of the scanning capability offered by modern AFM platforms. For microfabricated cantilever-based probes, a conductive stripline is necessary to carry microwave signal along the cantilever all the way

to the tip apex. The tip apex should ideally be the only part interacting with the sample and electrical shielding is thus needed to avoid stray field coupling between stripline and sample, which could induce a large background signal susceptible to low-frequency (thermal) drift. Moreover, minimized series resistance and background capacitance of the probe itself is critical to ensure high sensitivity to the minute change of tip-sample admittance when implemented in a resonant circuit. Finally, batch-processed fabrication is highly desired for consistent probe quality and large-scale application.

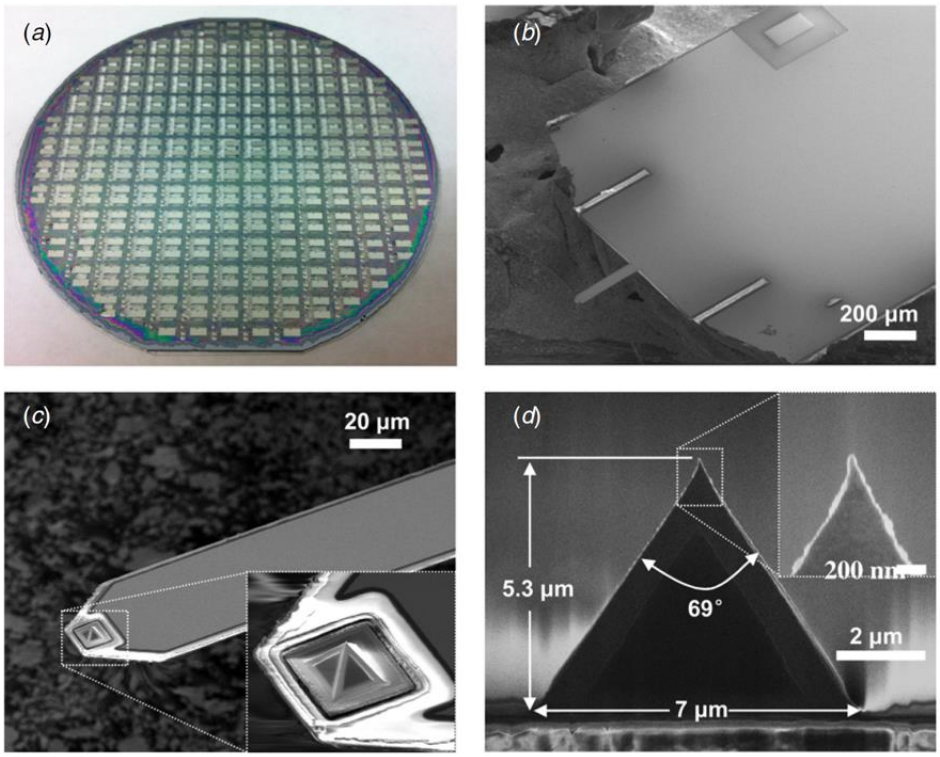

Figure 2.2: The 5th generation design of MIM probes. Adapted from Ref. 54.

In practice, MIM probe design has evolved through several generations[55, 56] and currently the most accepted design is the 5th generation of MIM probe, commonly referred as "Gen 5".[54] Gen 5 probes (shown in Fig 2.2) are AFM-compatible and cantilever-based with electrical shielding all the way to the pyramidal metal tip. Thanks to advanced MEMS

technology, a tip apex diameter less than 50nm can be routinely achieved for mass-produced probes at the Si wafer scale. In practice, the tip-sample admittance is measured as a perturbation to the admittance of probe itself, which should be small enough to ensure high sensitivity. Therefore, with great care, the width of the center conducting stripline and the thickness of the insulation dielectrics are optimized for small series resistance ($< 5\ \Omega$) and background capacitance ($\sim 1\ pF$). In addition, the structure of the cantilever is designed to be symmetric to balance the stress and thermal expansion on both sides, keeping cantilever straight in variable-temperature experiments. Details of the probe including the process of fabrication and its performance test can be found elsewhere[54]. The probe is now commercially available from PrimeNano Inc.

2.3 Tip-Sample Interaction

A thorough analysis of tip-sample interaction is crucial to understand how electrical properties of sample affect the admittance of the probe, which further leads to change of output MIM signal. In this section, I will first discuss the equivalent circuit of the MIM probe and its relationship with the tip-sample interaction. Then a qualitative estimation of tip-sample admittance on different sample will be given. Lastly, tip-sample admittance will be numerically calculated using the method of finite element analysis (FEA).

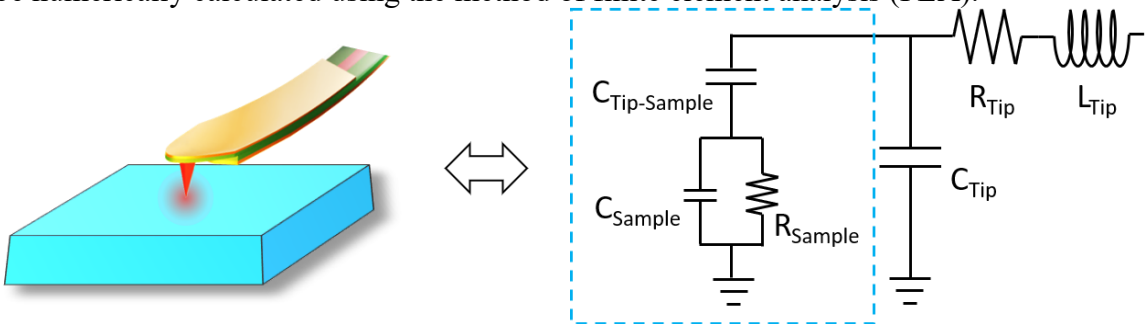

Figure 2.3: Equivalent circuit of the MIM probe and the tip-sample interaction.

Fig. 2.3 displays the equivalent circuit of the MIM probe with the general form of tip-sample interaction marked in the dashed rectangle. The probe itself can be regarded as an inductor, a resistor, and a capacitor in series. The inductance is due to the length of the metal stripline and the jumping wire connecting the probe to a microwave coaxial cable. The resistance comes from the stripline with a finite width and thickness. The potential distribution within the probe can be regarded as uniform because the series resistance is small and the dimension of the probe (~ 2 mm) is much smaller than the wavelength of microwave signal. Therefore, the total capacitance can be approximated by a capacitor in series with the resistor and the inductor, although the capacitance between the center stripline and the grounded shield indeed exists everywhere along the conducting path. The tip-sample interaction can be represented as the capacitance between the tip apex and the sample, in series with the impedance of sample, which generally consists of resistive and capacitive components. Note that the existence of tip-sample capacitance is very common due to separation induced by surface contamination, "dead" layer of material, or non-ohmic contact. Only in rare cases such as a metal surface free of oxide, the tip-sample capacitance can be absent. Finally, the tip-sample interaction should be in parallel with the tip-shield capacitance. As the tip-sample interaction is limited to the tip apex region, the induced tip-sample admittance will be rather small compared with the original tip admittance. Therefore, we will treat the tip-sample admittance as a perturbation to the admittance of a tip in air without any surrounding samples.

With the effective circuit of the probe and the tip-sample interaction determined, we can qualitatively estimate the tip-sample admittance in different types of materials. For insulating sample such as dielectrics, the sample impedance will be purely capacitive. Thus, the tip-sample admittance will be the admittance of two capacitors $C_{\mathrm{Tip-Sample}}$ and C_{Sample} in series. Higher dielectric constant will lead to higher C_{Sample} and consequently

higher tip-sample admittance. For highly conducting samples such as metals, the sample impedance will be nearly zero and the tip-sample admittance will again be capacitive with its value determined by $C_{\mathrm{Tip-Sample}}$. For samples with intermediate conductivity, the sample admittance consists of parallel resistance R_{Sample} and capacitance C_{Sample}. As the conductivity of sample increases from the insulating limit to the conductive limit, the resistance of sample will decrease while the tip-sample capacitance increases. Neglecting the relatively small sample capacitance, the total admittance will be

$$Y_{\mathrm{t-s}} = \frac{1}{\frac{1}{i\omega C_{\mathrm{Tip-Sample}}(\sigma)} + R_{\mathrm{Sample}}(\sigma)},$$

where ω is the circular frequency of microwave and $C_{\mathrm{Tip-Sample}}$, R_{Sample} are functions of the sample conductivity σ. The real part of the above expression can be deduced as

$$Real(Y_{\mathrm{t-s}}) = \frac{1}{R_{\mathrm{Sample}}(\sigma) + \frac{1}{\omega^2 C^2_{\mathrm{Tip-Sample}}(\sigma) R_{\mathrm{Sample}}(\sigma)}},$$

whose maximum exists when the following condition is satisfied

$$\omega = \frac{1}{R_{\mathrm{Sample}}(\sigma) C_{\mathrm{Tip-Sample}}(\sigma)}.$$

Therefore, with some approximation, we can already predict that, with the conductivity of sample increasing from the insulating limit to the conductive limit, the imaginary part of tip-sample admittance (capacitive term) will monotonically increase while the real part (loss term) will peak at certain conductivity and drop to zero at both limits. Moreover, using different microwave frequencies for detection, the maximum in $Real(Y_{\mathrm{t-s}})$ will shift to different σ accordingly. Since the dependence of tip-sample admittance on other properties such as permittivity, polarization, dielectric relaxation, etc., can be discussed in the same way as above, the details will not be discussed here case by case. Instead, I will introduce a general method to calculate the tip-sample admittance in arbitrary configurations of tip geometry and sample dielectric properties.

In principle, the tip-sample admittance can be calculated by solving Maxwell's equations with certain boundary conditions. However, analytical solutions can be obtained only when the system is highly symmetric, either spherical or cylindrical, and when the tip geometry is simple, e.g. spherical tip. On the other hand, a numerical solution for arbitrary tip and sample geometry can be achieved through finite element analysis. Dividing the system into small sections, the original partial differential equations can be approximated by a set of algebraic equations connecting the potential values of neighboring sections. Owing to the ever-increasing computational power of modern computers, the time and space complexity of finding a converging solution for such huge set of equations is no longer as dreadful as it was decades ago. Moreover, commercial FEA software has further simplified the process. Next, I will demonstrate how to calculate the admittance between tip and sample with varied sample conductivity using COMOSL. The FEA model can be built following the steps given by Model Wizard.

1) Choose the space dimension: Here we select axisymmetric for a tip on a uniform sample, which will simplify the model and accelerate the calculation.
2) Select physics to be studied: "Electric Currents" from "AC/DC" module is chosen here to compute electric field, current and potential distribution.
3) Select studies: "Study" here means a specific kind of problem to solve. We choose "Frequency Domain" to compute the response of the model subjected to harmonic excitation of one specific frequency, i.e. microwave frequency voltage on tip. Step 2&3 effectively determines the equations to solve in each unit.
4) Build the model in "Geometry" menu according to actual tip and sample dimensions: The tip apex can be modeled as a cone with a spherical head.

Several parameters define the tip: R_1 the curvature of the spherical head; R_2 the radius of the apex; h the height of the tip apex; θ the angle between the generatrix and the axis. In practice, typical values for R_1, R_2, and θ can be measured from SEM images of the probe; h is usually chosen ~ 1 μm to be consistent with the length of the oxide-sharpened part of apex. The difference is negligible whether or not the pyramidal part of the probe is included in the model. We further define the simulated region as a box of air surrounding the tip and a box of sample underneath. The box size L is chosen to be 10 μm here as a balance between emulating the real situation (infinitely large) and keeping the model size small. The tip is separated from the sample by a distance d ~ 3 nm.

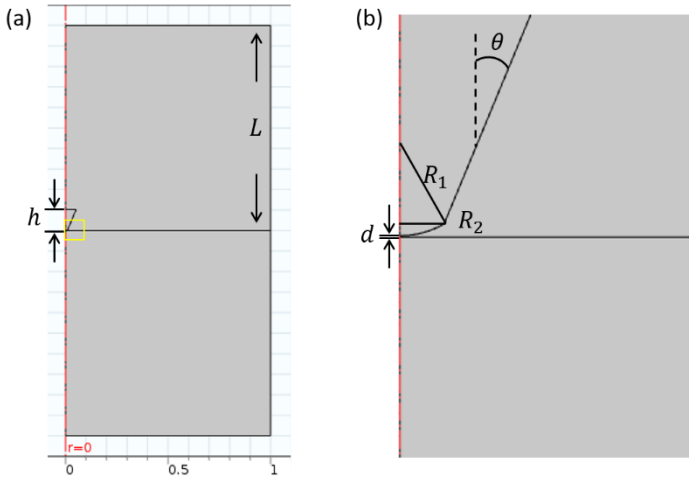

Figure 2.4: The model geometry for FEA: (a) overview of the whole model. (b) zoom-in view of the tip-sample region.

5) Assign material properties in "Materials" menu: The tip is assigned a conductivity σ of $10^8\ S/m$ as a perfect metal; for simplicity, the air is assigned a relative permittivity ε_r of 1 with zero conductance; the sample is assigned ε_r of 10 with σ to be determined.

6) Define boundary conditions in “Electric Currents” menu: The boundary of tip is defined as a “terminal” with a fixed voltage of ~ 0.1 V. The circumference of the system is defined as another terminal with a fixed voltage of zero or ground.

7) Generate mesh for the model in “Mesh” menu: Mesh determines how the volume of the entire system is divided into small parts with equal potential. Consequently, results calculated by FEA get closer to real values with finer mesh. On the other hand, mesh should be denser near small entities and sparser for large uniform ones. Fortunately, COMSOL automatically generates physics-controlled mesh with different density (from “extremely coarse” to “extremely fine”) as shown in Fig 2.5.

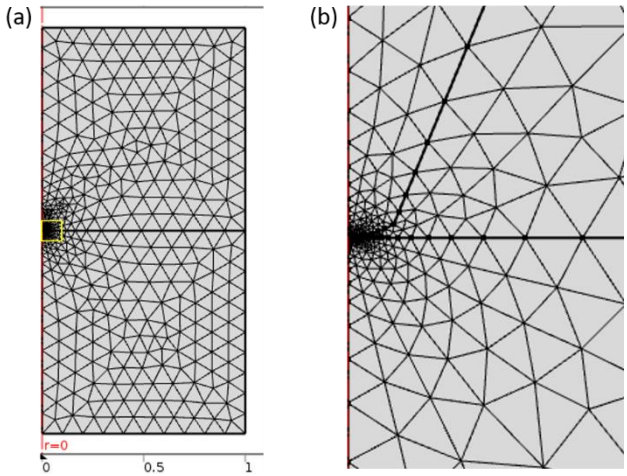

Figure 2.5: The generated “fine” mesh for the demonstration model: (a) overview. (b) zoom-in view of the tip-sample region.

8) Determine frequency and calculate quasi-static potential distribution in “Study\Frequency Domain”: For this demonstration, the frequency is set to 10^9 Hz, i.e., 1 GHz. Then the quasi-static potential distribution can be calculated by pressing the “Compute” button. One can examine if FEA

generates a reasonable solution by inspecting the potential distribution in "Results\Electric Potential".

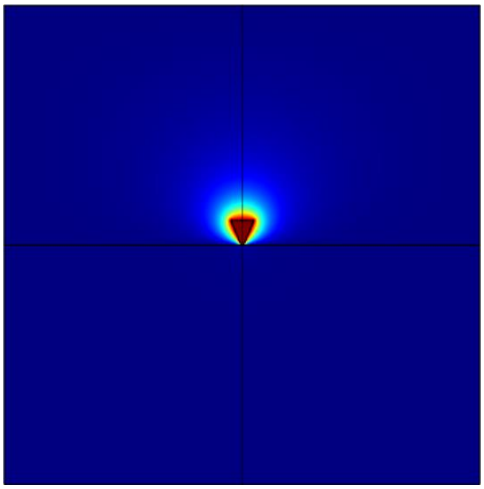

Figure 2.6: The calculated potential distribution with the tip on top of a metallic sample.

9) Calculate tip-sample admittance by varying parameters using "Study\Parametric sweep": With quasi-static potential calculated, the admittance between the tip and the sample can be calculated in "Results\Derived Values\Global Evaluation". "Parametric sweep" repeats the simulation while changing one or several parameters over the specified parameter space.

In this demonstration, the sample conductivity is ramped from 10^{-4} S/m to 10^{4} S/m and the tip-sample admittance is calculated accordingly (shown in Fig. 2.7). With increasing sample conductivity, the screening of electric field becomes more evident. A peak in energy loss occurs at intermediate sample conductivity. The result is consistent with the qualitative picture mentioned above. Dependence on other parameters, such as tip geometry and tip-sample distance, can be investigated with FEA in a similar way. In later sections and chapters, the dependence of tip-sample admittance on various sample

parameters will be frequently studied to interpret the MIM results. Plenty of resources can be found on the website of COMSOL with details of FEA for all kinds of scenarios.

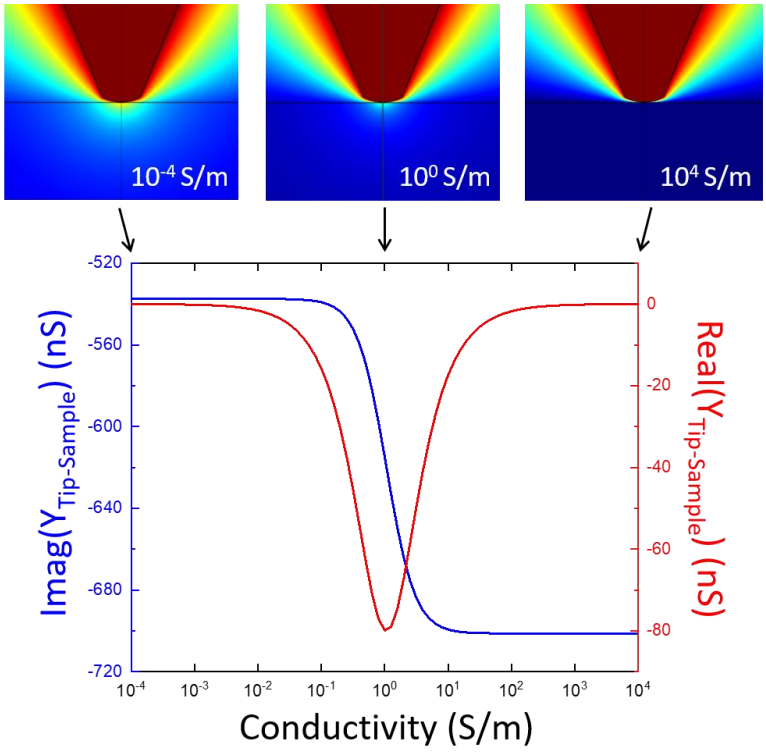

Figure 2.7: Dependence of tip-sample admittance on the sample conductivity. The three images above show the potential distribution with σ of 10^{-4}, 10^{0}, 10^{4} S/m respectively.

2.4 Impedance Match

For a uniform transmission line, the characteristic impedance Z_0, typically 50 Ω, is defined as the ratio between voltage and current for a propagating sine wave. On the other hand, not every microwave component shows an impedance with a purely real part of 50 Ω. Therefore, if such load impedance Z_L is connected to a transmission line, the reflection coefficient or return loss will be

$$\Gamma = \frac{Z_L - Z_0}{Z_L - Z_0},$$

and a large portion of power will be reflected. In order to improve power transmission, an impedance matching network is needed in between a load impedance and a transmission line so that the impedance seen looking into the matching network equals Z_0. Moreover, a lossless matching network will maximize the power delivered to Z_L.

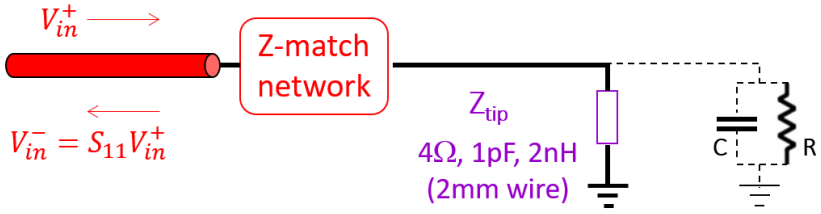

Figure 2.8: Sketch of impedance match for a MIM probe.

Fig. 2.8 illustrates the impedance matching for a Gen5 MIM probe connected to the circuit using an exposed 2-mm-long metal wire. Essentially the tip impedance and the impedance matching network form a resonant circuit whose resonant frequency equals that of the input signal. As a result, the reflection coefficient S_{11} will be minimized and the sensitivity of the resonator ΔS_{11} is maximized for perturbation caused by tip-sample interaction.

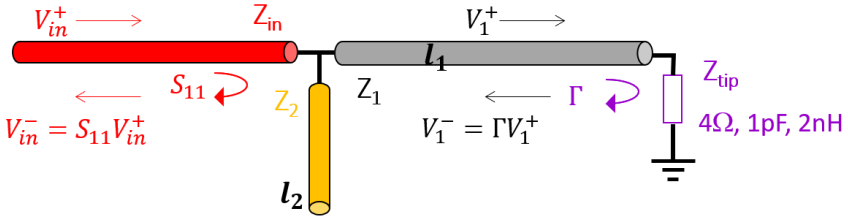

Figure 2.9: Stub tuning for a MIM probe.

In practice, impedance matching network can be made up of lumped elements, transmission lines, or a combination of both. A feasible method to match the tip impedance is referred to as stub tuning, which uses a single open-circuited section of transmission line (stub) connected in parallel with the feed line at a certain distance from the load, as shown

in Fig. 2.9. While the cable connected to the probe is fixed in length, the length of the parallel stub can be modified rather easily, just by cutting, to search for an optimized S_{11}. The impedance at a distance l from the load Z_L can be expressed as:

$$Z_{\text{distance}} = Z_0(1 + \Gamma e^{-2\gamma l})/(1 - \Gamma e^{-2\gamma l}).$$

Here Γ is the return loss $(Z_L - Z_0)/(Z_L + Z_0)$ and γ is the complex propagation constant of the transmission line, usually determined from specifications. Therefore, for Z_1 in Fig. 2.9:

$$Z_1 = Z_0(1 + \Gamma e^{-2\gamma_1 l_1})/(1 - \Gamma e^{-2\gamma_1 l_1}).$$

where $\Gamma = (Z_{\text{Tip}} - Z_0)/(Z_{\text{Tip}} + Z_0)$ and $Z_{\text{Tip}} = R + i\omega L + 1/i\omega C$.

For Z_2, with $Z_L \to \infty$, $\Gamma = 1$, thus

$$Z_2 = Z_0(1 + e^{-2\gamma_2 l_2})/(1 - e^{-2\gamma_2 l_2}).$$

The impedance seen by looking into the matching network can be calculated by considering the parallel connection of Z_1 and Z_2:

$$Z_{in} = (Z_1^{-1} + Z_2^{-1})^{-1}.$$

And the final reflection coefficient is,

$$S_{11} = (Z_{in} - Z_0)/(Z_{in} + Z_0).$$

Therefore, for a given microwave frequency, the only two variables in the above matching network are l_1 and l_2. Through the transmission-line simulation described above, one can search through the two-dimensional parameter space and find the solution for minimized S_{11}. For ΔS_{11}, one can simply repeat the calculation above with $Z_{tip}'^{-1} = Z_{tip}^{-1} + i\omega\Delta C + 1/\Delta R$ and calculate the difference between the two results. Fig. 2.10 shows the results of transmission line simulation using parameters of Astrolab 32018 cable with length l_1 and UT-085C-TP cable with length l_2. For a fixed microwave frequency, the minimum of S_{11}, which coincides with the maximum of ΔS_{11}, can be found when l_1

is close to a quarter of the wavelength in the transmission line. Therefore, the cable is commonly referred as a quarter-wave cable (QWC).

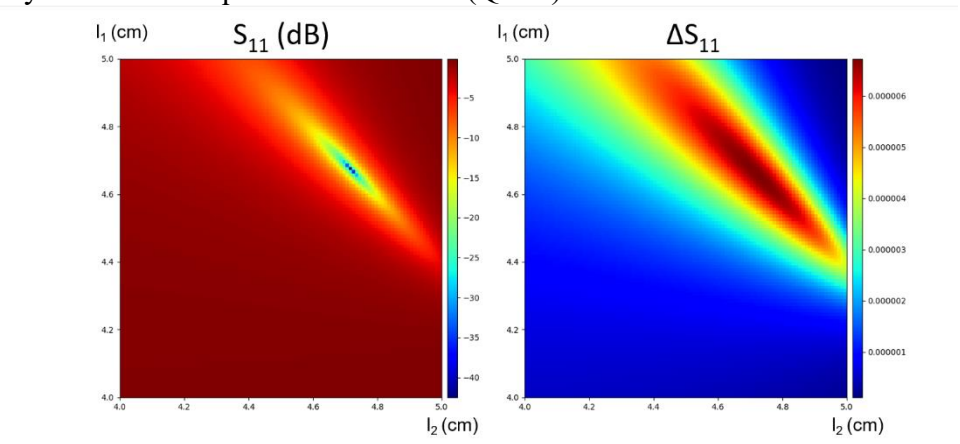

Figure 2.10: Search for the minimum of S_{11} with varied l_1 and l_2.

In practice, after the length of QWC is determined, one can tune the length of the open stub while monitoring S_{11} on a vector network analyzer (VNA). For each value of the open stub length, the VNA will display S_{11} as a function of frequency f. By trimming a relatively long stub, as shown in Fig 2.11, the dip in S_{11} vs. f diagram will first become deep and then shallow again after the sweet point. Therefore, stub tuning offers a feasible way to find the optimized solution (shown in Fig. 2.12) experimentally. It is worth noticing that while S_{11} varies greatly between matched and unmatched cases, ΔS_{11} as a measure of sensitivity does not differ too much between different l_2.

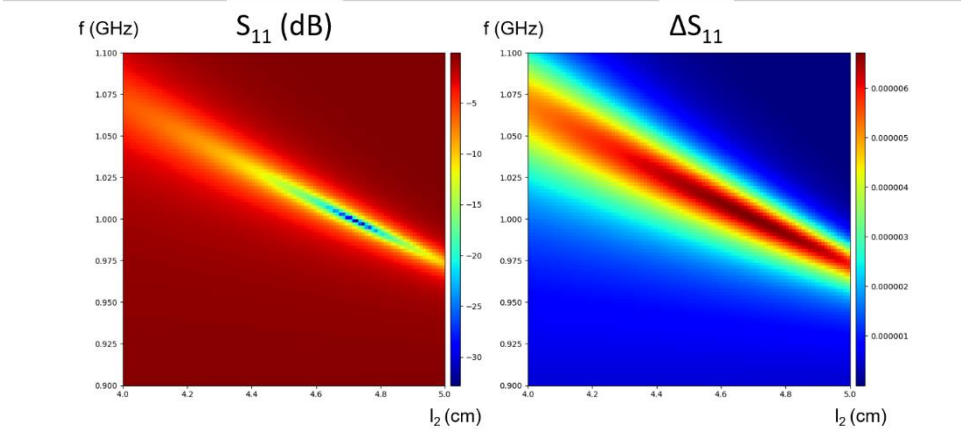

Figure 2.11: S_{11} and ΔS_{11} as a function of frequency f and stub length l_2.

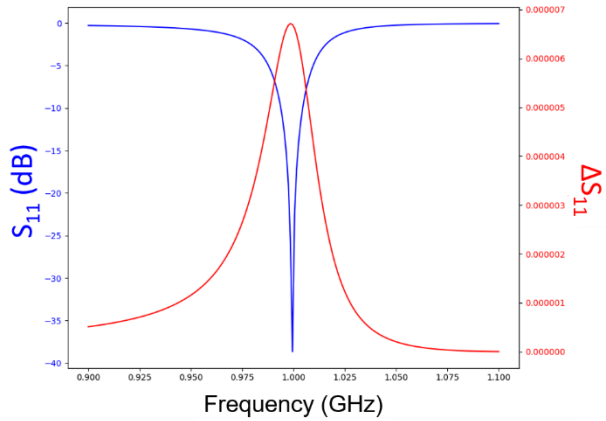

Figure 2.12: S_{11} optimized with stub tuning method.

Matched impedance also ensures that the voltage on the tip can be enhanced by a factor of ~ 3, compared with the unmatched case. The detailed derivation involves calculation of voltage at different intersection and will not be included here.

2.5 MIM Electronics

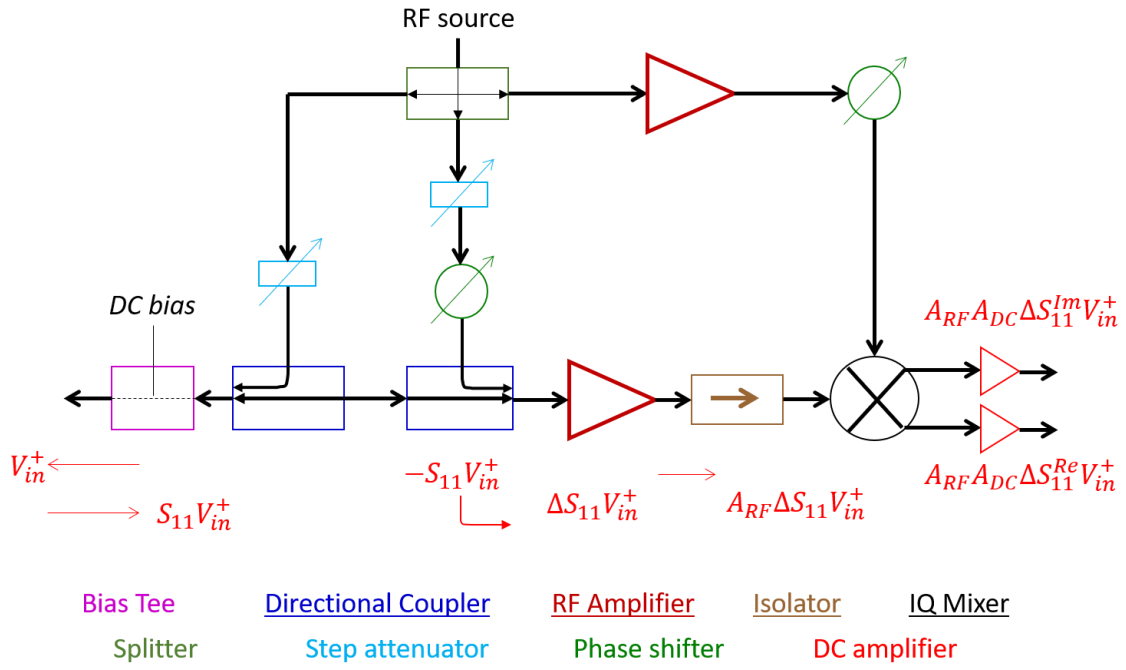

Figure 2.13: Block diagram of MIM detection circuitry.

In principle, the MIM electronics (as shown in Fig. 2.13) measures the reflection from the matching network mentioned in the last section. The reflected signal contains a large background, which could saturate the amplifiers and randomly drift over a long term. In order to sensitively pick up the small change from this large background or common-mode signal, a cancelation signal that is equal in amplitude but opposite in phase is combined with the reflected signal. The contrast signal is then amplified by RF amplifiers, demodulated by an IQ mixer, and amplified again in the DC stage. The total gain of the system, including RF and DC, can be calibrated by feeding a RF signal of small power and measuring the output voltages. The instrument here is calibrated to have a gain of 106 dB (2×10^5) at 1 kHz bandwidth. Therefore, assuming -20 dBm (10 μW) input power, a 1 aF capacitance change at the tip produces ~ 30mV in the output:

$$\Delta V_{out} = V_{in}^{+} \cdot \Delta S_{11} \cdot G = 22\, mV_{rms} \cdot 7 \times 10^{-6} \cdot 2 \times 10^{5} = 30.8\, mV,$$

where ΔS_{11} per capacitance change of 1 aF is from transmission line simulation in the last section. Considering Johnson noise

$$V_J = \sqrt{4k_B TBR} = \sqrt{4k_B(300\text{K})(1\text{kHz})(50\Omega)} \approx 30\text{nV}$$

and shot noise

$$V_S = \sqrt{2eVBR} = \sqrt{2e(0.02\text{V})(1\text{kHz})(50\Omega)} \approx 20\text{nV},$$

the total output noise of the setup is

$$V_n = G\left(V_J + V_S\right) = 10\text{mV}.$$

Therefore, when properly tuned, the microscope is sensitive to local impedance change less than 1 aF.

The signal of MIM possesses two important properties: **linearity** — MIM signal is always proportional to change of tip-sample admittance, and **orthogonality** — the imaginary and real parts of tip-sample admittance only cause change in signals from the corresponding output channels (MIM-Im / MIM-Re). The linearity and orthogonality of the MIM signal can be understood the following way. First, the MIM signal $\mathcal{M}$ after cancelation can be expressed as:

$$\mathcal{M} = e^{i\phi} G \cdot [V_{in}^{+} \cdot S_{11}\left(Y_{Tip}\right) + V_{Cancel}] + \text{offset}.$$

Here the cancelation signal should be close to $-V_{in}^{+} \cdot S_{11}\left(Y_{Tip}\right)$ and the offset is induced in the dc amplification stage. The factor $e^{i\phi}$ is induced by the IQ mixer reference. In general, $\mathcal{M}$ depends on a function F of Y_{Tip}:

$$\mathcal{M} = e^{i\phi} F\left(Y_{Tip}\right) + \text{offset},$$

If we regard the tip-sample admittance $Y_{Tip-Sample}$ as a perturbation to Y_{Tip}, then the generalized function F can be Taylor expanded around Y_{Tip} to the first order so that:

$$\mathcal{M} = e^{i\phi}[F\left(Y_{\text{Tip}}\right) + F'\left(Y_{\text{Tip}}\right)Y_{\text{Tip-Sample}} + O\left(Y_{\text{Tip-Sample}}^{2}\right)] + \text{offset},$$

Combining all constant terms,

$$\mathcal{M} = e^{i\phi} F'\left(Y_{\text{Tip}}\right) Y_{\text{Tip-Sample}} + \text{constant},$$

By properly adjusting the phase ϕ of the mixer reference to cancel the phase of $F'\left(Y_{\text{Tip}}\right)$, we can obtain:

$$\mathcal{M} = a \cdot Y_{\text{Tip-Sample}} + \text{constant}, \ a \in \mathbb{R}$$

or

$$\text{Imag}(\Delta\mathcal{M}) = a \cdot \text{Imag}(Y_{\text{Tip-Sample}})$$

$$\text{Real}(\Delta\mathcal{M}) = a \cdot \text{Real}(Y_{\text{Tip-Sample}}),$$

which can be output respectively through the two channels that are 90° out of phase.

Since $F = G \cdot V_{in}^{+} \cdot S_{11}\left(Y_{Tip}\right)$, the claim that the tip-sample admittance $Y_{\text{Tip-Sample}}$ is a perturbation to Y_{Tip} can be checked numerically by calculating $\Delta S_{11}/Y_{\text{Tip-Sample}}$ within different range of $Y_{\text{Tip-Sample}}$. As shown in Fig. 2.14, $\Delta S_{11}/Y_{\text{Tip-Sample}}$ can be regarded as a complex constant within range of 1000 nS, which covers the typical range of tip-sample admittance.

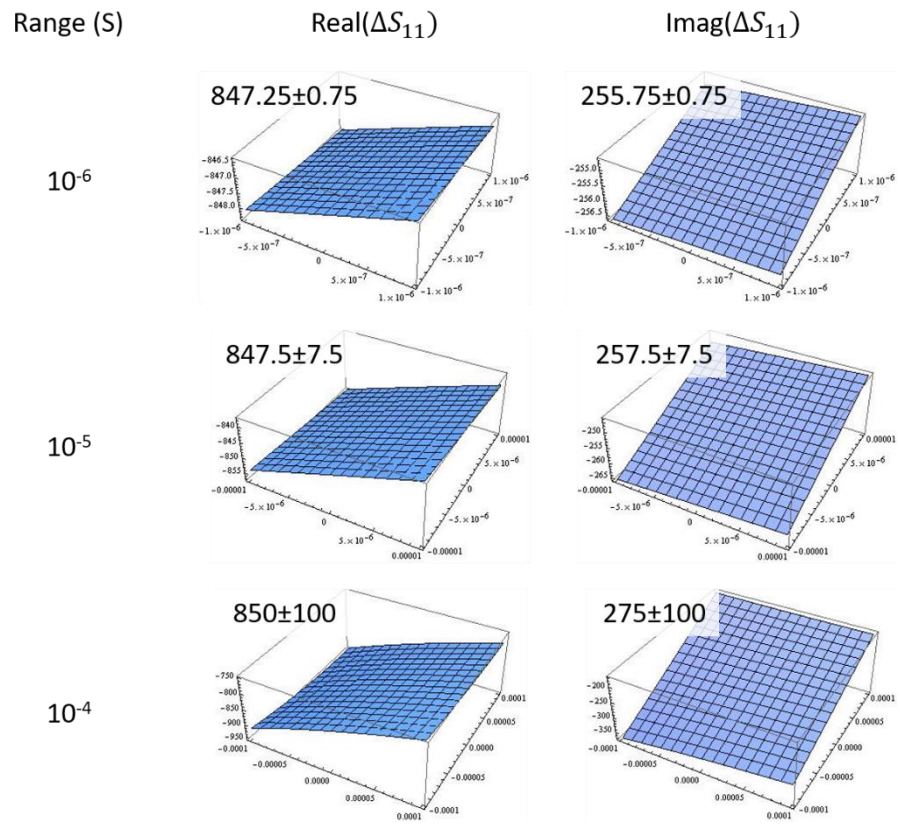

Figure 2.14: $\Delta S_{11}/Y_{\text{Tip-Sample}}$ numerically calculated within assigned range of $Y_{\text{Tip-Sample}}$. The x & y axes indicate the range of $Y_{\text{Tip-Sample}}$ while the z axis indicates the ratio of $\Delta S_{11}/Y_{\text{Tip-Sample}}$.

Lastly, we want to comment that, unlike many existing NSMMs that utilize the frequency shift and change of the quality factor Q for measurements, the electronics here measures the imaginary and real parts of the tip-sample admittance, which can be directly interpreted by FEA. With tip-sample admittance regarded as a perturbation to the tip admittance, the linearity and orthogonality of MIM signals further facilitate quantitative data analysis.

2.6 Summary and MIM Examples

Using probes fabricated by advanced MEMS techniques, the tip-sample interaction can be confined to a nanometer scale region. The tip-sample admittance $Y_{\text{Tip-Sample}}$ carries properties of sample and causes small changes to the tip-ground impedance. Since $Y_{\text{Tip-Sample}}$ is a perturbation to the tip admittance, the change of reflected signal from the impedance matching network is linear with respect to $Y_{\text{Tip-Sample}}$ and can be demodulated by microwave electronics into two orthogonal outputs (MIM-Im/Re) proportional to the imaginary and real parts of $Y_{\text{Tip-Sample}}$. After proper calibration, the complex $Y_{\text{Tip-Sample}}$ can be inferred from MIM-Im/Re and compared with FEA results to estimate sample properties.

With all the technical details described above, I will conclude the chapter with MIM measurements using two standard samples as a demonstration. The two standard samples are Al dots on n++Si substrate and n++ implanted p-Si.

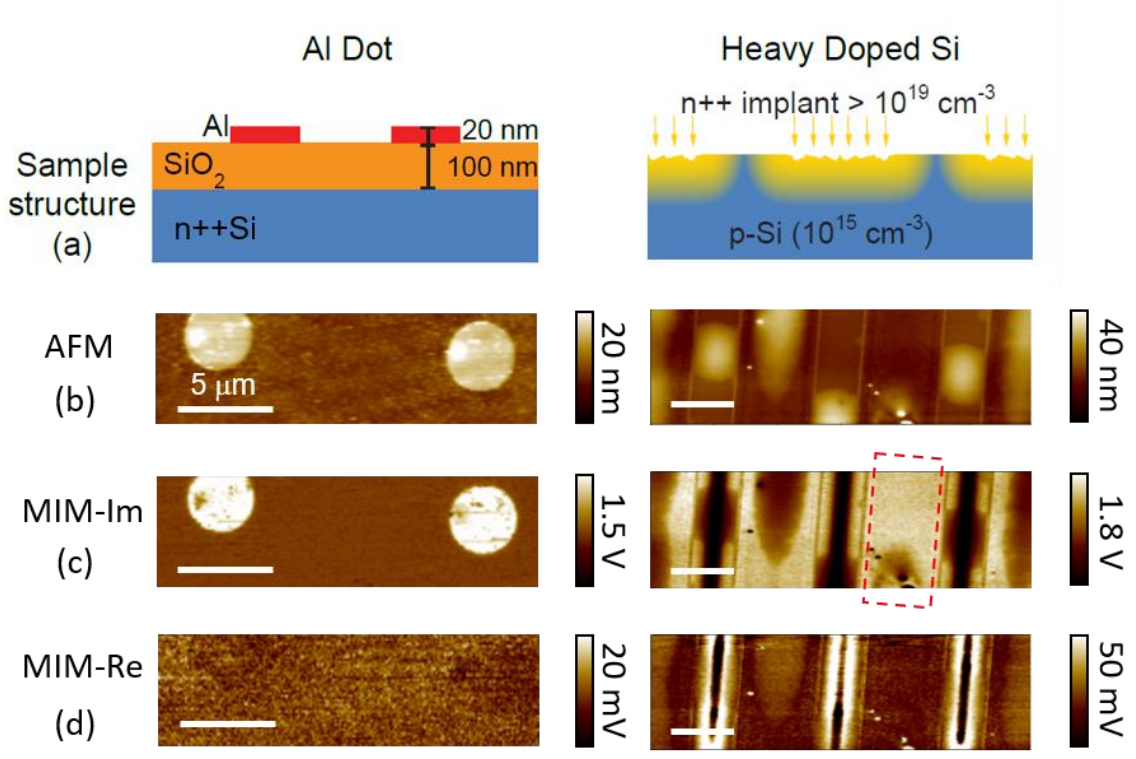

Figure 2.15: Standard samples: (a) sample structure, (b) AFM, (c) MIM-Im, (d) MIM-Re.

The standard sample with Al dots on n++Si serves the purpose of channel alignment, an important step before the actual measurement. On this sample the tip-sample capacitance is different between the ~ 4 nm native Al_2O_3 (on top of the metallic Al) and the ~ 100 nm SiO_2 (on top of the metallic n++Si) while both regions show zero real admittance, i.e., lossless. As a result, the contrast should only appear in the MIM-Im channel. This condition can be met by adjusting the phase shifter in front of the IQ mixer to nullify the contrast in the MIM-Re channel. As shown in Fig. 2.15, we can obtain good channel alignment with a residual MIM-Re/Im ratio < 1%. Moreover, colormap can be properly chosen so that bright area indicates stronger MIM-Im signal.

After channel alignment, we can perform MIM measurement on ion-implanted Si. The sample is prepared by large dosage of n++ implantation along parallel stripes on lightly

doped p-type Si and subsequent dopant diffusion through thermal annealing. Due to the heavy implantation over the original doping level, the carrier density profile at the surface is dominated by the implanted ions. As expected, the MIM-Im image shows uniformly bright stripes (e.g. marked in the red dashed box), indicating the highly conductive region. Beyond the edge of the implanted region, decreasing signal level perpendicular to stripes indicates the decreasing dopant density along the direction of diffusion. Note that MIM-Im channel is inversely coupled to topography, i.e. higher topography leads to lower MIM-Im signal. MIM-Re shows minimum signals in both implanted and undoped parts of the sample, whereas strong signals are observed in between the two, indicating pronounced energy loss at intermediate conductivity. Quantitative analysis of the dopant profile based on MIM-Im/Re signals requires FEA simulation for realistic sample structures. I will skip the detailed discussion here because similar analysis will be performed for almost every material investigated in this dissertation.

The above process demonstrates how MIM measurement is performed and how MIM images are interpreted. The same paradigm can be found in every published MIM work and will be followed in the following chapters.

Chapter 3: Development of Microwave Impedance Microscopy

In the previous chapter, I introduce the working principle of microwave impedance microscope based on commercial AFM platforms and operated in contact mode. The standard setup of MIM has been applied to study a plethora of materials with interesting physics in ambient condition. Development of MIM technique will enhance its imaging capability, enable more quantitative analysis, open up possibilities to probe new physics, and allow investigation of exotic phenomena at extreme conditions. Therefore, during my research, a considerable amount of effort has been devoted to exploration of new probe design, advanced operation modes, and implementation of MIM in extreme conditions. In Section 3.1, I will introduce a new microwave probe based on quartz tuning forks (TF) and demonstrate feasible quantitative measurements of nanoscale permittivity and conductivity using TF-based MIM.[1] In Section 3.2, I will expand the bandwidth of MIM from a single frequency to a range from 1 MHz to 10 GHz, spanning four orders of magnitude, and demonstrate the detection sensitivity at different frequencies. In Section 3.3, the implementation of MIM in a continuous flow cryostat and in a dry cryostat with strong magnetic field will be introduced. Remarks on future directions will be given in Section 3.4.

3.1 Tuning Fork-Based MIM

Early NSMMs lack feedback regulation on the tip-sample spacing and, therefore, a large force up to 10^{-5} N is usually applied to maintain the tip-sample contact.[9, 57] Such a

[1] This part of the chapter has been published as X. Wu, Z. Hao, D. Wu, L. Zheng, Z. Jiang, V. Ganesan, Y. Wang and K. Lai, Review of Scientific Instruments **89** (4), 043704 (2018). K.L. conceived and designed the experiments. D.W. fabricated the MoS_2 devices. X.W., Z.H., Z.J., and V.G. fabricated the TF-based probes, constructed the DAM-AFM and performed the TF-MIM experiment and numerical analysis. X.W. and K.L. wrote the initial draft of the paper. All authors were involved in the discussion of results and edited the manuscript.

strong contract force easily damages both the tip apex and the sample surface. In MIM the force is alleviated down to $10^{-9} \sim 10^{-7}$ N using cantilever-based probes.[19, 55, 56, 58, 59] However, tip wearing inherent in contact mode AFM still exists. More importantly, a number of problems are associated with contact-mode microwave imaging. First, due to the large background signal when measuring the reflected signal from the tip, common-mode cancelation is needed for signal amplification.[55] The information obtained this way represents only the relative admittance change rather than the absolute local properties.[56] Second, the MIM signal may drift in a long time scale as the microwave circuit and probe are susceptible to temperature and other environmental variations. Lastly, since the signal level is strongly affected by the condition of tip apex, quantification of the contact mode MIM is very difficult and extensive calibration process is needed throughout the measurements. Therefore, it is desired to develop a probe with minimal tip wearing, absolute measurement of sample properties, and drift-free signal level.

3.1.1 Design of Tuning-fork-based Probes

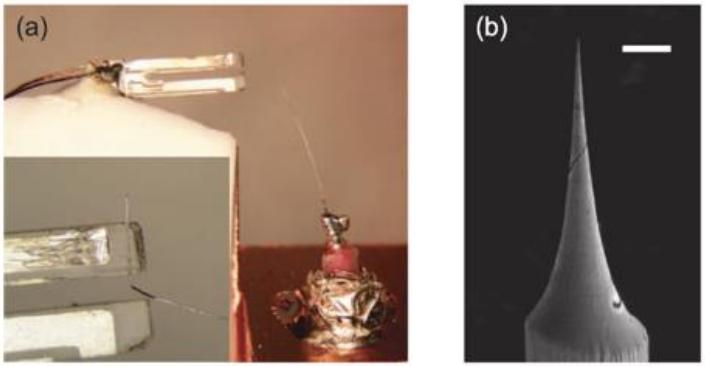

Figure 3.1: TF-based MIM probe: (a) optical images of the probe with a zoom-in view to where the metal wire is glued. (b) SEM image of the etched tip apex. Adapted from Ref. 60.

The issue of tip degradation can be partially solved by using tapping-mode MIM[61], although the spatial resolution is usually compromised by the large dithering amplitude (50 – 100 nm) in cantilever-based systems. Quartz TFs with small vibration amplitudes (< 10 nm) are widely used as the feedback elements in scanning probe microscopy[62, 63], especially under cryogenic environments. Inspired by TF-based AFM, TF-based MIM[60, 64, 65] with etched metal tips is recently proposed, which provides an elegant solution to tip degradation. As shown in Fig. 3.1(a), a TF-based probe is prepared by gluing a metal wire with a diameter of 25 μm to one prong of a quartz tuning fork. The metal wire has a sharp end electrochemically etched by commonly used recipes in the STM community. The sharpness of the tip can be accurately controlled by the etching condition to achieve an aspect ratio of ~ 5. The other end of the wire is soldered to the exposed center conductor of a coaxial cable connected to the MIM circuit via the impedance matching network.

In contrast to well-shielded cantilever probes fabricated with MEMS, a TF-based sensor simply uses a bare metal wire. But the two probes show comparable performance in noise level. For cantilever probes, shielding prevents the stray coupling between the conducting path and the sample, which is usually less than 10 μm away. For etched metal wires, the stray coupling is greatly suppressed due to the geometry of the sensor (metal tip 100 ~ 200 μm in length and perpendicular to sample surface) and the high aspect ratio of the etched tip. Detailed comparison of noise levels in the two probes can be found elsewhere.[60]

In addition to the self-sensing capability that preserves the tip condition, TF-MIM with small-amplitude distance modulation also features other advantages. For instance, the MIM electronics in contact mode are only sensitive to the relative electrical contrast between the material of interest and a background region.[66] In the TF-MIM mode, the

distance modulation automatically provides such a contrast mechanism and the demodulated MIM AC signals carry absolute information of the sample at every point.[60]

Moreover, because only the impedance between the tip apex and the closest point on the sample surface is strongly modulated, the differential measurement rejects most of the stray coupling, which is prone to drift, and thus the signal level can be stable over the entire scanning period.

3.1.2 Experimental Setup and Analytical Methods

Conventional frequency-modulation (FM) tuning-fork AFMs using stiff cantilevers and small amplitudes prove to be a powerful tool to achieve atomic resolution in ultrahigh vacuum environments[63]. However, many samples in MIM studies may have a surface roughness of 10 to 100 nm. As the change of tip-sample distance becomes comparable to the vibration amplitude, the atomic force can jump frequently between attractive and repulsive regimes, leading to non-monotonic frequency shift throughout the experiment and instability in the feedback control. On the other hand, the power dissipation of the TF sensor depends monotonically on the tip height and can therefore be used for robust feedback control for topographic sensing on rough surfaces[67]. Fig. 3.2 illustrates our implementation of TF-MIM with driving amplitude modulation (DAM) feedback control[68].

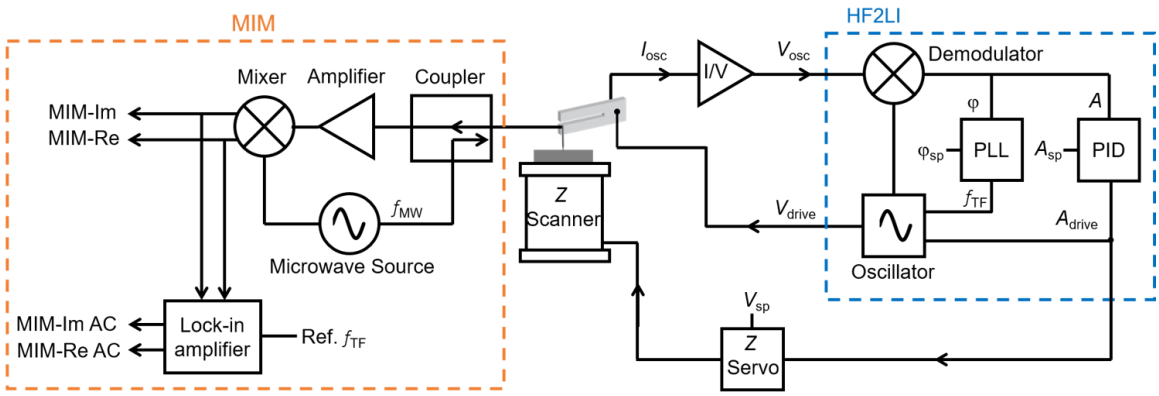

Figure 3.2: Schematic of the TF-based AFM configured for the DAM mode and the microwave electronics (detailed in the text).

In our implementation, a sinusoidal voltage V_{drive} at a frequency of f_{TF} is generated by the oscillator to drive the TF. The TF signal is detected by a current-to-voltage (I/V) amplifier and demodulated by the HF2LI (Zurich Instruments) lock-in amplifier, whose output consists of the phase shift ϕ and the mechanical oscillation amplitude A. A built-in phase locked loop (PLL) module is employed to maintain the phase shift to a set point of ϕ_{sp} by changing the driving frequency, which keeps the TF on resonance. The oscillation amplitude is kept at a constant A_{sp} by using a built-in proportional-integral-derivative (PID) controller. In the DAM mode, this PID output, which represents the energy dissipation due to atomic-force interaction, is fed into the z-controller of a commercial AFM (Park XE-70) as the feedback signal to maintain a constant average tip-sample distance. More details of the DAM mode and comparisons with the FM mode can be found in Ref. 68. The distance modulation also leads to the periodic change of MIM signals at the TF frequency. As shown in Fig. 3.2, the MIM-Im/Re signals (proportional to the imaginary and real parts of the tip-sample admittance, respectively) are demodulated at f_{TF} to form the MIM-Im/Re AC outputs of the system.

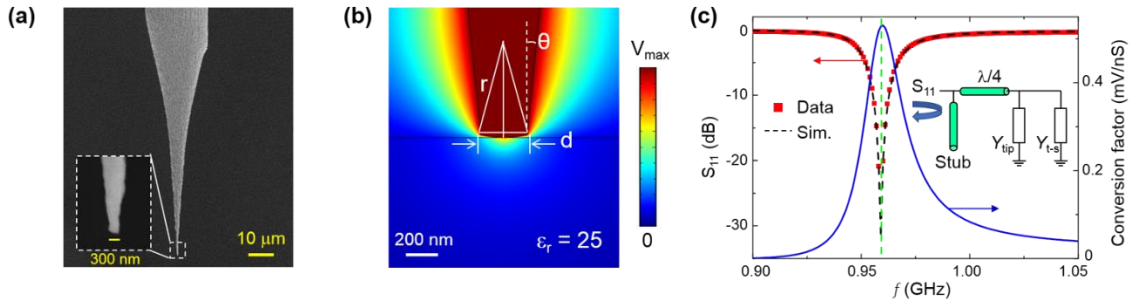

Figure 3.3: (a) SEM image of a typical etched W tip. The inset shows a zoom-in view near the tip apex. (b) Quasi-static potential distribution around the tip and a bulk dielectric sample simulated by the FEA software. (c) Measured S_{11} (red squares) of a TF-based sensor and a fit to the transmission line analysis (black dashed line). The blue curve is the simulated conversion factor between the tip-sample admittance and the MIM output. The inset shows the equivalent circuit of the impedance-match network.

The demodulated MIM AC signals can be quantitatively correlated with electrical properties of samples through a combination of FEA and Fourier transformation. Following the same recipe in Ref. 69, 70, we electrochemically etch a W or Pt/Ir wire with a diameter of 25 μm, as seen in Fig. 3.3a. In this work, we choose a relatively blunt tip to enhance the signal strength, whereas sharper tips are preferred for high-resolution imaging. The tip-sample admittance is computed by commercial FEA software COMSOL 4.4. As shown in Fig. 3.3b, the tip diameter d = 300 nm and the half-cone angle θ = 6° are measured from the scanning electron microscopy (SEM) image in the inset of Fig. 3.3a. As discussed below, the only fitting parameter of the tip geometry is the radius of curvature r (in this case $r \sim 600$ nm) at the apex, which can be determined by measurements on bulk dielectrics. With a good TF feedback control, we have confirmed that the tip condition can be preserved over an extended period of experiments.

At the MIM working frequency near 1 GHz, the metal wire behaves electrically as a lumped element with effective resistance R_{tip} = 1 Ω, capacitance C_{tip} = 0.16 pF, and inductance L_{tip} = 10 nH connected in series. The impedance (Z) match section[13] (inset of

Fig. 3.3c) consists of a flexible quarter-wave cable (Astro-Boa-Flex III, Astrolab Inc.) of 4.8 cm and a semi-rigid tuning stub (UT-085C, Micro-Coax Inc.) of 6.0 cm. As shown in Fig. 3.3c, the measured reflection coefficient S_{11} can be precisely reproduced by transmission-line analysis[13]. With a small load of tip-sample admittance $Y_{t\text{-}s}$, the same modeling can also yield the change of S_{11} as a function of frequency. Taking into account of the input microwave power (~ -20 dBm) and the electronic gain (~ 90 dB), we can plot the conversion factor between the admittance input (in unit of nS) and the MIM output (in unit of mV) in Fig. 3.3c, which peaks at the working frequency of 958 MHz. Using this parameter, $Y_{t\text{-}s}$ simulated by the FEA can be directly converted to the MIM raw signals in a quantitative manner.

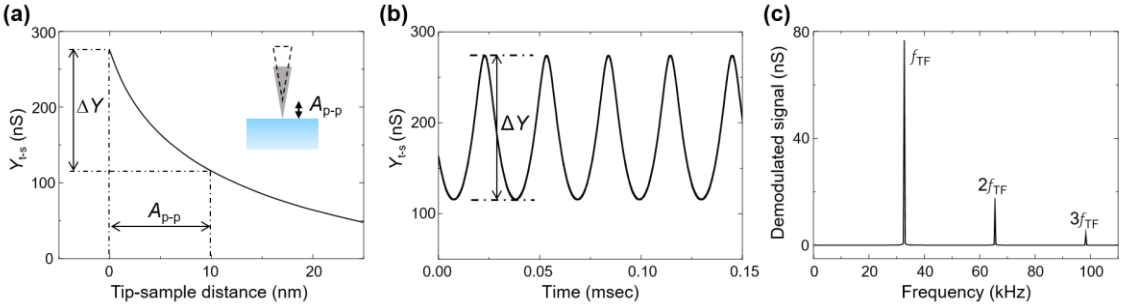

Figure 3.4: (a) Tip-sample admittance $Y_{t\text{-}s}$ on a dielectric sample ($\varepsilon_r = 25$) as a function of tip-sample distance (sketched in the inset) modeled by FEA. The tip oscillates between the contact point and a maximum height of $A_{p\text{-}p}$, resulting in a change of ΔY in the tip-sample admittance. (b) Time dependence of $Y_{t\text{-}s}$, assuming a simple harmonic oscillation of the tip. (c) Fourier spectrum of $Y_{t\text{-}s}$. The amplitude of the first harmonic peak corresponds to the MIM AC signal demodulated by the lock-in amplifier.

Fig. 3.4a shows the simulated $Y_{t\text{-}s}$ as a function of the tip-sample distance based on the tip geometry in Fig. 3.3b. As the tip oscillates between the contact point and a maximum height of $A_{p\text{-}p}$, the tip-sample admittance oscillates accordingly within a range of ΔY in the approach curve. In this work, $A_{p\text{-}p}$ is kept at a relatively large value of 10 nm for a better

tracking of sample surfaces. In Fig. 3.4b, the time dependence of $Y_{t\text{-}s}$ is calculated by correlating the tip-sample distance with the simulated admittance at each moment. In the experiment, the demodulated signals at the fundamental TF frequency, i.e., the first harmonic peak in the corresponding Fourier spectrum (Fig. 3.4c), are used for the MIM AC output. Since the approach curve strongly depends on the local permittivity and conductivity of the sample, the TF-MIM can quantitatively determine these electrical properties after a proper calibration.

3.1.3 Instrument Calibration

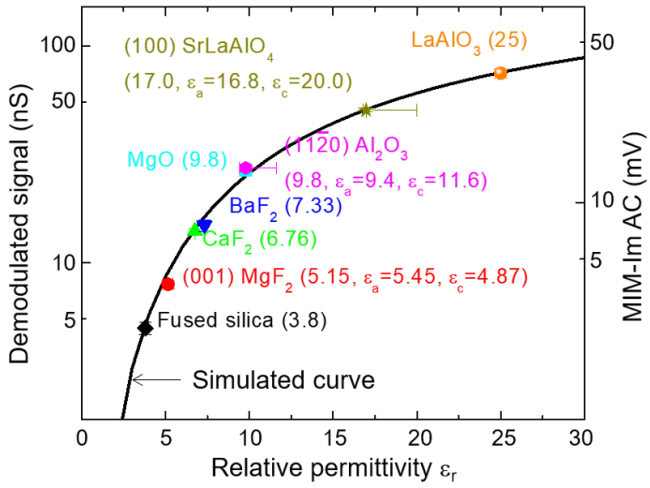

Figure 3.5: Demodulated tip-sample admittance and the corresponding MIM-Im AC signals as a function of the relative permittivity. Materials and the permittivity values are listed next to the symbols. Bars in the vertical axis indicate experimental uncertainties. Bars in the horizontal axis, on the other hand, identify the range between permittivity values at a-axis (ε_a) and c-axis (ε_c) for anisotropic materials. Data points for anisotropic materials represent the effective isotropic permittivity (see the text for details). The solid line is the simulated curve using FEA.

Similar to other quantitative microwave microscopy work[56, 71], our first set of experiment is to calibrate the instrument with various bulk materials. For each sample, an

area of 2 μm^2 is scanned by TF-MIM and the corresponding MIM-Im AC signal is averaged over the area to improve the signal-to-noise ratio. By comparing the measured signals with the FEA results of fused silica (relative permittivity $\varepsilon_r = 3.8$) and $LaAlO_3$ ($\varepsilon_r \sim 25$), we can estimate a radius of curvature $r \sim 600$ nm at the apex. With this fitting parameter determined, the MIM-Im AC signals can be simulated as a function of permittivity of isotropic dielectrics in Fig. 3.5. The experimental data on 8 bulk materials are also plotted in the graph, showing quantitative agreement with the modeling results. For each anisotropic dielectric, we calculate an effective isotropic permittivity by FEA simulation such that the MIM AC response matches that using the actual anisotropic permittivity tensor. Note that for anisotropic samples, the measured value is closer to the permittivity perpendicular to the sample surface, e.g., along the c-axis for (001) surface. Such a phenomenon can be explained by the monopole-like tip geometry, which generates quasi-static electric fields mostly in the vertical direction.

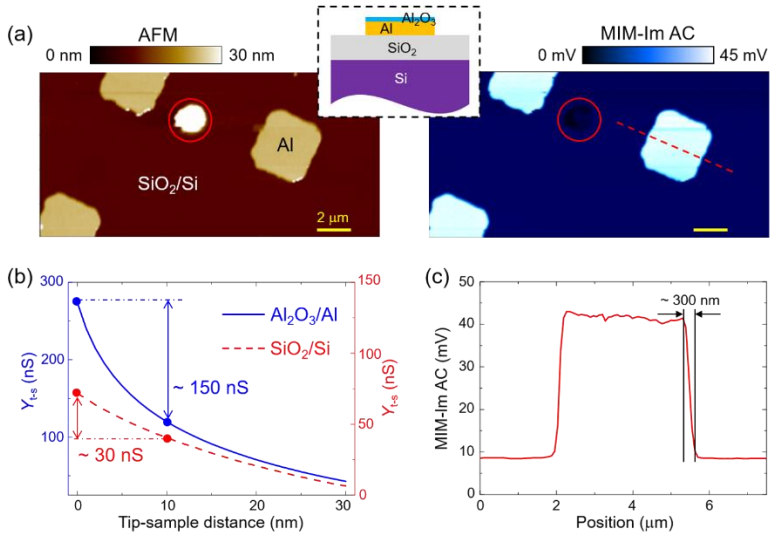

Figure 3.6: (a) AFM and MIM-Im AC images of a patterned Al dot sample measured by the TF-based MIM. The scale bars are 2 μm. The inset shows the sample structure. An insulating surface particle (inside the red circle) shows higher topographic and lower MIM signals than the substrate. (b) Simulated approach curves on the Al dot (solid blue line) and the substrate (dashed red line). (c) Line profile of the MIM-Im AC signal across an Al dot marked in (a), showing the electrical contrast between the two regions and a spatial resolution of ~ 300 nm.

Fig. 3.6a shows the topographic and MIM-Im AC images of the Al/SiO_2/Si sample measured by the same tip as above. The microwave image is clearly dominated by the electrical response since the insulating surface contamination particle (~ 100 nm in height) and conductive Al dots (~ 20 nm in height) exhibit opposite contrast with respect to the substrate. In traditional contact-mode MIM, only the contrast between the Al dots (covered by 4 ~ 5 nm native oxide) and the 100-nm-SiO_2/Si background is meaningful. In TF-based MIM, however, the absolute signals at both regions (~ 40 mV on Al and ~ 8 mV on the substrate) represent local electrical properties and can be readily simulated by the FEA, as shown in Fig. 3.6b. An additional advantage of distance modulation at the kHz range is that the signal does not suffer from the electronic thermal drift in the time scale of

minutes[30]. As a result, no background removal is needed to post-process the MIM-Im AC raw data in Fig. 3.6a. The spatial resolution of ~ 300 nm, as inferred from the line profile across one Al dot (Fig. 3.6c), is consistent with the tip diameter. Owing to the robustness of the DAM operation, high-quality AFM and MIM imaging can be acquired at a fast scan rate (up to 10 μm/s) without obvious scan instability and tip wear.

3.1.4 Quantitative Conductivity Imaging

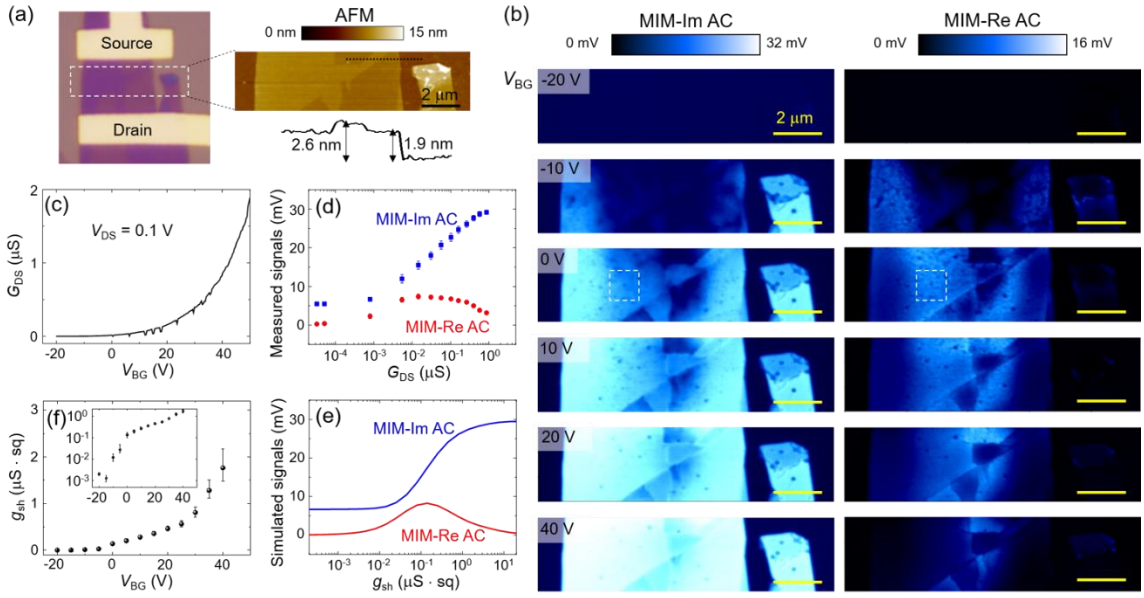

Figure 3.7: (a) Optical and AFM images of a back-gated MoS_2 field effect transistor. (b) Selected MIM-Im/Re AC images at different back gate voltages. All scale bars are 2 μm. (c) Transfer characteristics of the device at a source-drain voltage V_{DS} = 0.1 V. (d) Averaged MIM AC signals inside the dashed square in (b) as a function of source-drain conductance G_{DS}. (e) Simulated MIM AC signals as a function of the sheet conductance g_{sh}. (f) Local sheet conductance versus V_{BG} calculated by comparing (d) and (e). The inset shows the same data with y-axis in log scale.

Finally, we demonstrate that the TF-based MIM is capable of performing quantitative conductivity imaging on nano-devices, which is one of the key areas of application in microwave microscopy. Fig. 3.7a shows the optical and AFM images of an

exfoliated MoS_2 FET device on SiO_2/Si substrate. Details of the device structure and analysis of the contact-mode MIM results can be found in Ref. 51. Here the carrier density in the MoS_2 flake can be globally tuned by the back-gate voltage V_{BG}. In Fig. 3.7b, selected MIM-Im/Re AC images at various V_{BG}'s are displayed and substantial local inhomogeneity is observed in the channel region. To compare the macroscopic transport and microscopic imaging results, we plot the transfer characteristics (source-drain conductance G_{DS} versus V_{BG}) in Fig. 3.7c and MIM-Im/Re AC signals as function of G_{DS} over an area of 1.2 μm × 1.2 μm in Fig. 3.7d. Using the same FEA process above, we can also simulate the MIM-Im/Re AC signals as a function of the sheet conductance $g_{sh} = \sigma \cdot h$, where σ is the conductivity and h is the thickness of MoS_2. The response curves in Fig. 3.7e are similar to that of the contact-mode MIM[9], except that the signals are now absolute values rather than relative contrast over the insulating background. In particular, the MIM-Im AC signals increase monotonically as g_{sh} increases and saturates at both the insulating ($g_{sh} < 10^{-9}$ S·sq) and conductive ($g_{sh} > 10^{-5}$ S·sq) limits. The MIM-Re AC signals, on the other hand, peak at an intermediate $g_{sh} \sim 10^{-7}$ S·sq. Comparing the data in Fig. 3.7d and simulation in Fig. 3.7e, the local sheet conductance within the dashed square in the MIM images can be quantitatively extracted. The results in Fig. 3.7f nicely track the transport behavior in Fig. 3.7c, with deviations due to the strong inhomogeneity in the sample and contact resistance in the device. The error bar indicates the uncertainty of conductivity measurement, which, as shown in the inset of Fig. 3.7f, can be larger close to the insulating and conductive limits as a result of the saturated MIM AC signal. We emphasize that the spatial variation of g_{sh} carries rich information on the material properties and device performance. The ability to quantitatively map out the conductance distribution is therefore highly desirable for fundamental and applied research.

3.1.5 Summary

In summary, we have demonstrated quantitative measurements using tuning-fork-based microwave impedance microscopy operated in the driving amplitude modulation mode. The demodulated MIM AC signal can be simulated by a combination of FEA and Fourier transformation. Excellent agreement is achieved between the modeling and the experiment data on both bulk dielectrics and working nano-devices. Our work provides the pathway to perform quantitative near-field microwave imaging, where absolute signal levels can be readily interpreted as the local permittivity and conductivity.

3.2 BROADBAND MIM

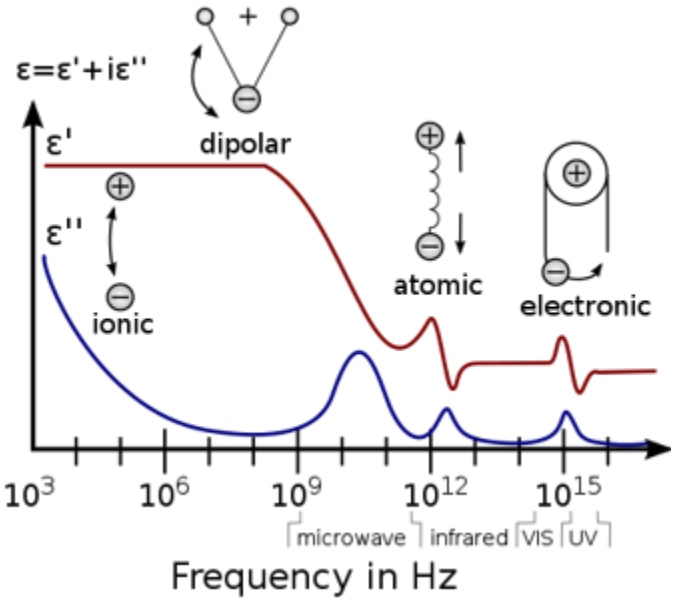

Figure 3.8: Dielectric permittivity spectrum over a wide range of frequencies. Various processes of dipole reorientation are depicted.

For enhanced sensitivity, MIM uses resonant microwave probe that usually works at a single frequency. However, the frequency response of material is of paramount importance as it characterizes the interaction between external ac fields and the electric dipole moments of the sample. Dielectric spectroscopy is an experimental technique that

measures the impedance of a bulk sample (usually at millimeter scale) over a range of frequencies. The detected frequency response of the system includes energy storage and energy dissipation due to different mechanism at the microscopic level. With the frequency of external fields increases (Fig. 3.8), the slow mechanisms drop out in turn, leaving the fast ones contributing to the real part of permittivity ε'. On the other hand, the imaginary part ε'' will peak correspondingly at critical frequencies where electric dipoles of certain kind resonate with stimulus. Specifically, dipolar relaxation and ionic conduction interacts strongly with kHz to GHz electromagnetic waves, while atomic and electronic processes are usually much faster. If the bandwidth of MIM can be expanded over a broader range of frequencies, localized dielectric spectroscopy will be achieved with nanometer scale resolution, revealing frequency response of microscopic entities.

3.2.1 Impedance Match

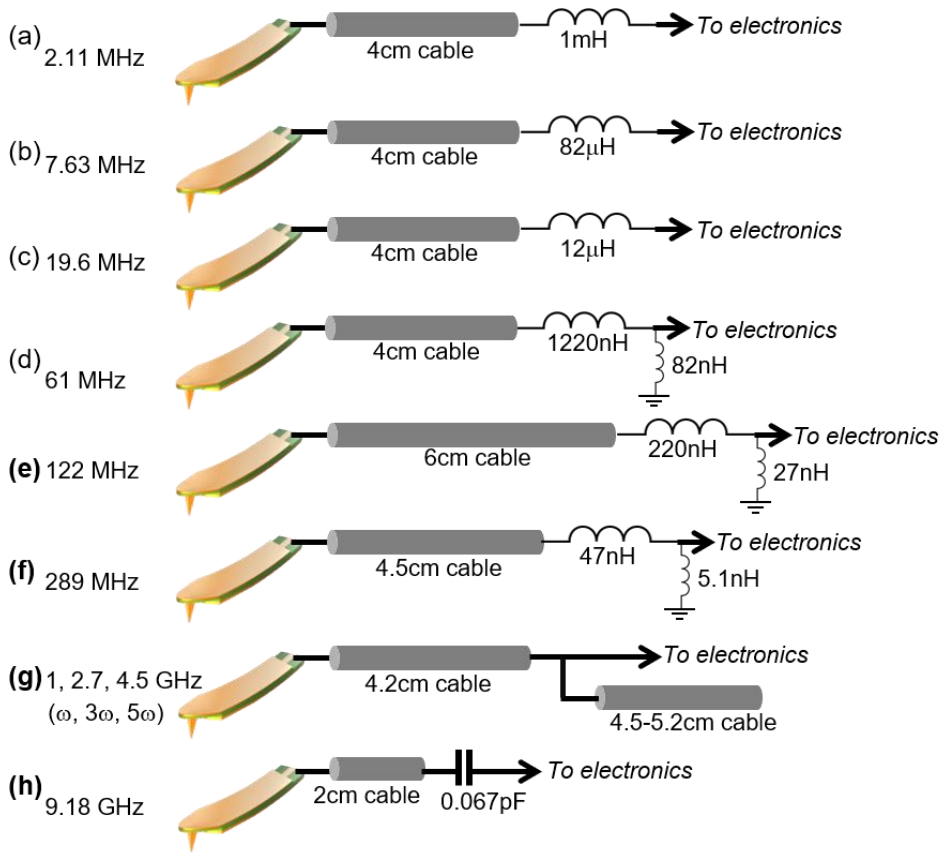

Figure 3.9: Impedance match sections at different frequencies.

To ensure satisfactory sensitivity, the first step to construct a broadband impedance microscope is to find optimized impedance matching network for each desired frequency. As microwave probes are impedance matched to the feed line, the resonant circuit can support not only its fundamental frequency ω but also its higher harmonics, $N\omega$ ($N = 2, 3, 4, ...$). Therefore, it is natural to perform multi-frequency MIM at these harmonics.[60, 72] However, higher harmonics are of little help when frequency lower than fundamental mode is needed. To tackle this problem, I have developed multiple impedance matching

networking optimized for Gen5 probes at a range of frequency (shown in Fig 3.9), thus enabling multiple frequency measurement.

3.2.2 Benchmark and Sensitivity

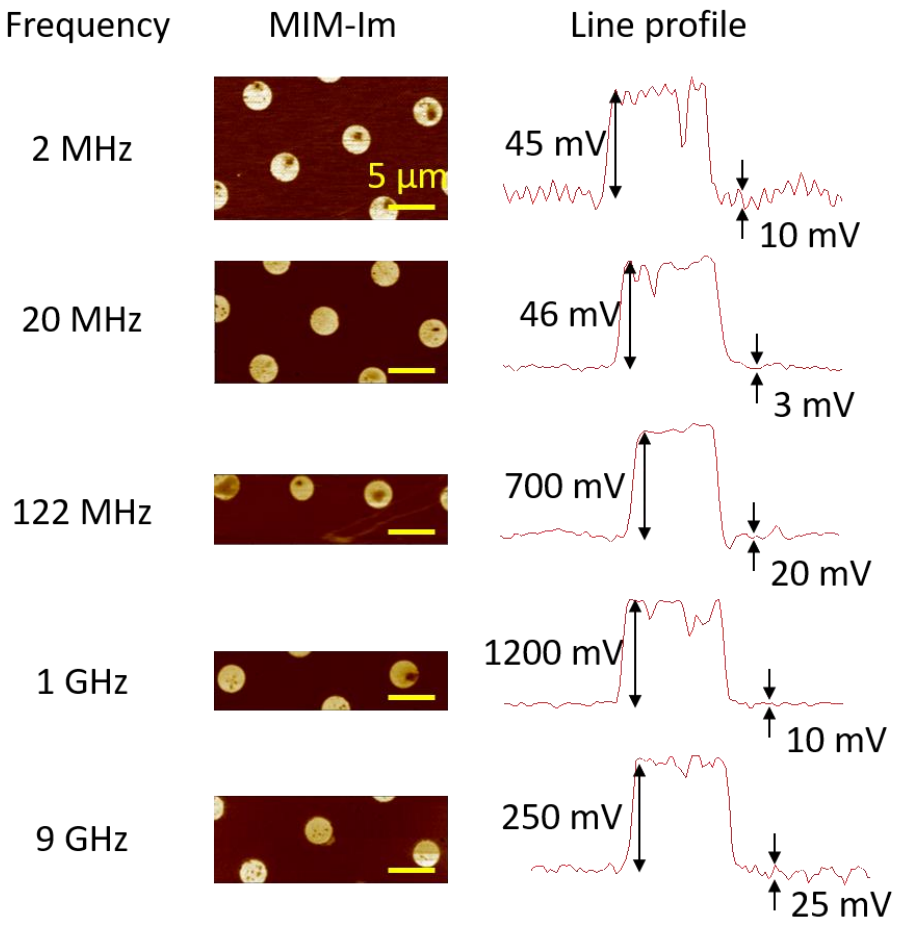

Figure 3.10: Measurement results on Al dot sample at different frequencies. Line profiles across Al dot show signal insensitivity and noise level.

As frequency has been expanded beyond microwave region, the impedance imaging technique is no longer proper to be regarded as *microwave* impedance microscope. Instead, it is named scanning impedance microscope (SIM). As all microwave components have their own working frequencies, we have constructed three sets of SIM electronics to

obtain the best sensitivity around 100 MHz, 1 GHz, and 10 GHz, respectively. For frequencies below 50 MHz, we configured the HF2LI lock-in amplifier from Zurich Instruments to perform the SIM imaging. As a benchmark, we perform SIM imaging on the Al-dot sample at multiple frequencies. While images in Fig. 3.10 show different signal-to-noise ratios (SNRs), the contrast mechanism between aluminum and silicon oxide is similar as neither material shows strong frequency dependence in this regime. Sensitivity of the instrument at different frequencies is shown in Fig 3.11 below.

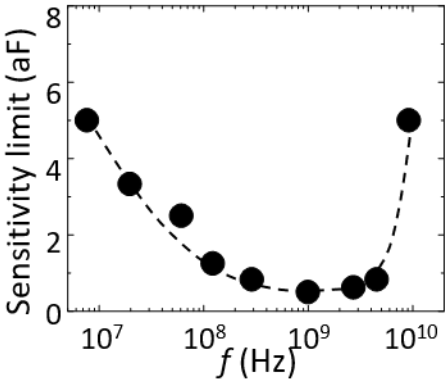

Figure 3.11: Sensitivity of broadband SIM at different frequencies.

3.2.3 Summary

We have developed impedance matching network at multiple frequencies for Gen5 MIM probe and constructed electronics covering a frequency range from 1 MHz to 10 GHz. The performance of broadband SIM is demonstrated using standard samples. In the following chapter, SIM will be utilized to investigate frequency response of nanoscale domain walls in ferroelectric materials.

3.3 Cryogenic MIM

Temperature is an important degree of freedom in physics. Various types of phase transitions set in at certain critical temperatures. The temperature dependence of physical

quantities can be used to determine the underlying mechanism. Therefore, I have incorporated MIM in cryogenic environment for research described in the following chapters.

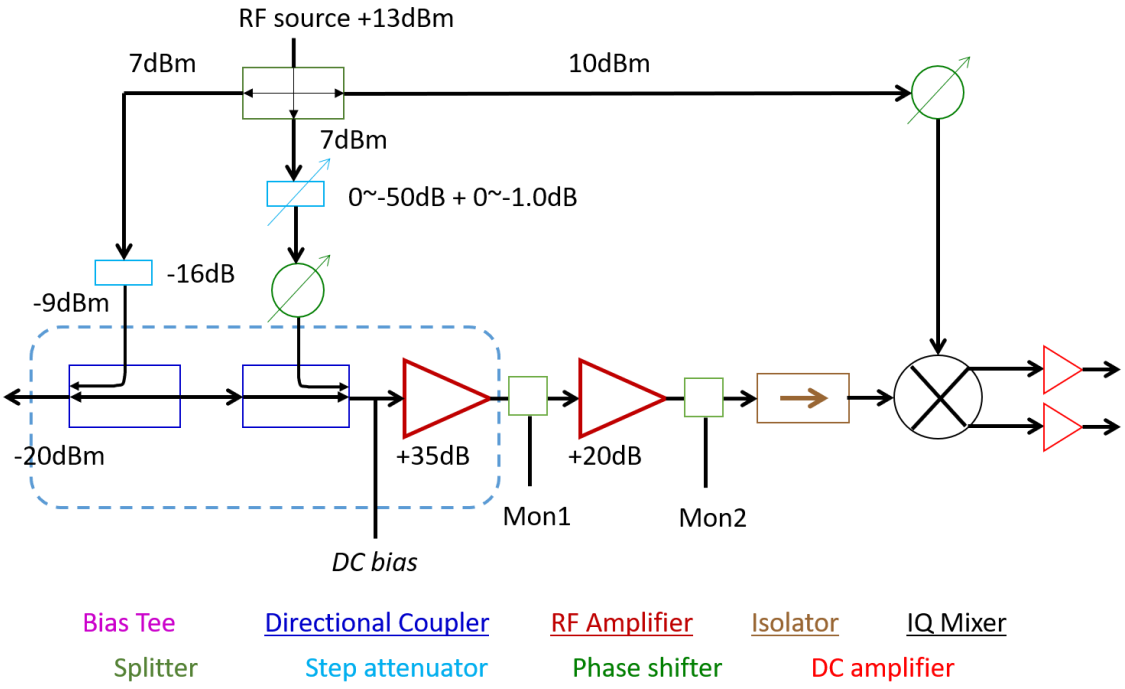

Figure 3.12: Modified MIM electronics for cryogenic measurement.

To combine MIM with a cryostat, one straight-forward method is to simply move the probe and the impedance match section into the chamber and to connect with the MIM electronics using a long coaxial cable. One step ahead is to move the first RF amplifier into the cryostat so that thermal noise of the instrument can be reduced. Accordingly, the two directional couplers in front of the amplifier should also be enclosed in the cryogenic chamber (indicated by the dashed blue rectangle in Fig 3.12). Such configuration is employed in our two types of low temperature system — continuous-flow cryostat and pulse-tube-based dry cryostat.

3.3.1 Cryogenic Environment Setup

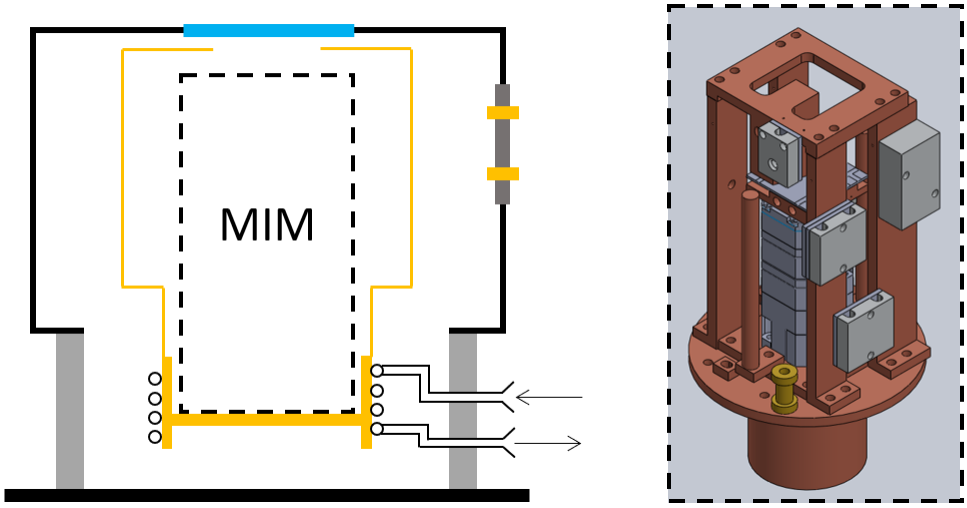

Figure 3.13: Illustration of ST-500 cryostat and MIM insert.

As shown in Fig. 3.13, the continuous-flow cryostat (ST-500 Microscopy Cryostat from Janis) is cooled down by routing cryogen through a long tube inside the vacuum chamber. The system temperature can be varied from 373 K to a base temperature of 10K using liquid helium or 80 K using liquid nitrogen while maintaining low cryogen usage. MIM sitting on the base plate is kept within a radiation shield in order to minimize environmental thermal radiation. The AFM is home-built and consists of coarse positioning system and fine scanning system using micro-positioning modules from Attocube Systems AG. Coarse positioning within a range of $5 \times 5 \times 5\ mm^3$ is achieved by stacking two lateral positioner (ANPx101) on top of a vertical one (ANPz101). Each positioner is equipped with a resistive encoder that monitors the current position. Installed on top of the positioners, the scanner (ANSxyz100) can move the sample over a range of $50 \times 50 \times 24\ \mu m^3$ at 300 K and $30 \times 30 \times 15\ \mu m^3$ at 4 K while the MIM probe is kept fixed in space. Tip-sample separation control can be either open-looped or closed-looped with TF sensors. The top plate of the chamber can be opened for sample and tip exchange.

A viewport with a quartz window allows monitoring the sample position relative to the tip during experiments.

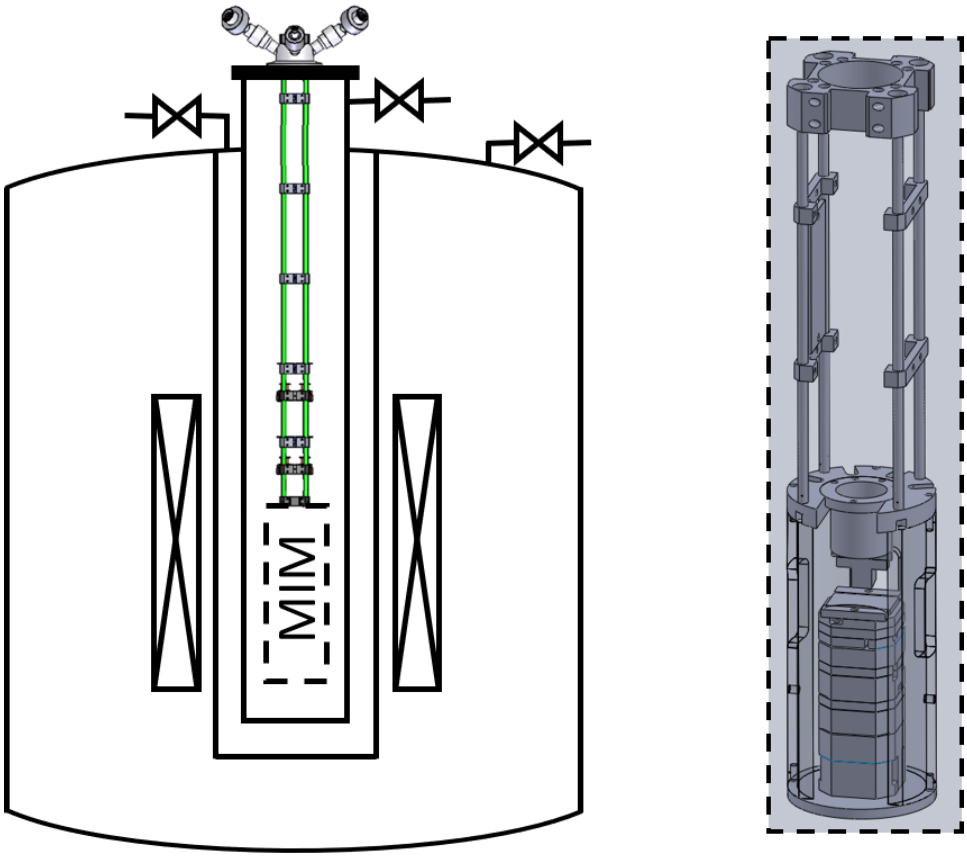

Figure 3.14: Illustration of AttoDry1100 cryostat and MIM insert.

The pulse-tube-based dry cryostat (AttoDry1100 from Attocube Systems AG) in Fig. 3.14 is cooled down by a pulse tube refrigerator. Mechanical vibration caused by the pulse tube coldhead is decoupled from the measurement platform. A superconducting magnet in an isolated vacuum chamber is directly coupled to the coldhead and therefore is the coldest part in the system. The MIM section is made of a similar Attocube assembly as mentioned above and mounted at the bottom of the microscope stick in the so-called inner vacuum space (IV). IV and the magnet is separated by the outer vacuum space (OV). The

pressure of exchange gas (ultrahigh purity helium) in IV and OV can be individually adjusted to control the thermal link between sample and magnet. Fast exchange of tip and sample is feasible as the microscope stick can be pulled out while the magnet is kept at base temperature by keeping OV in vacuum.

3.3.2 Operation of Cryogenic MIM

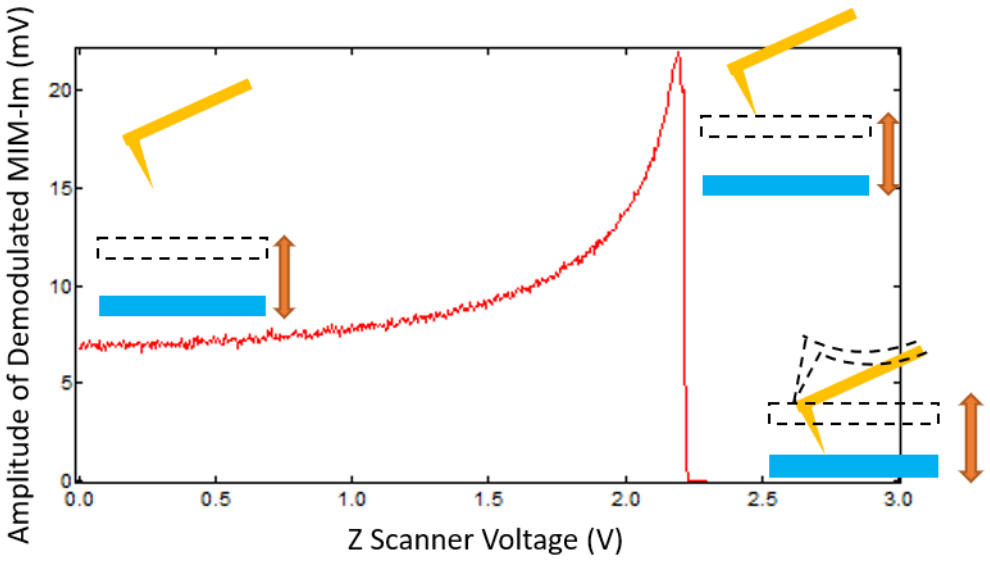

Figure 3.15: Approach curve of demodulated MIM-Im using tapping method.

While tip-sample distance control is feasible with TF sensors, constant tip-sample contact rather than tapping is occasionally needed for certain samples or experiments. To use cantilever probes with open-loop Z position control, one technical challenge is to approach the tip onto the sample surface. As the tip-sample distance d is modulated at a controlled amplitude $A\ of\ 20 \sim 40\ nm$ and a driving frequency $f\ of \sim 400\ Hz$, the tip-sample capacitance is modulated accordingly, and the modulation effect is stronger for small tip-sample distance. Therefore, MIM-Im signal can be demodulated by a lock-in amplifier and the output amplitude indicates the tip-sample separation. As shown in Fig

3.15, as the tip approach the sample surface, the demodulated signal becomes stronger and reaches its maximum when the tip apex and the sample start to contact. As the tip is pushed further against the sample, at some point the tip and the sample will always be in contact in spite of the modulation, leading to zero output signal. Based on this approach curve, the MIM probe can be approached onto the sample surface. As the cantilever has a relatively small spring constant, the tip-sample contact force after approach is acceptable, and the tip can survive extensive scans on relatively flat sample surface with nanometer scale roughness.

Laser interferometer feedback control can be a better option for cantilever probe to work at low temperature and is currently under development.

3.3.3 Calibration of XY Scanner

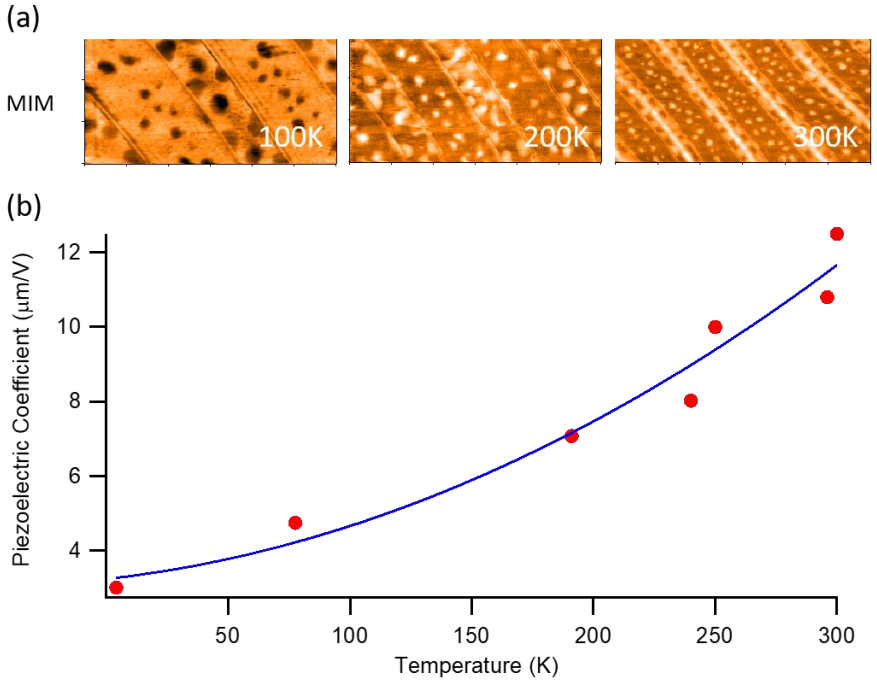

Figure 3.15: Calibration of XY scanner: (a) MIM images of heavy implanted Si at different temperatures. (b) Calculated temperature dependence of piezoelectric coefficient.

Scanners rely on the piezoelectric effect for precise control of the position. The piezoelectric coefficient quantifies the volume change when a piezoelectric material is subject to an electric field and is known to be temperature dependent by the STM community. As a result, calibration of the scanner at various temperature is a must in order to determine the size of features observed by cryogenic MIM. Here, the heavily implanted Si sample is scanned at different temperatures with a voltage ramping from 0 V to 3 V applied by the scan controller to the fast axis piezo (the actual voltage on piezo is amplified by a factor of 15, i.e. 0 V to 45 V). The period of implanted region is ~ 10 μm. Thus the piezoelectric coefficient can be calculated for different temperatures. Note here the coefficient is measured as the ratio of the travel distance over the scan controller output.

3.4 Remarks and Future Directions

In this chapter, I have presented development of MIM including TF-based MIM probes and the enabled quantitative measurements, broadband SIM for study of frequency response, and cryogenic MIMs for measurements at low temperatures and in strong magnetic fields. These advances open doors to research on emergent phenomena in novel quantum materials where interesting physics, including but not limited to conductivity inhomogeneity, happens at a mesoscopic level.

Promising future directions of MIM development include combination of MIM with other external modulation or stimulus (e.g. laser, magnetic field, electric field) and exploration of other degrees of freedom such as dependence of MIM signal on electron spin. Every attempt towards expanded MIM capability can be challenging but at the same time rewarding as new physics is unveiled.

Chapter 4: Emergent Phenomena at Ferroelectric Domain Walls

The phenomenon of ferromagnetism has always been fascinating to human beings since ancient times dated back to more than 2,500 years ago. It is now understood that ferromagnetism is induced by spontaneously aligned orientation of atomic or molecular magnetic moments, which can be switched by application of external fields. The electrical counterpart, namely ferroelectricity, was discovered about a century ago[73] and has been investigated extensively over decades for its potential applications such as non-volatile memories. Ferroelectricity was considered well understood until their real complexity was revealed by experimental techniques with high spatial resolution and polarization sensitivity such as transmission electron microscopy and piezo-force microscopy. Spatially resolved measurements have demonstrated that domain walls (DWs) in ferroelectric materials, which are the nanoscale interfaces separating domains with different order parameters, can host emergent phenomena that are absent in bulk materials. In this chapter, we will use MIM to investigate a family of ferroelectric materials with a focus on the response of DWs to external ac field.[2]

4.1 A Brief Introduction to Ferroelectric and Multiferroic Materials

Before we go into details of the specific ferroelectric materials investigated with MIM, I would like to take a moment to describe the background of research on ferroelectrics so that readers can understand why we choose to investigate DWs in hexagonal manganites.

---

[2] Part of this chapter has been published as X. Wu, U. Petralanda, L. Zheng, Y. Ren, R. Hu, S.-W. Cheong, S. Artyukhin and K. Lai, Science Advances **3** (5) (2017). S.-W.C. and K.L. conceived and designed the experiments. R.H. grew the materials. X.W., L.Z., and Y.R. constructed the electronics and performed the SIM experiment and numerical analysis. U.P. and S.A. performed the theoretical studies. X.W., S.A., and K.L. wrote the initial draft of the paper. All authors were involved in the discussion of results and edited the manuscript.

4.1.1 Ferroelectrics and Multiferroics

For a material to be ferroelectric, its unit cells must contain electrical dipoles that can point in two or more directions, i.e. the centers of positive charges and negative charges have to be separated. Different orientations of these dipoles, or different polarizations, are energetically equivalent. Thus, ferroelectric materials often spontaneously divide into clusters with finite polarizations and such clusters are called domains. Polarization of a domain can be switched by an external electric field and the dependence of polarization on field intensity follows the ferroelectric hysteresis loop displayed in Fig 4.1.

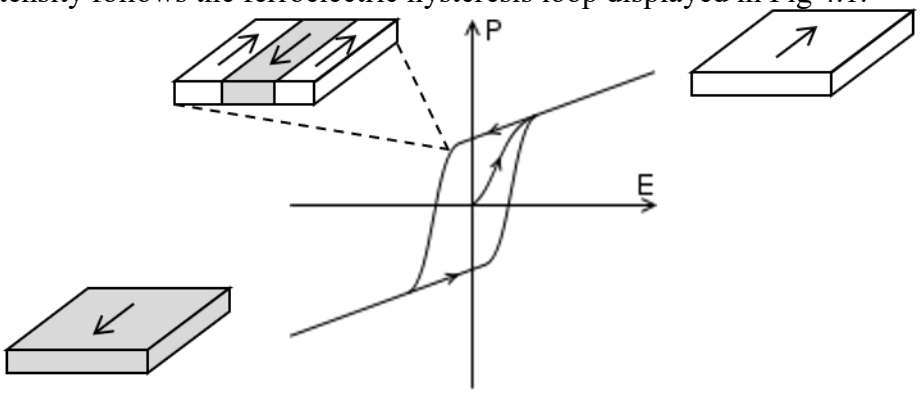

Figure 4.1: Ferroelectric hysteresis loop. The sketch shows the process of switching between two polarizations.

Owing to their strong spontaneous polarization, ferroelectric materials have been widely used in various applications including non-volatile memory, capacitor, thermistor, etc. On the other hand, the importance of magnetic materials as information storage media can never be overemphasized. Since 1950s, extensive attempts have been made to combine the two properties (or even more) into one phase of material called multiferroics (concept demonstrated in Fig 4.2) because the interplay of different ferroic orders can induce novel functionalities. For example, if magnetic properties can be controlled by electric fields in multiferroic materials (green arrows in Fig 4.2), it will be possible to read and write magnetic bits using voltage pulses instead of magnetic-field-generating currents.

Therefore, waste heat and build-up time will be greatly reduced, leading to faster and more energy-efficient data-storage technologies.

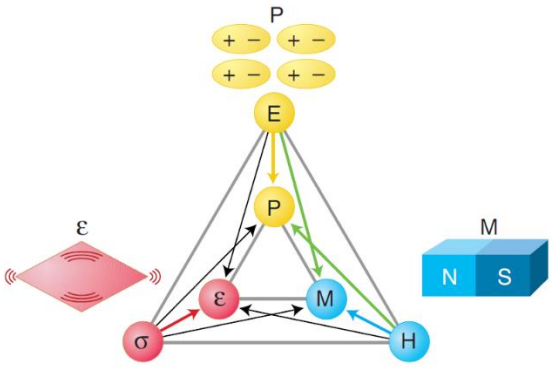

Figure 4.2: Phase control in ferroics and multiferroics. In a magnetoelectric multiferroics, electric fileds can be used to manipulate magnetic moments and electrical polarization can be controlled by magnetic field (indicated by green arrows). Adapted from Ref. 74.

Early efforts to synthesize multiferroic were undertaken through the introduction of magnetic ions in ferroelectric perovskites, in hope that ionic solution created in such way will host long-range magnetic order without losing ferroelectricity. However, few multiferroic materials have been found after decades of searching. It was not until 2000 did the community realize why ferroelectric and magnetic orders are mutually exclusive in perovskite structure.[75] In perovskites, displacive ferroelectricity is induced by off-center ions that occur as the electron clouds of neighboring ions hybridize. This type of ferroelectric order is energetically favorable when the 3d shell is empty. However, partially filled 3d shell is necessary for transition-metal to be magnetic. Once the contradiction is understood, the focus of multiferroic research shifted to the search of new mechanisms that can induce ferroelectricity in a non-displacive way while being compatible with magnetic ordering, including lone-pair mechanism, geometric ferroelectricity, charge ordering, and spin-driven mechanisms.

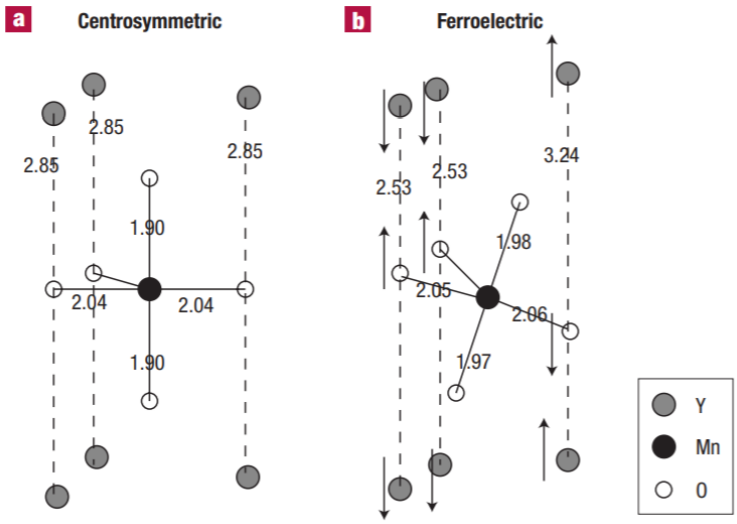

Figure 4.3: Schematic of a MnO_5 polyhedron with Y layers above and below in centrosymmetric (a) and ferroelectric (b) state. Adapted from Ref. 76.

The discovery of pronounced magnetoelectric coupling and geometric ferroelectricity in hexagonal rare-earth manganites (h-$R$$MnO_3$, R=Sc, Y, In, or Dy-Lu) was a breakthrough in the search for new multiferroics. The spontaneous polarization P along the hexagonal c-axis is a by-product of the trimerization of the MnO_5 polyhedra setting in at the structural phase transition around 1000 K, as shown in Fig. 4.3.[76] The primary order parameter, a 2D vector with length Q and azimuthal angle ϕ, describes the shift of apical oxygen atoms when the MnO_5 polyhedra tilt. The coupling between the polarization and trimerization leads to a firm clamping of ferroelectric DWs and structural anti-phase boundaries.[77, 78]

On the other hand, the magnetic order temperature in h-$R$$MnO_3$ is relatively low with $T_c \leq 120$ K. For enhanced magnetic properties or even root-temperature multiferroicity, researchers proposed approaches like Mn substitution with Fe[79-81] and synthesizing materials with strong magnetic ordering into those with electrical ordering[82,

[83]. A more complete review of the evolution of multiferroics can be found for interested readers.[84]

4.1.2 From Domains to Domain Walls

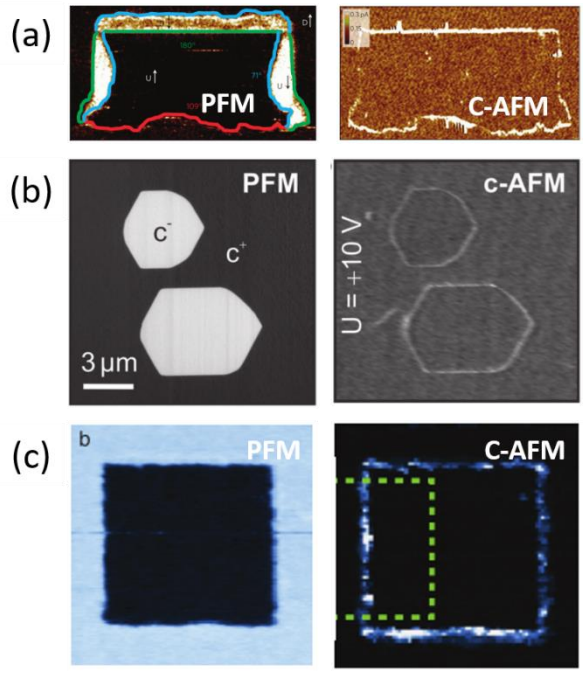

Figure 4.4: Domain wall conduction discovered in (a) $BiFeO_3$ thin film, (b) $LiNbO_3$ single crystal, and (c) $Pb(Zr_{0.2}Ti0_{.8})O_3$ thin film. Adapted from Ref. 85-87.

At the end of the day, the bulk properties of (multi)ferroic materials are determined by individual domains and DWs. As the size of ferroic devices gets down to the nanometer scale, the effect of DWs becomes evident. With the advent of scanning probe microscopy and scanning transmission electron microscopy (STEM), the complex structures of domains and DWs, along with their exotic properties, are revealed with nanoscale resolution. The ground-breaking discovery that DWs in $BiFeO_3$[85] is more conductive than surrounding bulk (Fig 4.4a) triggered a paradigm shift in research of multiferroics. In order to maintain a spontaneous polarization, the bulk ferroelectric domains are usually highly

resistive. Ferroelectric DWs, however, can host anomalous electrical conduction due to the redistribution of carriers, which has indeed been observed by conductive atomic-force microscopy (C-AFM) studies (examples shown in Fig. 4.4b&c).[85-91] The difference of dc conductivity between DWs and domains is usually large for charged walls, where free carriers are accumulated or depleted due to the polarization discontinuity[92, 93], and small for nominally uncharged walls, where secondary effects such as the flexoelectric coupling[94] or the reduction of bandgap[85] may take place. In addition, defects such as excess oxygen or oxygen vacancies can also affect the conductivity of DWs and domains through the change of carrier density[95-98].

4.1.3 Dynamic Responses of Domain Walls

Besides electrical conduction mentioned above, the dynamic responses of domain walls in ferroic materials to external stimuli have received tremendous research interest in recent years as they play an essential role in determining the material properties. In ferromagnets, for example, the supersonic motion of DWs driven by spin-polarized current leads to the exciting development of magnetic racetrack memories.[99, 100] The periodic motion of magnetic DWs around the equilibrium position can be induced by a radio-frequency (rf) current, which has been studied to extract the effective DW mass and to enable low-current device operations.[101] For the electric counterpart, the propagation of ferroelectric DWs under a direct-current (dc) bias has been extensively investigated to understand the switching mechanism.[102-104] On the other hand, the dynamics of ferroelectric DWs under alternating-current (ac) electric fields have not been thoroughly analyzed. While signatures of ferroelectric DW oscillation, e.g., the dielectric dispersion at the microwave regime[105-110], have long been noticed by the scientific community, little is known on the nanoscale dynamics down to the single DW level since conventional bulk

measurements inevitably sum up the responses from domains with different polarizations and walls with different orientations.[111, 112] Spatially resolved studies that address the nanoscale ac response are therefore crucial to explore the underlying physics of such low-energy excitations localized at the DWs, which may be useful for nanoelectronic applications.[113]

The electrical probing of ferroelectric DW response at the MHz – GHz frequency (*f*) regime may be complicated by the presence of mobile carriers, i.e. electrical conduction. Since the contribution from mobile carriers and bound charges at the DWs to the energy loss cannot be separated in a single-*f* measurement, a broadband study is of vital importance to understand the dynamic response of ferroelectric DWs and the corresponding instrumentation has been described in chapter 3.

4.2 Impedance Imaging of Ferroelectric Domain Walls in h-*R*MnO_3

In this section, we report the multi-*f* impedance microscopy experiments on the DWs of single-crystalline rare-earth hexagonal manganites (h-*R*MnO_3, *R* = Sc, Y, Dy–Lu). We show that the effective conductivity of DWs on the (001) surface at GHz frequencies is drastically higher than that at dc, while the effect is absent on surfaces with in-plane polarized domains.

4.2.1 Multi-mode Microscopy on (001) $YMnO_3$

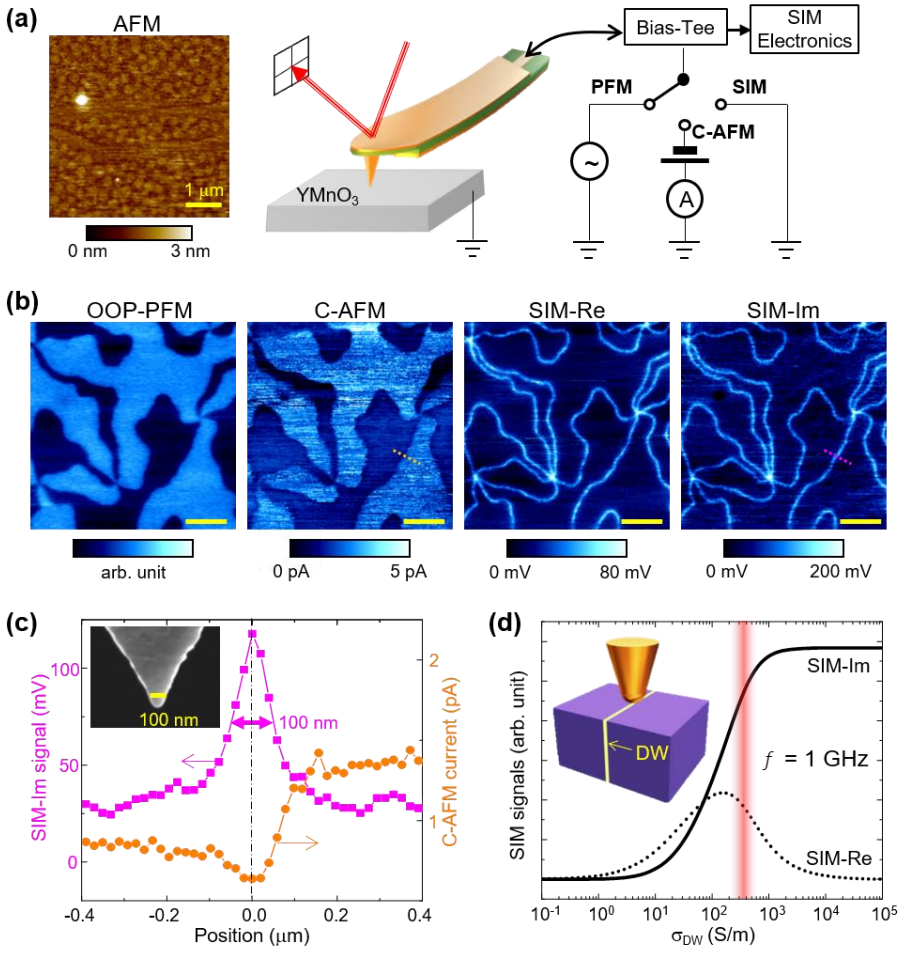

Figure 4.5: Multi-mode microscopy on (001) $YMnO_3$. (a) Schematic of the experimental setup. The shielded cantilever probe is connected to the SIM electronics via a bias-tee, through which a low-frequency ac voltage (95 kHz, 5 V) for PFM or a dc bias (−5 V) for C-AFM can be applied to the tip. The AFM image on the left shows the surface topography of (001) $YMnO_3$. (b) Out-of-plane (OOP) PFM, C-AFM, SIM-Re, and SIM-Im (f = 1 GHz) images acquired on the same area. All scale bars are 1 μm. (c) SIM-Im (purple) and C-AFM (orange) line profiles across a single domain wall centered at position 0.0 μm and labeled as dashed lines in b. The full-width-half-maximum of 100 nm is comparable to the tip diameter, as shown in the scanning electron microscopy (SEM) image in the inset. (d) Simulated SIM signals as a function of the effective DW conductivity. The measured DW signals with a ratio of SIM-Re/Im ~ 0.4 (shaded in red) are consistent with σ_{DW} ~ 400 S/m. The inset shows the tip-sample geometry for the FEA.

Our multi-mode imaging setup on a commercial AFM platform is schematically illustrated in Fig. 4.5a. We first discuss the results on the (001) surface of as-grown $YMnO_3$ samples. With no corresponding topographic features, the cloverleaf-like domain patterns are vividly seen in the out-of-plane piezo-response force microscopy (PFM) data in Fig. 4.5b. Due to its semiconducting band gap of ~ 1.5 eV and slight p-doping from interstitial oxygen[97] during the growth, the as-grown $YMnO_3$ in our experiment shows a room-temperature conductivity σ_{bulk} of ~ 0.3×10^{-3} S/m[77, 114, 115] (Appendix A). This bulk conduction is further modulated by the different surface band bending between up- and down-polarized domains, giving rise to the domain contrast in the C-AFM image under a tip bias of -5 V[77, 115]. In contrast to the uncharged walls in other ferroelectrics[85-87], it was found that the charge-neutral DWs on the (001) $YMnO_3$ surface are more resistive than the adjacent domains[77]. Since the paraelectric phase of $YMnO_3$ is more insulating than its ferroelectric phase, it was suggested that the dc behavior of the DWs closely resembles the corresponding high-temperature high-symmetry states[77].

Different from the dc C-AFM, the scanning impedance microscope (SIM)[66, 116] working at f = 1 GHz measures the local complex permittivity of the material with a spatial resolution of ~ 100 nm determined by the tip diameter d. The input excitation power is on the order of 10 μW[116], corresponding to a low GHz tip voltage of ~ 0.1 V. And the electric field ~ 10 kV/cm at the tip apex is too small to cause ferroelectric switching of the $YMnO_3$ domains[77, 95, 96]. The output SIM-Re and SIM-Im signals are proportional to the real and imaginary parts of the tip-sample admittance, respectively. The SIM images acquired on the same area as above are also displayed in Fig. 4.5b. Strikingly, while the DWs are the least conductive objects on the (001) surface at zero frequency, they exhibit much higher SIM signals than the bulk domains, as seen from the line profiles in Fig. 4.5c. Note that since the tip diameter is much larger than the size of the vortex cores[117], the high SIM

signals at the cores may be a resolution-limited effect due to the summation of adjacent DW signals. We will not, therefore, analyze the SIM data on the vortices.

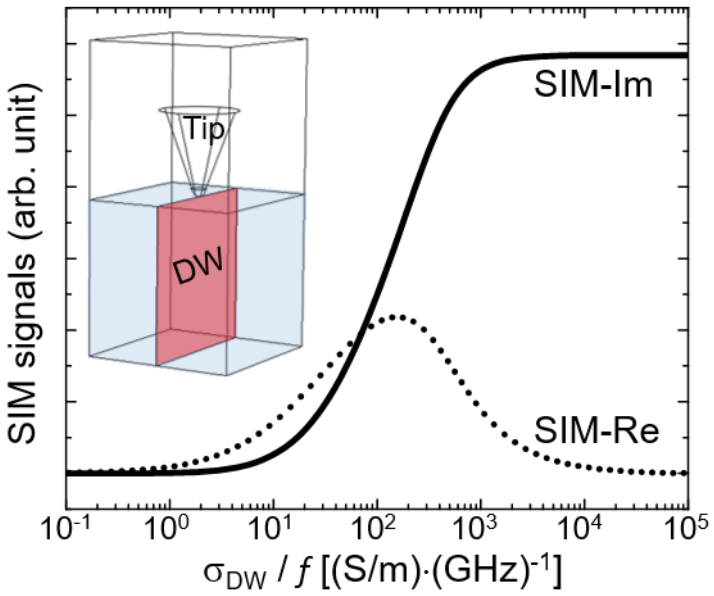

Figure 4.6: Finite-element analysis of the tip-sample interaction. Finite-element analysis (FEA) of the SIM signals as a function of σ_{DW}, which is scaled by the frequency in unit of GHz. The 3D modeling geometry is shown in the inset.

In order to interpret the SIM data as physical quantities, we use finite-element analysis (FEA) to simulate the DW response at GHz frequencies[66]. Near the surface of plate-like $YMnO_3$ crystals, the DWs tend to be perpendicular to the surface for a depth (h) of several micrometers[118], i.e., $h >> d$. As a result, we can model the DW as a vertical narrow slab sandwiched between adjacent domains. To compare results at different frequencies, we characterize the total dielectric loss at the DWs, including both contributions from mobile carriers and DW dynamics, by the effective DW ac conductivity σ_{DW}^{ac}. The FEA results are shown in Fig. 4.6. Here SIM-Re and SIM-Im signals are directly proportional to the real and imaginary parts of the tip-sample admittance (inverse

impedance), which can be computed by the software COMSOL 4.4. Note that the SIM signals saturate at both the low (below 1 S/m at 1 GHz) and high (above 10^4 S/m at 1 GHz) conductivity limits. Due to the small bulk conductivity $\sigma_{bulk} \sim 10^{-3}$ S/m, the SIM response on the bulk domains is in the insulating limit. The quasi-static simulation is invariant when the effective DW conductivity σ_{DW} is scaled by the frequency, i.e., the curves shift to higher σ_{DW} at higher frequency and vice versa. A tip diameter (d) of 100 nm was used in the modeling, consistent with the SEM image at the tip apex and the line profiles in Fig. 4.5c. The domain wall width (λ) on the order of 1 nm was reported in previous transmission electron microscopy studies.[117, 119] We assign $\lambda = 2$ nm so that it is easy to generate a dense mesh in the simulation. In fact, since $d >> \lambda$, the modeling result is invariant with respect to the effective sheet conductance $S_{DW} = \sigma_{DW} \cdot \lambda$. For instance, $\sigma_{DW} = 500$ S/m and $\lambda = 2$ nm lead to $S_{DW} = 1$ μS·sq and an effective sheet resistance $R_{DW} = 1/S_{DW} = 1$ MΩ/sq. Due to the relatively small static dielectric constant $\varepsilon_s = 17$ of the improper ferroelectric h-*R*MnO_3[120], it is unlikely that a possible dipolar relaxation process[121] (ε' drops from ε_s to $\varepsilon_\infty < \varepsilon_s$ and ε'' peaks at $(\varepsilon_s + \varepsilon_\infty)/2$) within our frequency span will substantially affect the simulation result. As a result, we have chosen to interpret the observed impedance contrast in terms of a single parameter, i.e., the effective ac conductivity of the DWs, while making the reasonable assumption of f-independent dielectric constant $\varepsilon = 17$ for both domains and DWs.

Compared with the FEA result (in Fig 4.6 / Fig. 4.5d), the measured DW contrast corresponds to $\sigma_{DW}^{ac} \approx 400$ S/m, which is 5 ~ 6 orders of magnitude higher than σ_{DW}^{dc}. The electrical response of $YMnO_3$ DWs is therefore qualitatively different from that of the ferroelectric lead zirconate (PZT)[122] and the magnetic insulator $Nd_2Ir_2O_7$[42], where the DWs are more conductive than domains at both dc and GHz frequencies.

4.2.2 Control Experiments on Other h-*R*MnO_3

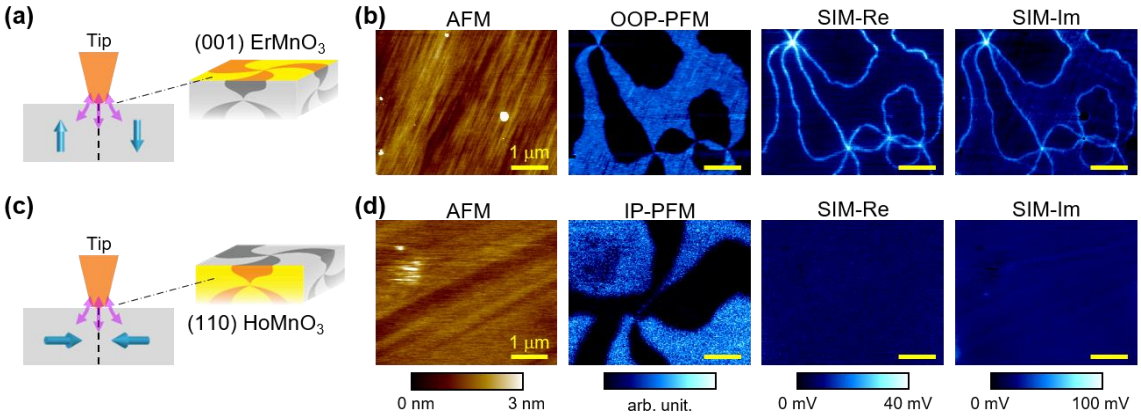

Figure 4.7: SIM experiments on other h-*R*MnO_3. (a) Schematic representation of the tip electric fields (purple) and the out-of-plane polarization (blue) on the highlighted (001) $ErMnO_3$ surface. (b) AFM, out-of-plane PFM, SIM-Re, and SIM-Im (f = 1 GHz) images acquired on (001) $ErMnO_3$. Clear DW contrast can be seen in the SIM data. (c) and (d) are the same as (a) and (b) except that the schematic and the data are for (110) $HoMnO_3$, showing clear domain contrast in the in-plane PFM but no DW contrast in the SIM images. All scale bars are 1 μm.

In order to investigate the generality of the observed behavior, we have also performed control experiments on other h-*R*MnO_3 samples. As shown in Fig. 4.7b, the same DW contrast in SIM data is seen on the (001) surface of $ErMnO_3$, suggesting that the effect is insensitive to the variation of rare-earth elements. The situation, however, is rather different on h-*R*MnO_3 surfaces with in-plane polarized domains. In Fig. 4.7d, no DW contrast in the SIM images is observed on the cleaved (110) $HoMnO_3$ crystal.

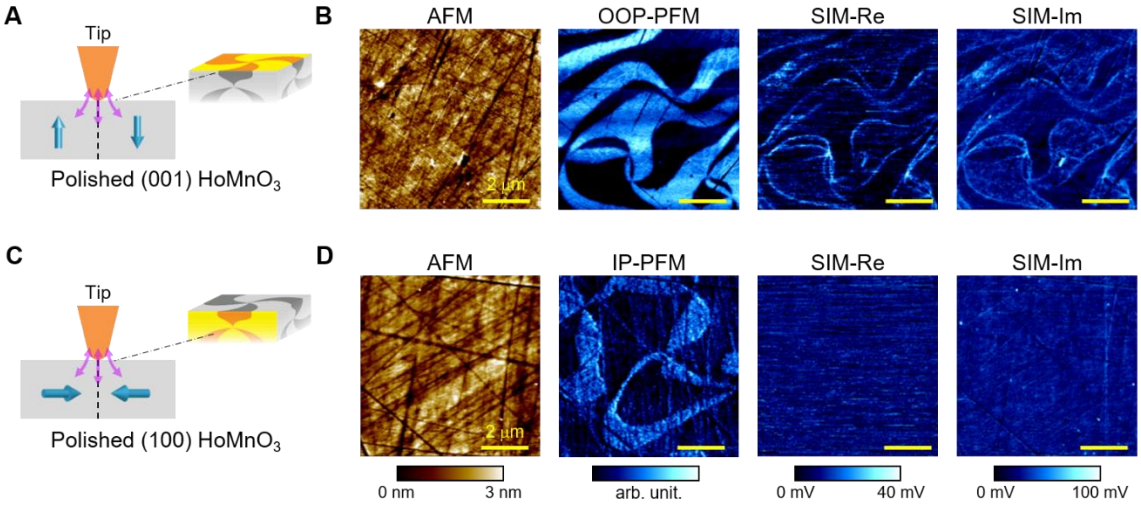

Figure 4.8: SIM data on polished $HoMnO_3$ samples. (a) Schematic and (b) AFM, out-of-plane PFM, and SIM images on the polished (001) surface of $HoMnO_3$ single crystal. (c) Schematic and (d) AFM, in-plane PFM, and SIM images on polished (100) surface cut from the same sample. All scale bars are 1 μm.

In addition to the as-grown $YMnO_3$, $ErMnO_3$ and cleaved $HoMnO_3$ samples presented above, we have also measured other samples to confirm that the results are common to the h-$RMnO_3$ family. In particular, we cut and polished two samples, one with (001) surface and the other with (100) surface, from one single piece of $HoMnO_3$. Note that the SIM data are usually of low quality for polished samples with inevitable scratches and possible damages on the surface. Nevertheless, the images in Fig. 4.8b&d clearly show the appearance and absence of DW contrast on the (001) and (100) surfaces, respectively. In addition, the SIM-Re/Im ratio of the (001) sample (0.40±0.10) is consistent with that on the $YMnO_3$ and $ErMnO_3$ samples. We therefore conclude that the observed DW signals do not depend on the choice of the rare-earth element *R*, and the DW contrast is most prominent on the ab-plane with out-of-plane polarizations[77] and absent on surfaces parallel to the c-axis with in-plane polarizations[123, 124].

DWs inside h-*R*MnO_3 form a complex network that permeates the bulk of the material[125]. On the (110) and (100) surfaces with in-plane polarization, charged DWs are stabilized by the interlocking of the ferroelectric and antiferrodistortive orders. Previous C-AFM work on these surfaces showed that σ_{DW}^{dc} varies continuously as the neighboring domains change from 'tail-to-tail' to 'head-to-head' configurations, presumably due to the accumulation or depletion of p-type carriers.[123, 124] On the other hand, only moderate conductance difference between domains and DWs (within an order of magnitude) is measured on these surfaces.[123] Compared with the FEA results in Fig. 4.6, the contribution due to mobile carriers on the charged walls ($\sigma_{DW}^{dc} << 1$ S/m) is still too small to be detected by the SIM. As a result, the missing DW contrast on the (110) and (100) surfaces at $f = 1$ GHz indicates that the contribution from dipolar loss to the local energy dissipation is also negligible in crystal planes parallel to the polarization axis.

4.2.3 Frequency Dependent DW Response

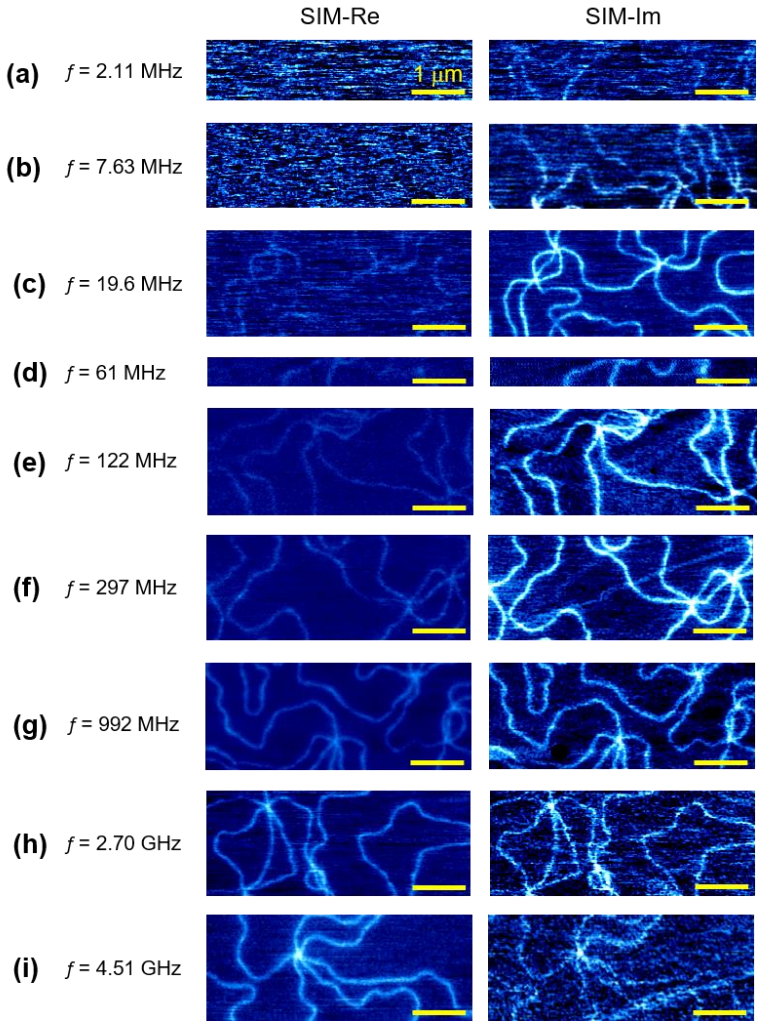

Figure 4.9: Frequency dependent DW response. (a-i) SIM images on (001) $YMnO_3$ at various frequencies. All scale bars are 1 μm. (e) Simulated SIM signals and (f) SIM-Re/Im ratios for different tip diameters, showing the weak dependence on the exact tip condition when the Re/Im ratio is calculated. Note that the *x*-axis is σ_{DW}/f, i.e., the simulation is invariant when σ_{DW} is scaled by the frequency. (g) SIM-Re/Im ratio of the DW signals as a function of *f* in a log-log plot. The constant σ_{DW} contours at 10, 30, 100, 300, 1000 S/m are also plotted in the graph. (h) *f*-dependent σ_{DW} of the (001) $YMnO_3$ DWs. The dash-dot line is a guide to the eyes. The inset shows the same data in the log-log scale.

To further explore the unusual ac response of DWs on (001) $YMnO_3$, we construct multiple SIM electronics to cover a broad spectrum ranging from 10^6 to 10^{10} Hz (Section 3.2). Selected SIM images with clear DW contrast are shown in Fig. 4.9a-i. For each *f*, the SIM-Re and SIM-Im images are displayed with the same false-color scale. Due to the different settings such as input power, amplifier gains, and impedance-match sections of the electronics, the absolute SIM signals cannot be directly compared between different frequencies and therefore are not shown here.

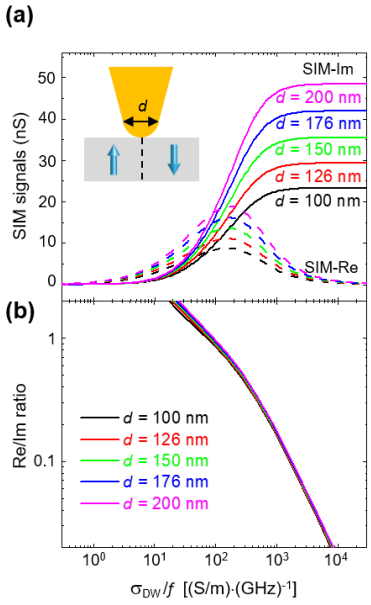

Figure 4.10: Dependence of SIM output on tip geometry. (a) Simulated SIM signals and (b) SIM-Re/Im ratios for different tip diameters, showing the weak dependence on the exact tip condition when the Re/Im ratio is calculated. Note that the *x*-axis is σ_{DW}/f, i.e., the simulation is invariant when σ_{DW} is scaled by the frequency. (c) SIM-Re/Im ratio of the DW signals as a function of *f* in a log-log plot. The constant σ_{DW} contours at 10, 30, 100, 300, 1000 S/m are also plotted in the graph. (d) *f*-dependent σ_{DW} of the (001) $YMnO_3$ DWs. The dash-dot line is a guide to the eyes. The inset shows the same data in the log-log scale.

Moreover, the SIM output is strongly dependent on the condition of the tip apex, as evident from the simulation results in Fig. 4.10a. We have therefore taken the ratios between SIM-Re and SIM-Im signals, which not only cancel out the circuit-dependent factors but also show much weaker dependence on the tip diameter (Fig. 4.10b), for quantitative analysis.

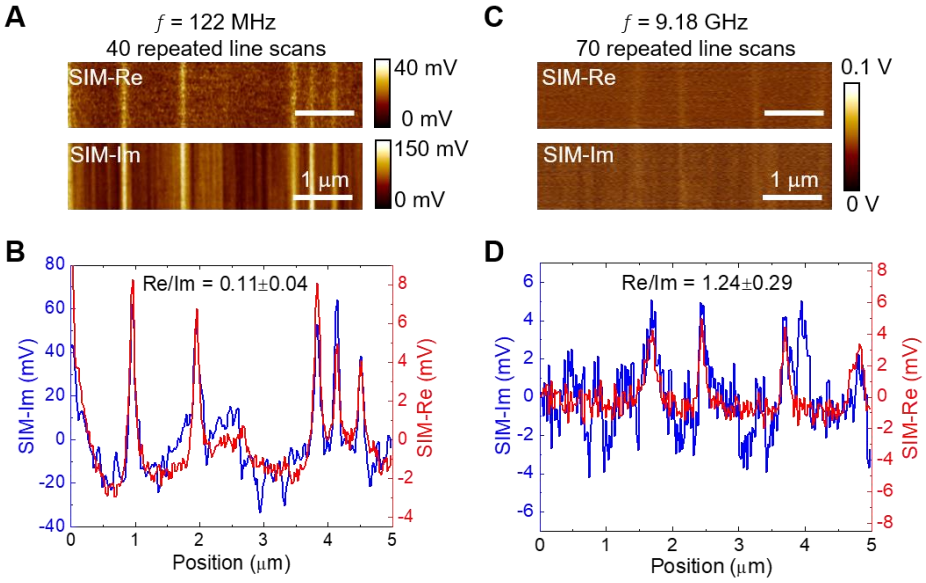

Figure 4.11: SIM experiments with repeated line scans. (a) Repeated SIM line scans at f = 122 MHz and (b) the corresponding averaged signals for calculating SIM-Re/Im with a better signal-to-noise ratio. (c) and (d) show the same results acquired at f = 9.18 GHz. All scale bars are 1 μm.

For the same capacitance contrast ΔC, the admittance change ($2\pi f \cdot \Delta C$) becomes smaller at lower frequencies, which is thus harder to detect by the SIM electronics. The lowest frequency in this work is ~ 2 MHz, below which the signal-to-noise ratio (SNR) is too low for the imaging experiment. At high frequencies, the loss in the coaxial cables and the shielded cantilever sets our upper limit to be ~ 10 GHz, beyond which the SNR is again too low for imaging.

To extract the SIM-Re/Im ratio of the DW contrast, we perform repeated line scans to improve the SNR of the data. Figs. 4.11a&b show the results (f = 122 MHz) of 40 scans on the same line and the plot of averaged SIM signals, respectively. For the f = 9.18 GHz data shown in Figs. 4.11c&d, the DWs are hardly seen in the raw data due to the poor sensitivity. The line averaging method, however, provides adequate SNR such that the SIM-Re/Im ratio can be readily calculated.

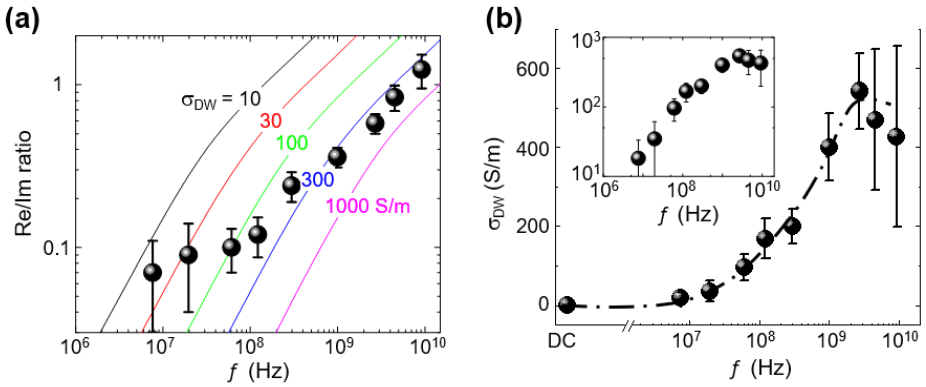

Figure 4.12: Analysis of frequency dependent DW response. (a) SIM-Re/Im ratio of the DW signals as a function of f in a log-log plot. The constant σ_{DW} contours at 10, 30, 100, 300, 1000 S/m are also plotted in the graph. (b) f-dependent σ_{DW} of the (001) $YMnO_3$ DWs. The dash-dot line is a guide to the eyes. The inset shows the same data in the log-log scale.

In Fig. 4.12a, the SIM-Re/Im data are plotted together with the constant-σ_{DW}^{ac} contours from the FEA simulation. Within the experimental errors in Fig. 4.12b, the effective DW conductivity rises rapidly from nearly zero at dc to ~ 500 S/m above 1 GHz and develops a feature not inconsistent with a broad peak around 3 ~ 5 GHz, although the cut-off frequency at 10 GHz prevents us from resolving the full resonance-like peak. Given the very small contribution from Drude conduction of mobile carriers, it is obvious that the bound-charge motion at the DWs, which is microscopically equivalent to the vibration of

DW position, on the (001) surface of h-*R*MnO_3 is responsible for the pronounced ac loss observed in our experiment.

4.3 THEORETICAL ANALYSIS OF DW DYNAMICS IN H-*R*MnO_3

In this section, we perform theoretical analysis on the DW dynamics in h-*R*MnO_3 based on experimental observations in the previous section. Theoretical calculations indicate that the observed behavior is consistent with the dielectric loss due to periodic sliding of the DW around its equilibrium position, i.e., the synchronized oscillation of local polarization and apical oxygen atoms. Our results thus represent a major milestone in understanding the structural DW dynamics in complex systems.

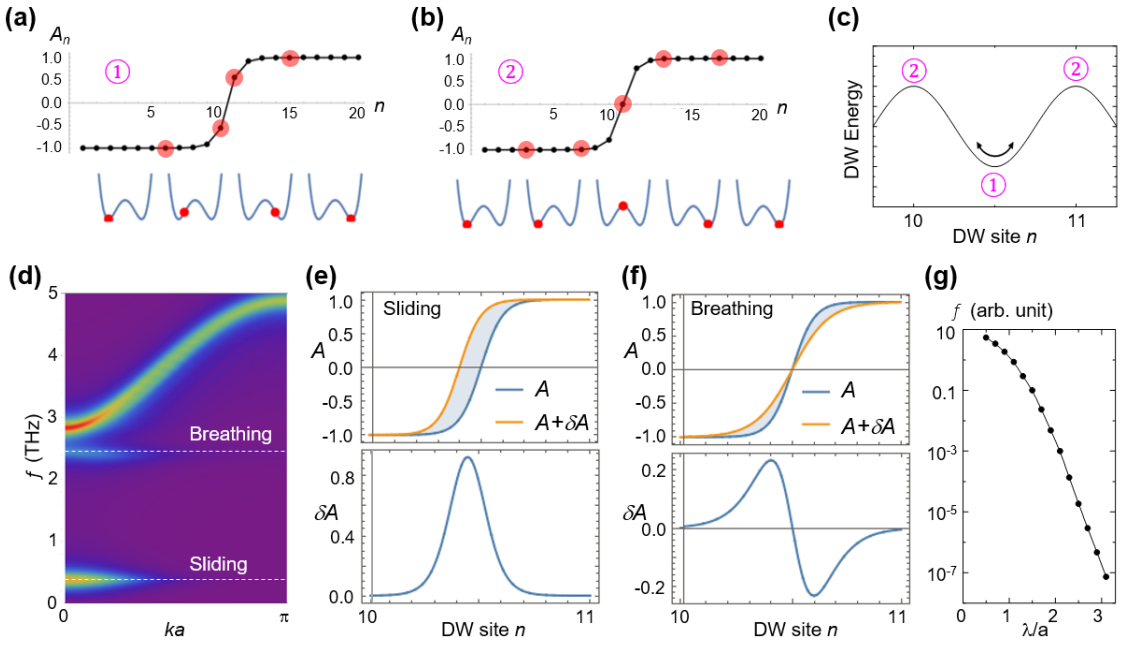

Figure 4.13: Periodic DW sliding in the simplified model. (a) Ground-state configuration of the simplified Hamiltonian (1), with the DW centered between two Mn sites. (b) A high-energy configuration when the domain wall is centered at a Mn site. The schematics in (a) and (b) show the corresponding on-site energies in the double-well potential. (c) Washboard-like potential when the center of the DW slides across different sites. (d) Phonon spectral function in this simple model, showing the non-dispersive sliding mode at the lowest energy, the breathing mode at a higher energy, and the dispersive bulk phonon branch. (e) Mode texture for a lateral shift of the DW position (top) and the corresponding DW sliding mode (bottom). (f) Mode texture for an increase of the DW width (top) and the corresponding DW breathing mode (bottom). (g) Dependence of the DW oscillation frequency on its width.

The starting point to analyze the lattice dynamics in h-RMnO$_3$ is to understand its non-uniform trimerization textures, which were first explained within the long-wavelength Landau theory, using parameters extracted from ab initio calculations.[126] Density functional theory (DFT) calculations predict the lowest optical phonon at ~ 2 THz[126, 127], well above the characteristic frequency in our experiment. On the other hand, the presence of DWs breaks the continuous translational symmetry and introduces a mode associated

with the periodic DW sliding around its equilibrium position, whose energy approaches zero in the continuum model. When the DW width λ is comparable to the lattice constant a, the sliding mode acquires a gap due to the discrete translational symmetry of the lattice. The essential physics of DW dynamics can be captured by a simplified one-dimensional model Hamiltonian:

$$H = \sum_r \frac{(\dot{A}_r)^2}{2m} + b(A_r^2 - 1)^2 + \frac{c}{2}(A_r - A_{r+\delta})^2 - EA, \quad [4.1]$$

where the four terms represent the kinetic energy of the local mode A_r at site r with mass m, the local double-well potential, the nearest-neighbor interaction, and the interaction between the local mode and oscillating external field E, respectively. In the equilibrium, the center of the DW locates in between two adjacent sites, as shown in Fig. 4.13a, so that the mode amplitude at every site is close to the minimum of the ferroelectric double-well potential. When moving to a neighboring unit cell, the DW passes through an intermediate configuration in Fig. 4.13b, where it is centered at the site. The mode amplitude of this configuration corresponds to a maximum of the potential and a high total energy. The energy difference between these two configurations gives rise to the Pierls-Nabarro barrier[128, 129] in Fig. 4.13c that needs to be overcome in order to flip the polarization of a unit cell and move the DW to the adjacent cell. In our SIM experiment, the excitation tip voltage, thus the external field E, is too low to cause any ferroelectric switching. As a result, we only need to consider the linear response of this model Hamiltonian.

The solution of model above reveals two non-dispersive modes localized perpendicular to the DW plane, along with the continuous spectrum of bulk phonons, as shown in Fig. 4.13d. The lowest-energy mode (Fig. 4.13e) corresponds to oscillations of the DW position, whereas the higher-energy breathing mode (Fig. 4.13f) corresponds to oscillations of the DW width. As seen in Fig. 4.13g, the frequency of the DW sliding mode rapidly decreases with increasing λ and approaches zero for $\lambda >> a$, consistent with the free

DW sliding in the continuum theory. The nearly-exponential dependence of the resonance frequency on λ makes it difficult to calculate the frequency precisely from an approximate model, but it is still possible to estimate it by the order of magnitude. This simple model thus illustrates how the low-energy GHz-scale mode emerges from the THz phonon spectrum.

Now we extend the above model to incorporate the principal trimerization amplitude (Q), angle (ϕ), and polarization (P) modes in $YMnO_3$, which are strongly coupled to each other. The structural changes across the domain walls and other non-uniform trimerization textures are primarily described by the modulation of these modes.[126] Since the DW vibration occurs at a frequency much lower than the optical phonons, it is within the error bars of the conventional frozen-phonon calculations.[130] To provide a quantitative estimate, we use the discretized version of the model in Ref. 126, involving all the relevant degrees of freedom, Q, ϕ, and P, and replace the gradient terms with the corresponding interactions between the neighboring sites:

$$H = \sum_{n=1}^{L} \frac{(\dot{Q}_n)^2 + Q_n^2 \dot{\phi}_n^2}{2m_Q} + \frac{(\dot{P}_n)^2}{2m_P} - A_1(Q_n^2 - Q_0^2)^2 - c_1\left((Q_n - Q_{n+1})^2 + \frac{(Q_n + Q_{n+1})^2(\phi_n - \phi_{n+1})^2}{4}\right) - A_2 P_n^2 - c_2(P_n - P_{n+1})^2 - g_1 Q_n^3 P_n \cos 3\phi_n - g_2 Q_n^2 P_n^2. \quad [4.2]$$

In order to approximate the realistic phonon dispersion, we use the corresponding interaction constants and mode masses to fit the phonon band dispersion and band center positions to those determined by the DFT calculations. To calculate the phonons within the model, the Hamiltonian is expanded around the equilibrium DW configuration, up to the terms, quadratic in deviations from the ground state DW, and the corresponding Euler-Lagrange equations are solved as an eigenvalue problem. The finite chain is used with the fixed boundary conditions. The resulting phonon modes with energies E_n and amplitudes $x_{nm}^{(\alpha)}$ of the mode α (α = 1, 2, 3 for modes Q, ϕ, and P) on the site m can be visualized by plotting the phonon spectral function in Fig. 4.14a,

$$A_{\alpha\beta}(k,\omega) = \sum_n \delta(\omega - E_n)\left\langle k\left|x_{nm}^{(\alpha)}\right\rangle\right\langle x_{nm}^{(\beta)}\left|k\right\rangle. \quad [4.3]$$

Here the summation runs over all phonon branches n, $|\mathrm{k}\rangle = \mathrm{e}^{\mathrm{i\,k\,m}}$ is a plane wave with the wave vector k. A scalar product is defined in the usual way, $\langle \mathrm{k}|\mathrm{x_{nm}}\rangle = \sum_{\mathrm{m}} \mathrm{e}^{-\mathrm{i\,k\,m}}\mathrm{x_{nm}}$. And we use a finite-width approximation to a δ-function to describe a finite lifetime. The result looks similar to the phonon dispersion of a periodic crystal, but the translation symmetry breaking due to the DW is manifested in the normal modes at a given frequency not having a single plane wave form with fixed k, but instead a combination of plane waves with different wave vectors.

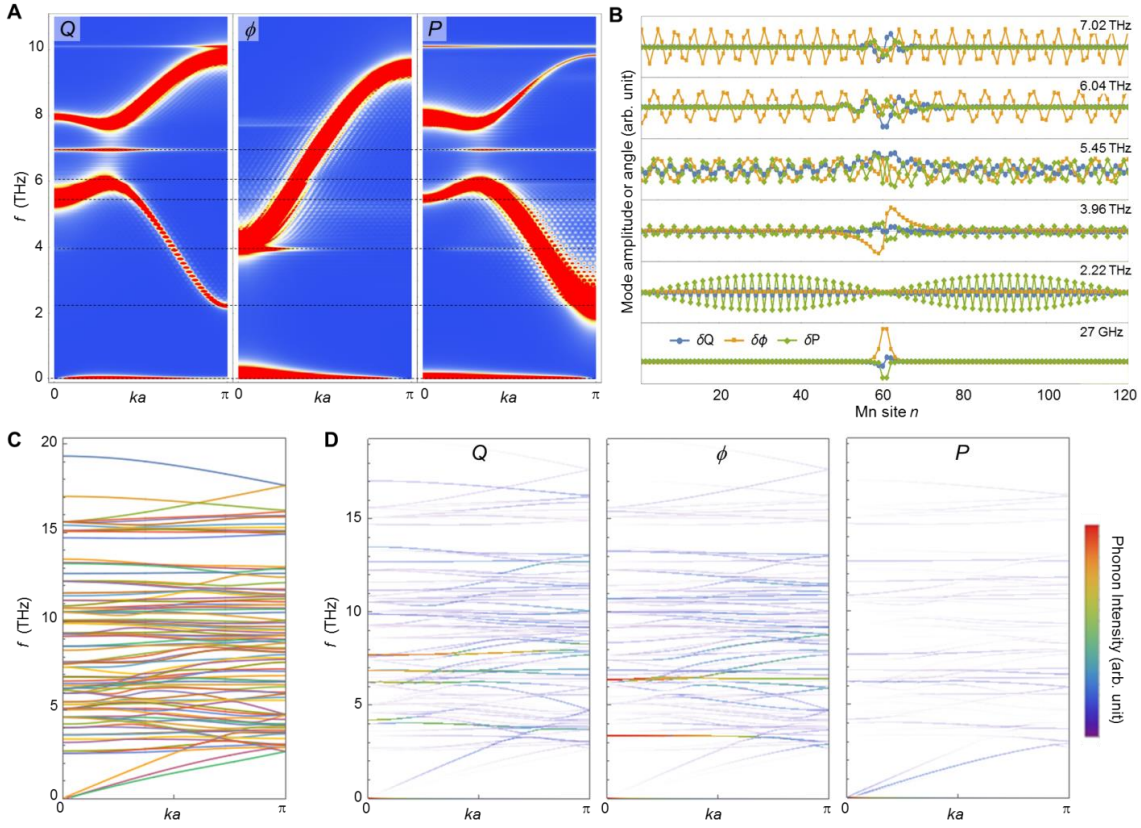

Figure 4.14: First-principles-based model calculations. (a) Phonon spectral function projected to the Q, ϕ, P modes. (b) Oscillation amplitudes of the local modes Q, ϕ, and P are shown for several characteristic phonons at frequencies labeled in A with the dashed lines. (c) Phonon dispersion of $YMnO_3$ in the low temperature $P6_3cm$ structure. (d) From left to right: Contributions of the Q, ϕ, and P modes to the phonon dispersion. The lines are color coded with the relative intensity.

The spectral function projected on the oscillations of Q, ϕ, and P modes resembles the bulk phonon dispersion with the dispersive branches for Γ_2^- and K_3 phonons, along with several non-dispersive branches, corresponding to the phonons localized at the DWs. Here a damping parameter of 20 GHz, consistent with the optical experiments[131], is used in the calculations. The ripples in the false-color maps (Fig. 4.14a) are due to the finite size of the supercell. Fig. 4.14b shows the real-space oscillation of δQ, $\delta\phi$, and δP at several

characteristic frequencies. The lowest branch, appearing in the GHz range, corresponds to the oscillations of the DW position around the equilibrium position, while the localized modes at the THz range correspond to the width oscillations of the Q, ϕ, and P textures. Note that DW-sliding mode is localized only perpendicular to the DW plane and free to propagate within the DWs. Our 1D calculation, therefore, only shows the bottom of the phonon band. The sliding mode with non-zero k_y, k_z wave vectors in the DW plane are analogous to the acoustic waves in elastic media. The inter-site mode coupling terms similar to those with c_1, c_2 in Equation [4.2] give rise to the phonon dispersion for the wave vector components in the DW plane (e.g. yz). These terms give rise to the band of DW-localized phonons, with phonon amplitudes in the DW plane having the oscillating form $\exp(k_y y+k_z z)$, and the bandwidth determined by the respective stiffness constants, and therefore of the same order as the bandwidth of Γ_2^- and K_3 bands in the bulk.

The phonon calculations are performed using frozen-phonon method as implemented in Phonopy software, within the 3×3×2 supercell of the $P6_3cm$ low-temperature unit cell using generalized gradient approximation to density functional theory (GGA, DFT) with a plane wave basis set and projector-augmented waves formalism as implemented in the Quantum Espresso package[132, 133]. The plane wave cut-off of 35 Ry and density cut-off of 300 Ry are used. The magnetic ordering is approximated by A-type antiferromagnetism, which should be sufficient for the present estimates and LDA+U with atomic projection and U = 4 eV was used[134]. The results of the phonon dispersion (Fig. 4.14c) and contributions from the Q, ϕ, and P modes are shown in Fig. 4.14d. The discrete model is then constructed using the force constants calculated, with the energy of the domain wall minimized in the harmonic approximation, which is justified by the small tilts of bi-pyramids from the equilibrium positions in the two domains. Then the energy is

expanded around this state and the phonons are calculated. The results, projected on the phase and amplitude modes of trimerization and on polarization are shown in Fig. 4.14a.

This approach, combining models and first-principles calculations, allows us to treat the bulk and DW-specific phonons within the unified picture and clarifies the physics of the localized low-energy excitation in the SIM data.

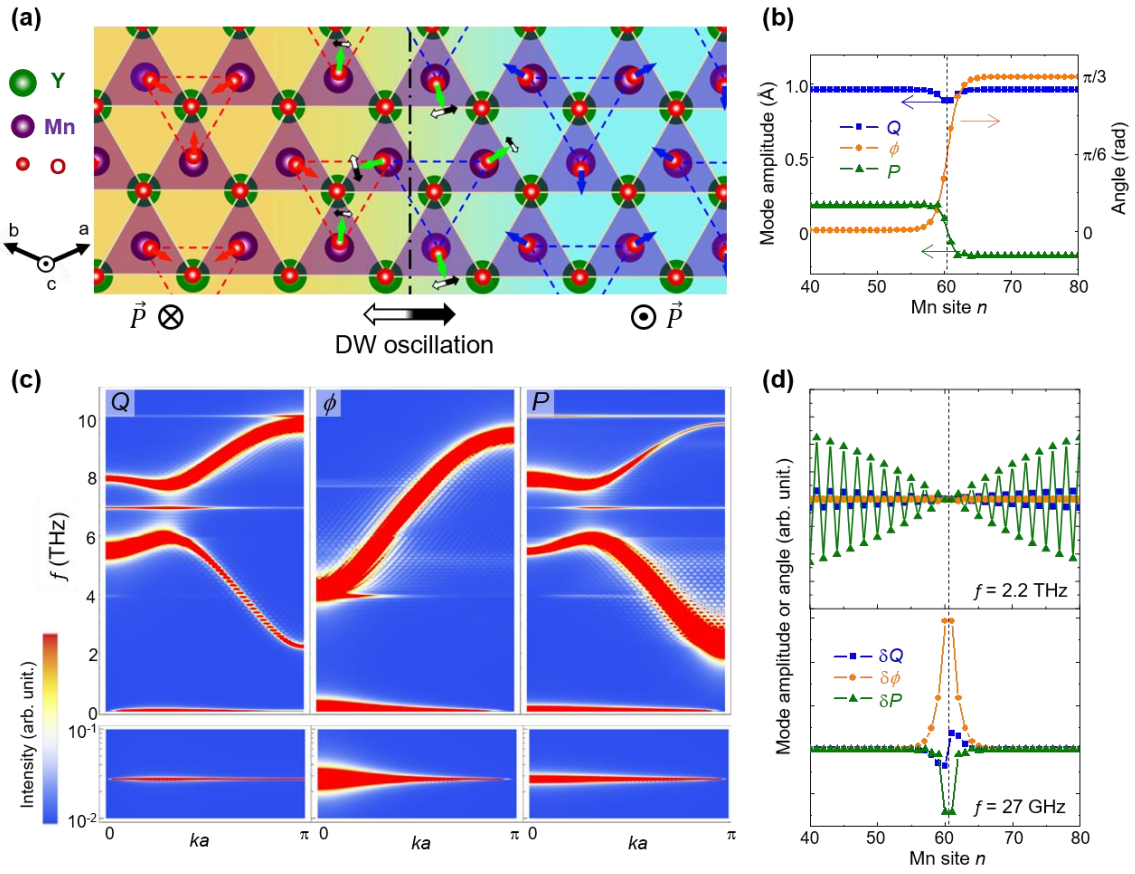

Figure 4.15: DW dynamics revealed by first-principles-based model calculations. (a) Atomistic view of $YMnO_3$ in the (001) plane across the interlocked antiphase boundary and ferroelectric DW. The MnO_5 polyhedra are shaded in purple. The displacements of apical oxygen atoms in the down-domain (left), DW (middle), and up-domain (right) regions are displayed by red, green, and blue arrows, respectively. The trimers are indicated by dashed triangles. The black and white double-headed arrows illustrate the amplitudes and directions of the periodic DW sliding. (b) Ground-state configuration of the three order parameters across the DW obtained by minimizing the model Hamiltonian. (c) Phonon spectral function projected to the Q, ϕ, P modes. The ripples are due to the finite size (120 sites) of the super-cell. The lower panels in the log scale show the spectral intensity of the low-energy non-dispersive branch. (d) Real-space oscillation of δQ, $\delta\phi$, and δP for (top) a regular dispersive phonon at the THz-range and (bottom) the localized DW sliding mode at the GHz-range.

The DW energy centered at the Mn sites is lower than that in between the sites, again giving rise to the washboard-like Pierls-Nabarro barrier. The atomistic view of $YMnO_3$ in Fig. 4.15a shows the synchronized oscillation of apical oxygen atoms and the local polarization during the periodic DW sliding. In Fig. 4.15b, the ground-state configuration by minimizing the model Hamiltonian is plotted for Q, ϕ, and P. The calculated phonon dispersion can be visualized by the phonon spectral function in Fig. 4.15c, where the damping is estimated from optical experiments.[131] Similar to the simplified model, the spectrum contains the usual dispersive phonons originated from the Γ_2^- and K_3 modes in the $P6_3/mmc$ space group[127] and non-dispersive branches, the lowest of which corresponds to the localized DW oscillating mode. In Fig. 4.15d, the order parameter oscillation amplitudes at the lattice sites are plotted for both a regular phonon and the localized mode. Note that our 1D model calculations only capture the bottom of the phonon bands, i.e. phonons with zero wave vector in the DW plane. In real 3D crystals, the vibration of local polarization and oxygen atoms can still propagate with non-zero wave vectors within the DW plane, resembling the acoustic waves in elastic media. The bandwidth of such a DW-acoustic-wave mode is determined by the inter-site coupling strength, and is therefore of the same order as the bandwidth of the Γ_2^- and K_3 modes in the bulk.

4.4 Discussion and Summary

Comparisons between our experimental and theoretical results strongly suggest that the ac response of the h-$R$$MnO_3$ DWs is associated with the DW oscillation mode. First, for DWs on the (001) surface, the vertical component of the oscillating E-field from the SIM tip is aligned with either up- or down-polarized domains in each half-cycle, leading to the periodic motion of the apical oxygen atoms coupled with local polarization and thus

the ac dielectric loss. In contrast, the coupling between the tip *E*-fields and the DW motion on the (110) and (100) surfaces is negligible due to *E* being mostly orthogonal to *P*. Such a 'selection rule' is indeed seen in Fig. 4.7 and Fig. 4.8. Secondly, while the error bars of a full *ab initio* calculation for all 3×30 h-*R*MnO_3 phonons can mask the low-energy mode, our model Hamiltonian taking the essential Q, ϕ, and P modes into account provides an estimate of its frequency that indeed falls into the GHz regime. Further development of the model, such as the inclusion of the next-nearest-neighbor interaction and more phonon modes, may allow a more quantitative comparison with the experiment. Thirdly, our generic analysis of the low-energy DW vibration may explain the dielectric dispersion observed in many ferroelectrics.[105-110] Future experiments on materials with a characteristic frequency well within the range of our SIM, e.g., 0.1 ~ 1 GHz, will allow us to fully resolve the resonance-like peak (similar to Fig. 4.12b), which contains important information such as the DW effective mass. Finally, our model calculations suggest the possible presence of an acoustic mode localized perpendicular to the wall but free to propagate within the DW plane. If confirmed by future experiments, this low-energy excitation, in analogy to the magnonic wave traveling along the magnetic DWs[135] and surface acoustic wave traveling on the surface of piezoelectric materials[136], may be exploited for nanoelectronic applications.

To summarize, by using broadband impedance microscopy, we have observed the drastic increase of effective DW conductivity from dc to microwave frequency on the (001) surfaces of hexagonal manganites, while the effect is absent on surfaces with in-plane polarized domains. First-principles and model calculations indicate that the DW oscillation, rather than the presence of free carriers, is responsible for the ac energy loss and selection rules. Ferroelectric DWs, with their own rich excitations, thus offer a new

playground to explore emergent interfacial phenomena that are not present in bulk domains.

Chapter 5: Imaging Electrical Inhomogeneity in Nanodevices

With sub-micrometer scale distribution of quasi-static fields near the tip apex, MIM excels in characterizing conductivity in buried structures, such as heterostructures and encapsulated devices, which are usually hard to access through traditional transport techniques. In this chapter, I will demonstrate two typical applications of MIM in the above scenario — imaging sketched conductive nanostructures at the heterointerface of $LaAlO_3$ (LAO) and $SrTiO_3$ (STO)[3] and visualizing conductance evolution in electric double-layer transistors (EDLT)[4].

5.1 Sketched Nanostructures at LAO/STO Interface

5.1.1 Introduction

The interface between two insulating perovskites $LaAlO_3$ (LAO) and $SrTiO_3$ (STO) has been in the limelight of material research in the past decade.[137] When 4 or more unit cells (uc) of LAO are epitaxially grown on a TiO_2-terminated STO substrate, a high-mobility quasi-two-dimensional electron gas (q2DEG) forms spontaneously on the STO side of the interface.[138] This system exhibits a plethora of intriguing phenomena including the presence and coexistence of superconductivity and ferromagnetism.[139-142] At the critical LAO thickness of 3 uc, a metastable metal-insulator transition can be controlled using

[3] This part of the chapter has been published as Z. Jiang, X. Wu, H. Lee, J.-W. Lee, J. Li, G. Cheng, C.-B. Eom, J. Levy and K. Lai, Applied Physics Letters **111** (23), 233104 (2017). J.L. and K.L. conceived and designed the experiments. H.L., J.-W.L., J.L., and C.-B.E. fabricated the devices. Z.J. and X.W. performed the MIM experiment and numerical analysis. Z.J., X.W., and K.L. wrote the initial draft of the paper. All authors were involved in the discussion of results and edited the manuscript.

[4] This part of the chapter has been published as Y. Ren, H. Yuan, X. Wu, Z. Chen, Y. Iwasa, Y. Cui, H. Y. Hwang and K. Lai, Nano Letters **15** (7), 4730-4736 (2015). H.Y. and K.L. conceived and designed the experiments. H.Y. fabricated the devices. Y.R. and X.W. constructed the cryogenic MIM and performed the MIM experiment and numerical analysis. Z.C. and H.Y. performed the theoretical studies. Y.R., and K.L. wrote the initial draft of the paper. All authors were involved in the discussion of results and edited the manuscript.

either a global gate voltage applied on the back of the STO substrate[143] or on the top LAO surface using a conductive atomic-force microscopy (c-AFM) tip[144]. In the latter case, the q2DEG can be reversibly written and erased underneath the tip with nanoscale lateral dimensions, enabling the creation and control of a variety of nanostructures such as sketch field effect transistors (FETs)[144-146], photodetectors[147], single electron transistors[148], and quantum dots[149, 150].

Scanning probe microscopy (SPM) has played a key role in understanding the rich physics at the LAO/STO interface. Aside from the aforementioned c-AFM nano-patterning[144-150], the depth profile of the q2DEG has been visualized by cross-sectional c-AFM imaging[151], and the surface charge distribution and electromechanical response have been imaged by electric force microscopy (EFM)[152] and piezo-force microscopy (PFM)[153, 154], respectively. Other properties of the LAO/STO system, including the electrostatic potential, magnetism, and superconductivity, are also locally probed using scanning single-electron transistor (SET) microscopy[155] and scanning superconducting quantum interference device (SQUID) microscopy[142, 156]. On the other hand, one of the most important physical quantities in this system, the local 2D conductivity, has not been directly imaged in a quantitative manner. In this section, we report the patterning and imaging of sketched conductive nanostructures at the 3uc-LAO/STO interface by microwave impedance microscopy (MIM)[116]. The sketched q2DEG patterns can be visualized by the MIM, and the estimated sheet resistance can be extracted using finite-element analysis[66], in agreement with the transport data. The local insulator-to-metal transition is also demonstrated as a function of the tip voltage. Our work lays the foundation to explore various emergent phenomena in oxide interfaces with local electrical probes.

5.1.2 Writing and Cutting Nanowires

The LAO/STO sample in this experiment is prepared as follows. The LAO thin film is deposited on a TiO_2-terminated STO (001) substrate by pulsed laser deposition with *in situ* high-pressure reflection high-energy electron diffraction (RHEED) monitoring. The 3 uc of LAO film is grown at a temperature of 550 °C and O_2 pressure of 1×10^{-3} mbar[157]. After growth, electrical contacts to the interface are prepared by Ar-ion milling 25 nm deep trenches and filling them with Au/Ti bilayer (2 nm adhesion Ti layer and 23 nm Au layer).

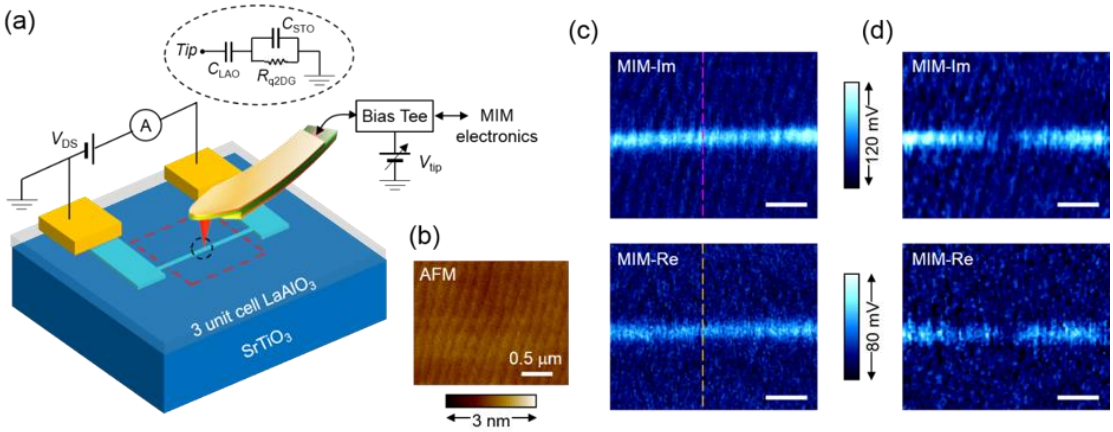

Figure 5.1: (a) Schematic of the experimental setup. Both the microwave excitation and the tip bias are applied to the shielded cantilever tip through a bias-tee. The two-terminal conductance is monitored by a source-drain bias across the Ti/Au electrodes. The inset shows the equivalent lump-element circuit of the tip-sample interaction. Here C_{LAO}, C_{STO}, and R_{q2DEG} represent the capacitance of the LAO layer, STO substrate, and resistance of the q2DEG layer, respectively. (b) AFM image inside the dashed rectangle in (a). (c) MIM images in the same area as (b) after the writing of a nanowire with V_{tip} = +5 V. (d) MIM images after the wire is cut in the middle by a tip bias of -5 V. All scale bars in (b – d) are 0.5 μm.

The MIM measurement is performed on an AFM platform (XE-70, Park Systems) described in chapter 2.[116] As shown in Fig. 5.1a, an excitation signal (10 μW at 1 GHz) is fed to the center conductor of a shielded cantilever tip[54] and the reflected microwave is demodulated to produce the two output signals MIM-Im and MIM-Re, which are

proportional to the imaginary and real parts of the tip-sample admittance, respectively. The GHz frequency is essential for effective capacitive coupling to the buried q2DEG at the LAO/STO interface, as well as to suppress the piezoelectric modes as probed in PFM[153, 154]. The equivalent lump-element circuit of the tip-sample interaction is sketched in the inset. The impedance between the tip and the ground is dominated by the STO substrate when the LAO/STO interface is insulating, and by the LAO layer when the interface is highly conductive interface. In addition to the microwave signals, a DC bias V_{tip} is also applied to the tip through a bias-tee. The two-terminal conductance between the Au/Ti electrodes is monitored by a Keithley source meter with V_{DS} = 10 mV. As an extension of the metal contacts, two rectangular pads are first written with V_{tip} = +5 V. A nanowire is then drawn by scanning the MIM tip with the same bias from one pad to the other. Results shown here are representative of over 20 nanowires created in this fashion using several MIM tips. The abrupt increase of conductance due to the connection of two pads is around 0.1 ~ 1 μS for each micrometer in length of the wire. Similar to previous reports[157], the conductance slowly decreases under the ambient condition, with a characteristic time scale (several hours) much longer than the MIM imaging time (~ 10 min). We note that both water cycle[157] and oxygen vacancy formation[158] may be responsible for such a phenomenon, which is subjected to future studies. The AFM and MIM images of a typical nanowire are shown in Figs. 5.1b and 5.1c, respectively. The step-terrace-like features in the MIM-Im images are due to the topographic crosstalk.[54] On the other hand, with no corresponding observable features in the surface topography, the sketched wire is clearly seen in the MIM data. Note that the two-terminal conductance remains stable during the imaging, indicative of the noninvasive nature of the MIM measurement. The nanowire is then cut by moving the tip with V_{tip} = −5 V perpendicular to the wire, accompanied by a

sudden drop of the current.[144] The MIM images (Fig. 5.1d) taken after the erasing process also show a clear breakage at the cutting point.

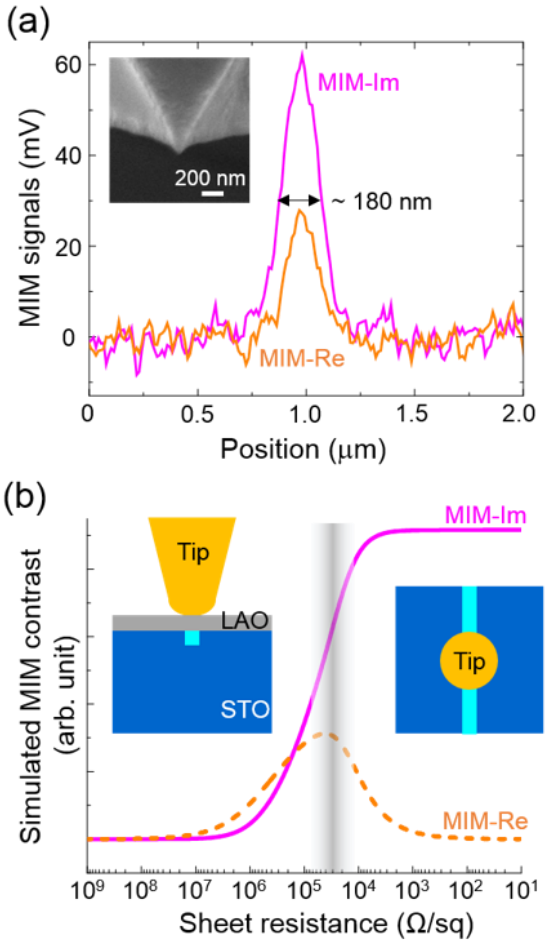

Figure 5.2: (a) MIM line profiles of the nanowire labeled as the dashed lines in Fig. 1c. The inset shows the SEM image of a typical MIM tip. (b) FEA simulation of the MIM contrast (with respect to the insulating background) as a function of the sheet resistance for a 10 nm wire underneath the tip. The signal levels from (a) are consistent with R_{sh} ~ 30 kΩ/sq, as indicated in the shaded area. The insets show the side (left) and top (right) views of the tip-sample configuration in the simulation.

The MIM line profiles of the nanowire in Fig. 5.1c are plotted in Fig. 5.2a. For the > 20 wires measured in this study, the full-width-half-maximum (FWHM) linewidths are

around 150 ~ 250 nm, which is limited by the spatial resolution[116] rather than the actual width of the nanowire. We note that the MIM signal levels, defined as the contrast between the peak values and the insulating background, are different for different tips in the measurements. On the other hand, it has been shown that the ratio between MIM-Im and MIM-Re signals is much less affected by the uncertainty on tip shapes.[43] In the following, we will compare the MIM-Im/Re ratio with the modeling results. To estimate the local conductivity of the nanowire, we simulate the tip-sample admittance by finite-element analysis (FEA)[66] using commercial software COMSOL 4.4. Here the 3 uc LAO is modeled as a 1.2-nm-thick layer with a relative permittivity of 25.[159] The relative permittivity of the STO substrate is 300. The nanowire located on the STO side of the interface is assumed to be 10 nm in width.[144] The radius of the MIM tip in the simulation is 100 nm, consistent with the scanning electron microscopy (SEM) image of a typical probe (inset of Fig. 5.2a) and the FWHM in the MIM line profiles. Under these conditions, the simulated MIM signals[66] as a function of the sheet resistance R_{sh} of the nanowire are plotted in Fig. 5.2b, from which R_{sh} ~ 30 kΩ/sq can be estimated by comparing the measured MIM-Im/Re ratio (around 2:1 for the nanowires) with the COMSOL results.

5.1.3 Comparing MIM and Transport Results

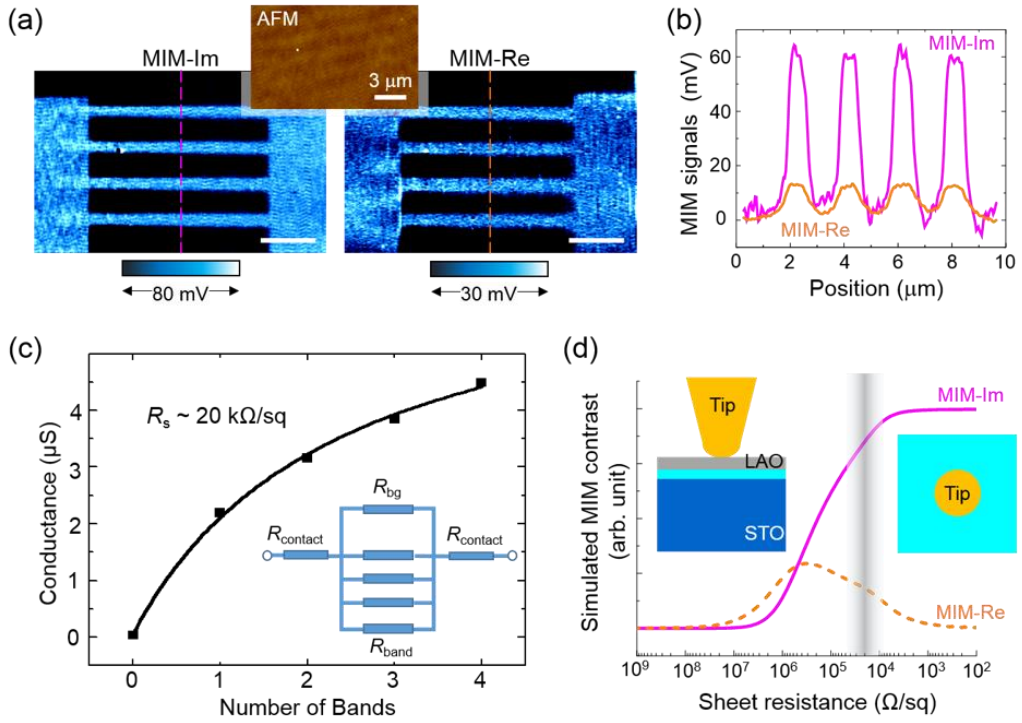

Figure 5.3: (a) AFM and MIM images of four bands across two pads, all written with V_{tip} = +5 V. The scale bars are 3 μm. (b) MIM line profiles across the bands labeled as the dashed lines in (a). (c) Conductance between the electrodes as a function of the number of bands. The solid line is a fit to the experimental data (black squares) using a sheet resistance R_{sh} ~ 20 kΩ/sq. (d) Simulated MIM signals as a function of R_{sh} when the conductive region is much wider than the tip diameter. The insets show the side (left) and top (right) views of the tip-sample configuration in the simulation. The contrast in (b) is consistent with R_{sh} ~20 kΩ/sq, in good agreement with the transport data.

In the single-wire experiment described above, it is difficult to directly compare the MIM and transport results because of the uncertainty in the nanowire width and the contact resistance. To circumvent these problems, we write multiple wide bands, each about 15 squares, with V_{tip} = +5 V across two pre-patterned rectangular pads extended from a pair of electrodes. It is worth noting that the lateral dimension of the conductive region is now greater than the tip diameter. The sketched conductive features are clearly observed in Fig.

5.3a, with measured MIM-Im/Re ratio around 4:1, as seen in the line profiles in Fig. 5.3b. The conductance after the writing of each band is recorded. Assuming that the contact resistance R_{contact} and the background leakage resistance R_{bg} of the device stay constant throughout the measurement, we can express the total resistance across the two electrodes as follows:

$$R_{\text{total}} = 2R_{\text{contact}} + \left(R_{\text{bg}}^{-1} + n \cdot R_{\text{band}}^{-1}\right)^{-1}.$$

As shown in Fig. 5.3c, the experimental data fit nicely to Eq. (1) with a resistance of each band R_{band} ~ 300 kΩ and the corresponding sheet resistance R_{sh} ~ 20 kΩ/sq. Fig. 5.3d shows the simulated MIM signals when the size of the conductive region is much larger than the tip diameter. By comparing the experimental data and FEA results, the sheet resistance extracted from the MIM images is 20 ~ 30 kΩ/sq, which is in excellent agreement with the transport data.

5.1.4 Visualization of the Insulator-to-Metal Transition

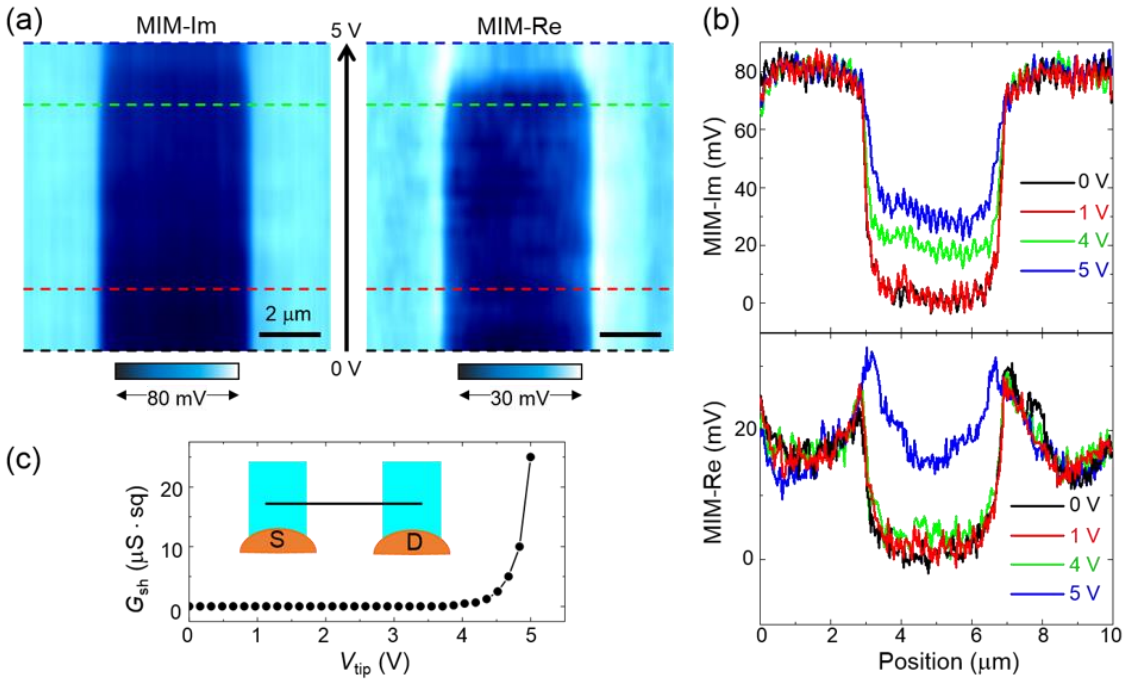

Figure 5.4: (a) MIM signals as the tip repeatedly scans between two pads. The y-axis in the plots represent V_{tip}, which ramps from 0 (bottom) to +5 V (top). The scale bars are 2 μm. (b) Selected MIM line profiles labeled as the dashed lines in (a). (c) Sheet conductance G_{sh} as a function of V_{tip} estimated from the FEA. The conduction at the LAO/STO interface becomes evident above a threshold voltage of +4 V. The inset shows a schematic of the repeated line scans (black line).

Finally, we demonstrate the visualization of the insulator-to-metal transition at the LAO/STO interface by MIM imaging. Fig. 5.4a shows the MIM signals during repeated line scans across two pads when V_{tip} ramps from 0 to +5 V. As seen from the selected line profiles in Fig. 5.4b, the MIM signals on the pads remain constant during this process, whereas the signals on the nanowire region rise as increasing V_{tip}. As illustrated in the insets of Fig. 5.2b and Fig. 5.3d, the conductive region underneath the tip is much narrower in the case of a nanowire than that of a pad. As a result, for the same sheet conductance in these two regions, the MIM-Im signals (proportional to the tip-sample capacitance) will be

larger on the pad than that on the wire. Moreover, we note that the MIM-Re peaks at the nanowire-pad junctions are not fully understood. Using the same FEA simulation described above, it is straightforward to show that the conductance across the two pads emerges rapidly once the tip bias exceeds a threshold voltage $V_{th} \sim +4$ V, as plotted in Fig. 5.4c. This threshold voltage is consistent with previous c-AFM studies[145], as well as the observation that surface charge accumulation on the LAO surface is enhanced for $V_{tip} > +4$ V[152]. The result suggests that the interfacial conductance is due to the field effect through charge writing at the sample surface. We emphasize that the measurement is made possible by the ability of conductivity imaging in the presence of a tip bias.

5.1.5 Conclusions

In conclusion, using a microwave impedance microscope, we have demonstrated the non-invasive visualization of conductive nanostructures at the 3uc-LAO/STO interface. The MIM not only reveals the sketched patterns but also provides a quantitative measurement on the local sheet resistance of the q2DEG, which is in good agreement with the transport data. The insulator-to-metal transition is observed at a threshold tip bias of +4 V, beyond which the local conductivity is strongly enhanced. Our results provide opportunities to study the emergent phenomena at various oxide interfaces.[160, 161]

5.2 Nanoscale Conductance Evolution in Ion-Gel-Gated Oxide Transistors

5.2.1 Introduction

Metal-insulator transitions (MITs), in which the electrical conductivity changes by orders of magnitude[162], are intriguing phenomena that underlie many long-standing physics problems such as unconventional superconductivity[163] and colossal magnetoresistance[164]. The same process is also important for modern semiconductor devices, in which the conductivity is controlled by either chemical doping or electrostatic field effect[165]. Using

ionic liquids[166-168] or gels[169-172] as the gate dielectrics, the electric double-layer transistors (EDLTs) developed in the past few years have demonstrated the ability to modulate the sheet carrier density up to a level much higher than that achieved in conventional metal-oxide-semiconductor field-effect transistors (MOSFETs)[166-173]. Such unprecedented tunability of electron concentration represents a paradigm shift in condensed matter physics research since many carrier-mediated processes, previously only accessible through chemical substitution, can now be studied in the FET configuration with better controllability and less disorder effect.[174, 175] To date, the EDLT structure has been utilized to investigate the field-induced MITs[173, 176-178], magnetic ordering[179, 180], interfacial superconductivity[181-186], and topological surface states[180, 187] in a variety of advanced materials, with an ever increasing list in the foreseeable future.

The remarkable success in the EDLT research has mostly been made possible by transport[166-173, 176-187] and optical[188-190] experiments, in which macroscopic properties of the buried conduction channel at the EDL interfaces are measured. In contrast, it remains technically challenging to obtain the microscopic electrical information in the EDLT channel, which is crucial for the study of nanoscale electronic inhomogeneity in complex quantum materials[191-194] and the local conductance fluctuation in technologically important semiconductors. In conventional EDLT devices, however, the electrolyte-semiconductor interface is usually buried underneath a large droplet of ionic liquid/gel and thus cannot be directly studied by surface-sensitive electrical probes such as conductive atomic-force microscope (C-AFM) or scanning tunneling microscope (STM)[195]. In recent years, a number of local probes, including scanning Kelvin probe microscopy (SKPM)[196], electrostatic force microscopy (EFM)[197], scanning charge modulation microscopy (SCMM)[198], and Raman microscopy[199], have been utilized to image the FETs in a non-contact manner. These techniques, however, only provide indirect rather than direct

information on the nanoscale conductance evolution. A new approach capable of spatially resolving the sub-surface electrical conductivity is therefore highly desirable to advance our knowledge on the electrostatic control of novel materials.

In this section, we report the first real-space electrical imaging of the channel conductance in an oxide EDLT by combining the cryogenic microwave impedance microscopy (described in Section 3.3)[40, 41, 54, 200] and electrolytic gating with ultra-thin ionic gels (thickness < 50 nm), as schematically illustrated in Fig. 5.5a. Thanks to the long-range tip-sample coupling[66], the MIM is capable of performing sub-surface imaging in the presence of a thin dielectric capping layer[41], which is ideal for measuring the ion-gel capped EDLT devices. We have observed the systematic evolution of local channel conductance during the insulator-to-metal transition induced by electrolytic gating. The uneven channel conductance in the presence of a large source-drain bias can also be imaged by MIM and the results are further corroborated by transport measurements and numerical simulations.

5.2.2 Device Structure and Transfer Characteristics

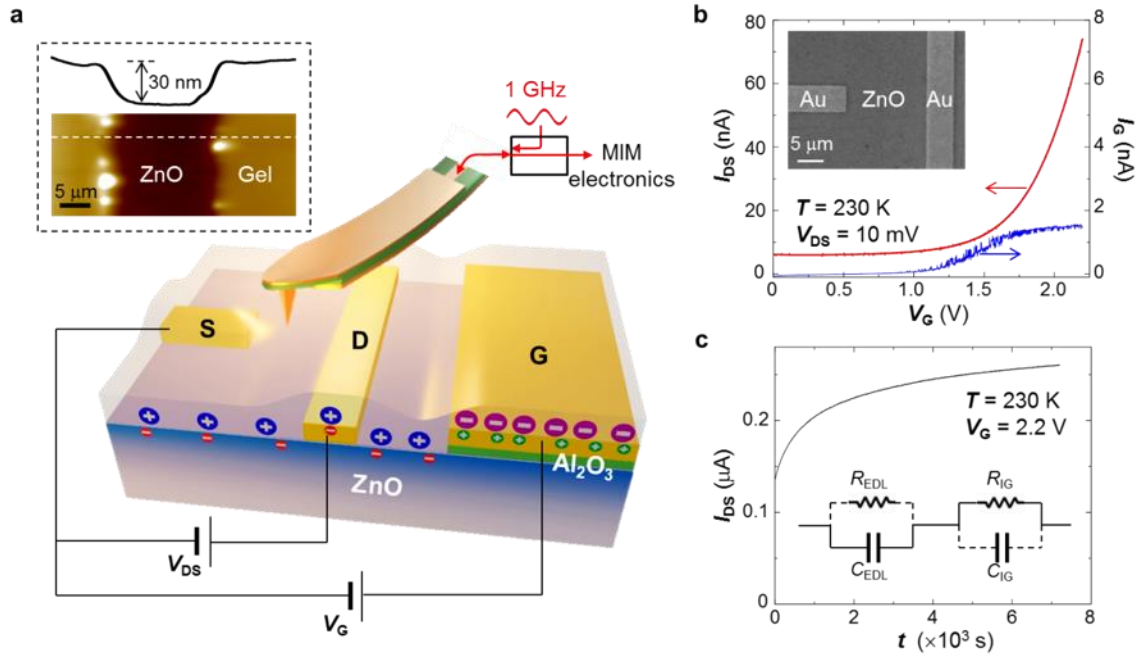

Figure 5.5: (a) Schematic diagram of the EDLT device and the MIM setup. The 1 GHz microwave signal is guided to the shielded cantilever probe and the reflected signal is detected by the MIM electronics. The inset shows the AFM image and a line cut of a typical spin-on ionic gel layer (thickness ~ 30 nm), whose middle part was scratched away for thickness measurement. (b) Transfer characteristics of the EDLT measured at 230 K with V_{DS} = 10 mV. The inset shows the SEM image of the ZnO channel defined by a pair of T-shaped Au contacts. (c) Slow relaxation of the source-drain current at 230 K. The equivalent circuit of the charging process is shown in the inset. For the ultra-thin ionic gel, the dominant circuit elements are the capacitance of the electric double layer C_{EDL} and the resistance of the ionic gel R_{IG}, resulting in a long time constant on the order of 10^4 sec.

As a prototypical semiconducting oxide extensively studied in the EDLT configuration[167, 173, 201, 202], ZnO was used as the material platform in our experiment. The EDLT channel was defined by a pair of T-shaped Au electrodes for easy comparison between macroscopic transport and microscopic imaging, as shown in the scanning electron micrograph (SEM) in the inset of Fig. 5.5b. The T-shaped source/drain electrodes

were patterned on the ZnO substrates (c-cut crystals from MTI Corporation) using standard electron beam lithography. A large area gold pad (60 nm thick), which served as the side gate electrode, was deposited on an Al_2O_3 (100 nm thick) isolation layer. Different from the vertical metal-dielectric-semiconductor structure in conventional MOSFETs, the configuration of side metal gating provides the opportunity for scanning probe microscopy directly from the top of the channel without being shadowed by a top metal electrode. An optimized ionic gel solution [DEME-TFSI-based, N,N-diethyl-N-(2-methoxyethyl)-N-methylammonium bis-trifluoromethylsulfonyl)-imide from Kanto Chemical Co.] was spin-coated on the device with a speed of 6000 rpm, followed by a vacuum baking at 80 ºC for 12 hours. As confirmed by our AFM measurement, the gel thickness was in the range of 30~50 nm, which is ideal for MIM imaging with a spatial resolution on the order of 100 nm. Fig. 5.5b shows the typical transfer characteristics of ion-gel-gated EDLTs with a source-drain bias V_{DS} = 10 mV. The measurements were performed at 230 K, which is higher than the glass transition temperature (T_g ~ 180 K)[173] to allow ionic motion but is low enough to avoid large leakage and irreversible electrochemical effects[202]. The gate dependence of the source-drain current (I_{DS}) clearly indicates that the EDLT can be turned on beyond a threshold voltage V_{th} ~ 1.5 V with a negligible gate leakage current (I_G) below 2 nA. Note that we have studied samples with other contact configurations and the results were qualitatively the same.

The good transfer characteristics and small leakage current suggest that the ZnO EDLT gated by an ultrathin ionic gel can still function as a normal transistor and induce the insulator-to-metal transition inside the channel. However, it should be addressed that the gate response of this device is relatively slow, as compared to ionic-liquid-gated EDLTs. While the actual distribution of ions in the gel can be quite complicated, an order-of-magnitude estimate of the gate response time can be obtained by examining the

equivalent circuit in the inset of Fig. 5.5c. At T = 230 K, the series resistance of the ultrathin ionic gel (R_{IG}) estimated from the gate current is about $10^9 \sim 10^{10}$ Ω, much higher than that of the bulk ionic liquids/gels. Assuming a capacitance per unit area on the order of 10 μF/cm^2, as in previously reported ZnO EDLTs[173], the effective electric-double-layer capacitance C_{EDL} of this millimeter-sized device is about 10^{-6} F. As a result, the time constant ($\tau = R_{IG} \cdot C_{EDL} = 10^3 \sim 10^4$ sec) of this ion-gel-gated EDLT is very long, i.e., it typically took several hours or even longer for I_{DS} to reach the true equilibrium state, which was indeed observed in the time dependence of I_{DS} in Fig. 5.5c.

5.2.3 Distribution of Local Conductance in EDLT

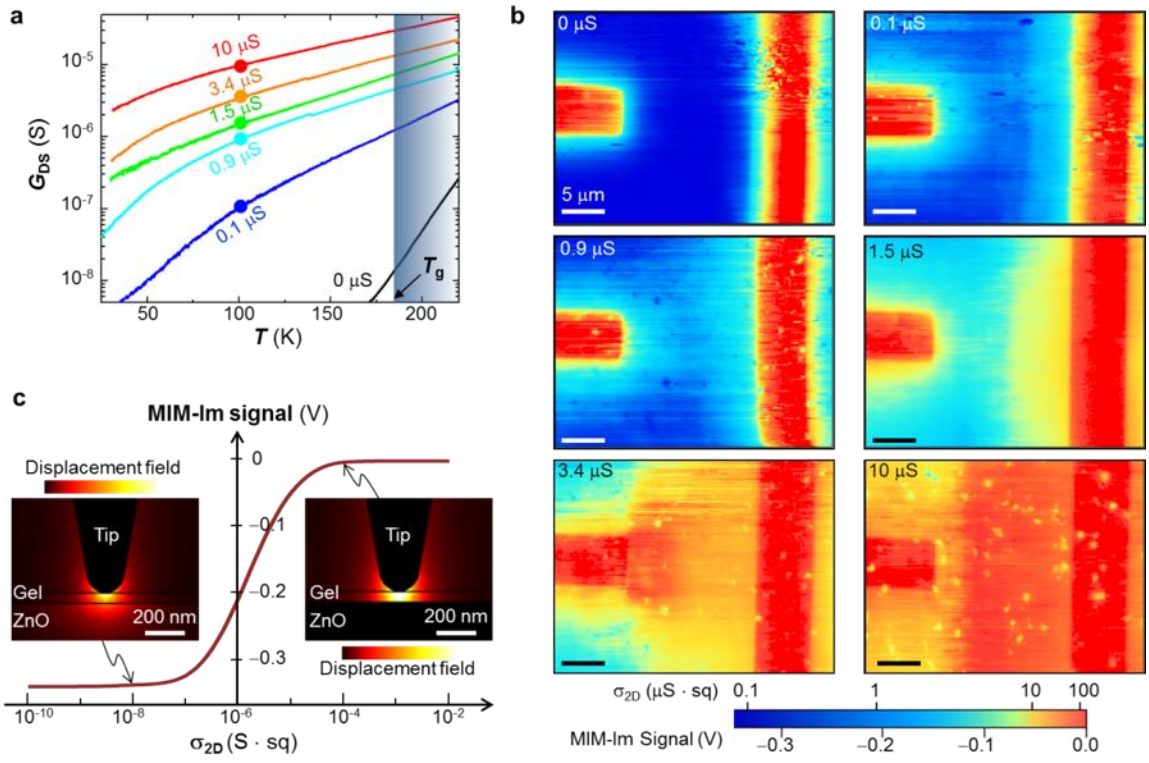

Figure 5.6: (a) Temperature dependence of the channel conductance G_{DS} (V_{DS} = 10 mV) as the device was gradually turned on. The G_{DS}'s at 100 K are labeled on each curve. As temperature decreased from 230 K (shaded region), the ionic motion slowed down and completely stops below T_g ~ 180 K. Electron transport through the ZnO surface, however, was not affected by the glass transition of the ionic gel. (b) MIM-Im images with different G_{DS}'s at 100 K. Some surface particles with lower MIM signals, whose locations change from cool-down to cool-down, can be seen on the device (Supporting Information S3). The false color scale shows both the measured MIM signals and the 2D sheet conductance σ_{2D} simulated from finite-element analysis (FEA). All scale bars are 5 μm. (c) FEA simulation of MIM-Im signals as a function of σ_{2D} at the gel-ZnO interface. The maps of the quasi-static 1 GHz displacement field amplitude (D = εE, where ε is the permittivity and E the electric field) at the insulating (left, $\sigma_{2D} < 10^{-8}$ S · sq) and conducting (right, $\sigma_{2D} > 10^{-4}$ S · sq) limits are also shown in the insets. Scale bars in the insets are 200 nm.

Such a slow charging process owing to the small thickness of the gel layer has a direct consequence on our imaging experiment. For systems with a short response time,

one usually measures the properties under equilibrium by varying the external V_G, which is difficult to realize here. Alternatively, taking advantages of the slow relaxation in our ion-gel-gated device, we may freeze the ionic motion at intermediate states by cooling the device below T_g of the gel, and study the corresponding microscopic distribution of local conductance in the EDLT channel. In our experiment, a V_G of 2 V was applied at 230 K for various periods of waiting time until the desired I_{DS} was reached. The sample was then cooled down for T-dependent measurements, as plotted in Fig. 5.6a.

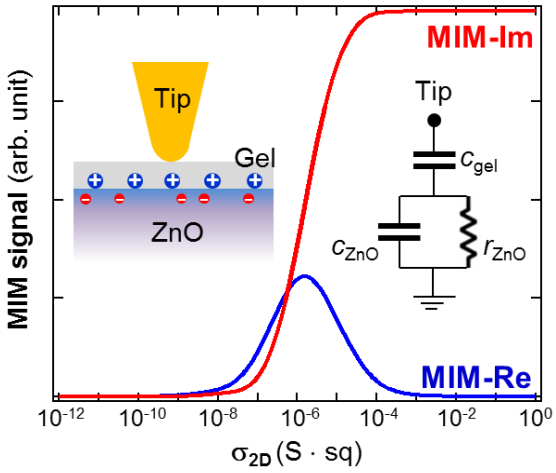

Figure 5.7: FEA simulation of the real (MIM-Re, blue) and imaginary (MIM-Im, red) components of the tip-sample admittance. The insets show the tip-sample configuration (left) and a lumped-element circuit model (right).

For each transport curve in Fig. 5.6a, we acquired the MIM images near the source/drain electrodes at T = 100 K (Fig. 5.6b). For simplicity, only the imaginary (MIM-Im) components of the data, which fully capture the local conductance information, are displayed in Fig. 5.6b. To obtain a quantitative understanding of the MIM images, we first present the finite-element analysis (FEA)[66] of the tip-sample interaction (Fig. 5.7), which converts the MIM-Im signals to the 2D sheet conductance σ_{2D}. For the simulation, the diameter of the focused ion-beam (FIB) deposited Pt tip is assumed to be 200 nm[66] and the

thickness of the ionic gel is 50 nm. The dielectric constant (ε) of ZnO is 8.5.[203] While little is known on the dielectric constant at 1 GHz for the ionic gel, we have assumed here $\varepsilon \sim 3$, similar to typical polymers. The simulation result does not depend strongly on the dielectric constant. The thickness of the ZnO surface inversion layer is assumed to be $d = 5$ nm and the 2D sheet conductance $\sigma_{2D} = \sigma_{3D} \cdot d$, where σ_{3D} is the 3D conductivity.

The real (MIM-Re) and imaginary (MIM-Im) parts of the effective tip admittance, which are directly proportional to the MIM signals, are shown in Fig. 5.7. The results can be qualitatively understood by the lumped-element circuit in the inset[66]. Note that this equivalent circuit seen by the tip is for the 1 GHz microwave excitation, which is totally different from the DC effective circuit in the inset of Fig. 5.5c. When the gel-ZnO interface is insulating, the resistance at the ZnO surface r_{ZnO} is very large and the tip is loaded by two geometric capacitors (c_{gel} and c_{ZnO}) in series. When the gel-ZnO interface is highly conducting, the small r_{ZnO} effectively shunts c_{ZnO}. In between these two limits, the MIM-Im signal increases monotonically as increasing σ_{2D} and the MIM-Re signal reaches a peak around $\sigma_{2D} = 1\ \mu S \cdot sq$. For simplicity, only the MIM-Im component is presented in the main text.

Note that due to the generally non-negligible contact resistance and the specific source/drain geometry, one cannot directly calculate σ_{2D} from the two-terminal conductance G_{DS} measured by transport. In the following analysis, we only use G_{DS} for an order-of-magnitude estimate when comparing with the σ_{2D} maps. When the EDLT interface is insulating, the quasi-static microwave electric fields can spread into the bulk of ZnO. On the other hand, a highly conductive EDLT interface can effectively screen the microwave electric fields, which are then terminated at the ZnO surface. Consequently, the tip-sample capacitance, which is proportional to the MIM-Im signal, depends strongly on σ_{2D}. As plotted in Fig. 5.6c, the MIM-Im signal remains low for small σ_{2D}, increases

monotonically with increasing σ2D between 0.01 and 100 μS · sq, and saturates for σ_{2D} above 100 μS · sq.

Of particular interest in Fig. 5.6b is the spatial evolution of local conductance as the EDLT channel was turned on. When a positive gate bias $V_G > V_{th}$ is applied, electrons in ZnO are first induced near source and drain by fringing fields from the cations accumulated on the electrodes. More cations are then attracted to these regions and the conductive area in ZnO gradually propagates into the entire channel. Such a process is vividly manifested by the MIM data. As G_{DS} at 100 K increased from 0 to 1.5 μS, the light blue regions in the false-colored map ($\sigma_{2D} \sim 1$ μS · sq) with higher MIM signals than the initial insulating state (dark blue, $\sigma_{2D} < 0.1$ μS · sq) appeared around the source/drain contacts and propagated toward the center of the channel. For G_{DS} = 3.4 μS, the highly conductive areas (orange to red, $\sigma_{2D} \sim 10$ μS · sq) originated from the two electrodes started to merge. At the highest G_{DS} of 10 μS in our experiment, the ZnO became highly conductive with $\sigma_{2D} > 10$ μS · sq everywhere inside the channel. We emphasize that, while the same process is ubiquitous in FETs, it is a rare occasion that the evolution can be imaged by scanning probe experiments, which provide not only strong support on the effectiveness of the ion-gel gating but also the real-space information of field-induced MITs.

5.2.4 Imaging Spatial Inhomogeneity of Channel Conductance

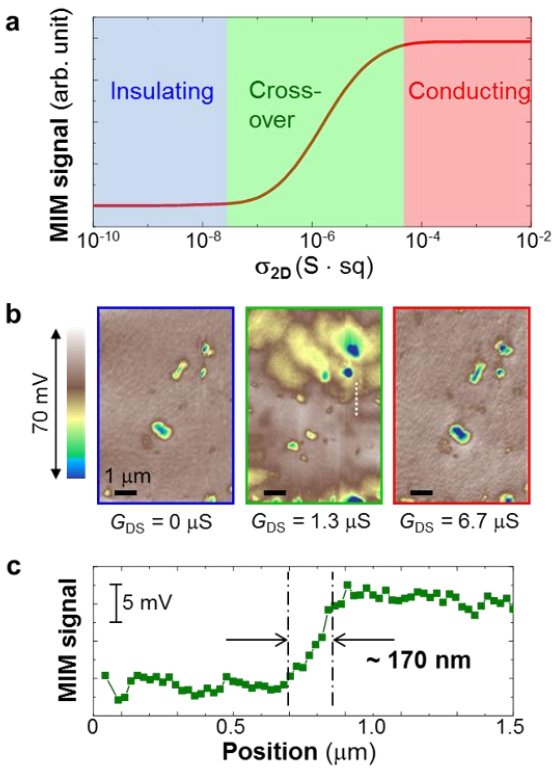

Figure 5.8: (a) Simulated results of MIM-Im signals as a function of σ_{2D}. The insulating, crossover, and conducting regimes are color-coded as blue, green, and red, respectively. (b) MIM images at three different G_{DS}'s after removing the background signals. Only several surface particles fixed in location were seen in the data when the ZnO channel was insulating (G_{DS} = 0 μS) or relatively conducting (G_{DS} = 6.7 μS). Fluctuation of the local conductance was observed when G_{DS} = 1.3 μS, which is likely within the crossover regime. All scale bars are 1 μm. (c) A line profile (white dotted line in b) in the crossover regime, showing a spatial resolution of about 170 nm for the MIM signals.

Evidence of the spatially inhomogeneous channel conductance has also been observed in our MIM experiment. As discussed before, the MIM-Im signals saturate for $\sigma_{2D} < 10^{-8}$ S · sq (insulating limit) and $\sigma_{2D} > 10^{-4}$ S · sq (conducting limit). Therefore, small fluctuations of local conductance are best visualized in the crossover regime (Fig. 5.8a) around $\sigma_{2D} = 10^{-6}$ S · sq. Fig. 5.8b shows the MIM images of a small area inside the channel

at three different G_{DS} values. For better visualization of the data, we remove the linear background that contains the absolute σ_{2D} information and display the relative variations of MIM signals with a false-color scale different from that used in Fig. 5.6. As shown in Fig. 5.8b, only several surface particles with low MIM signals were seen when the ZnO channel was insulating (G_{DS} = 0 μS). For an intermediate G_{DS} = 1.3 μS, which likely corresponds to an average σ_{2D} around 1 μS · sq in the channel, appreciable mesoscopic conductance fluctuation could be observed in the image. A line profile in Fig. 5.8c shows that a spatial resolution of ~ 170 nm can be obtained in this regime. Due to the saturation of MIM response at the conducting limit, the image acquired at G_{DS} = 6.7 μS again shows spatially uniform signals except for the same surface particles described before. Further experiments are needed to elucidate the origin and evolution of these non-uniform states. Nevertheless, the ability of resolving electrical inhomogeneity during the MITs will be particularly useful for the study of strongly correlated systems with nanoscale phase separation[191].

5.2.5 Local Conductance Profile under Different Drain-Source Voltages

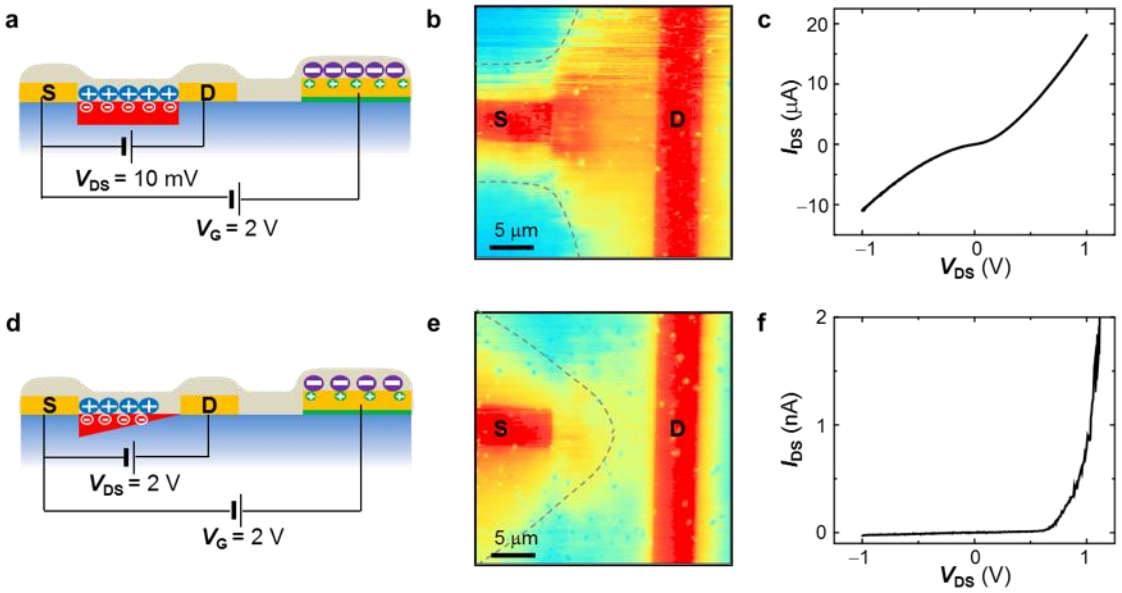

Figure 5.9: (a) Schematic of the EDLT and the charge distribution with a small V_{DS} = 10 mV. (b) Corresponding MIM image at 100 K around the source and drain electrodes. (c) I_{DS}-V_{DS} characteristics when the device under the bias condition in (a) was cooled to 100 K. (d – f) Same as (a – c) except that a large V_{DS} = 2 V was applied at 230 K before cooling down to 100 K for the MIM imaging and transport measurement. The dashed lines are guides to the eyes for the boundaries of conductive regions (yellow to red in the false color map). The scale bars are 5 μm.

In order to further demonstrate the MIM imaging on EDLTs, we studied the local conductance profile under two different V_{DS}'s applied across the channel. For a small V_{DS} of 10 mV in Fig. 5.9a, both the ions and induced electrons were evenly distributed in the channel, which agreed well with the MIM conductance map in Fig. 5.9b. In contrast, when a large bias V_{DS} = 2 V was applied at 230 K, an asymmetric lateral conductance distribution was set up along the channel (Fig. 5.9d), reminiscent of the textbook description of FETs in the saturation regime4. The corresponding MIM image in Fig. 5.9e clearly shows that the conductive regions were pushed away from the drain electrode. Interestingly, since ions are immobilized upon cooling through the glass transition, the conductance landscape in

the channel established by V_G and V_{DS} above T_g will be frozen in space below T_g. This effect could have a strong impact on the transport characteristics, as recently reported in EDLTs fabricated on MoS_2 and WSe_2 flakes[190, 204, 205]. For the bias configuration in Fig. 5.9a, appreciable I_{DS} in the μA range was measured (Fig. 5.9c) when V_{DS} was swept between –1 V and 1 V at 100 K, presumably due to the high σ_{2D} in between the source/drain contacts. On the other hand, when the channel was asymmetrically biased at 230 K (Fig. 5.9d), a strong rectifying behavior was seen in the I-V characteristics in Fig. 5.9f, again consistent with the low σ_{2D} near the drain contact.

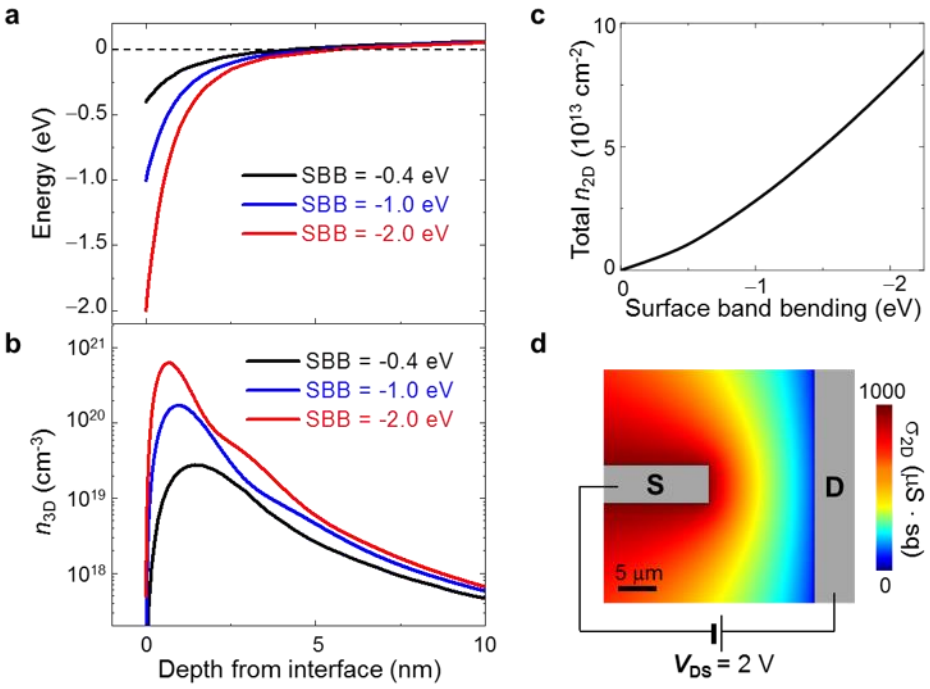

Figure 5.10: (a) Poisson-Schrodinger simulation result of the conduction band edge and (b) 3D electron density (n_{3D}) as a function of the depth from the EDLT interface. The results under three surface band bending (SBB) values of –0.4 eV, –1.0 eV, and –2.0 eV are plotted. (c) Total 2D density (n_{2D}) as a function of the SBB. (d) Simulated local conductance distribution induced by a large V_{DS} = 2 V across the EDLT channel.

The uneven distribution of σ_{2D} in the presence of a large V_{DS} can be understood by considering the local surface band bending (SBB) inside the channel. In Figs. 5.10a&b, we show the simulated depth profiles of the conduction band edge and total 3D electron density (n_{3D}) near the gel-ZnO interface with the SBB values of –0.4 eV, –1.0 eV, and –2.0 eV. Details of the Poisson-Schrodinger simulation[206] are provided as follows.

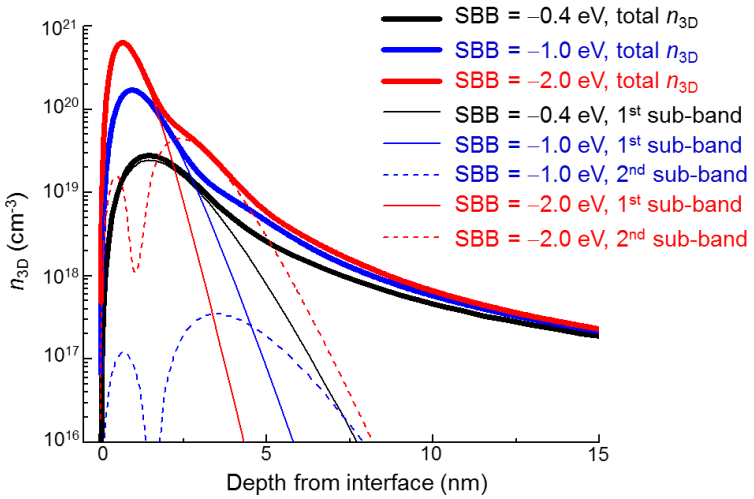

Figure 5.11: 3D electron density (n_{3D}) as a function of the depth from the EDLT interface. The dashed lines show the contribution from the 1st and 2nd sub-bands. The temperature is 300 K in this simulation.

Fig. 5.11 shows the results of the self-consistent Poisson-Schrodinger simulation using a non-uniform-meshed method described in Ref. 207. The mesh is denser close to the interface to enhance accuracy and efficiency. In order to simulate the experiment in a range of temperatures, Fermi-Dirac distribution is also incorporated, so that thermally excited electrons in sub-bands with energy higher than the Fermi level are also taken into account. The effective mass is adapted from Ref. 208 and the dielectric constant used is from Ref. 203. The solving range in depth is from 0 to 100 nm to ensure wide enough space for realistic solutions. We assume in the simulation a uniform electron doping at the level

of 1×10^{16} cm^{-3} in the whole sample. The effective 2D density (n_{2D}) as a function of various SBB values, as plotted in Fig. 5.10c, can then be calculated from the 3D density profile.

Based on the effective 2D density n_{2D} as a function of surface band bending (SBB), we can perform self-consistent modeling to obtain the conductance distribution around the source/drain electrodes. Here we assume a much larger gate area than the channel region such that V_G drops mostly on the gel-ZnO interface. In addition, the mobility of ZnO (100 $cm^2/V \cdot s$)[173], is assumed to be independent of the electron density. The conductance distribution affects the potential drop inside the channel, which results in different SBB at each point. The calculation runs iteratively until the change of potential distribution is less than 0.01 V. The resultant σ_{2D} map, as shown in Fig. 5.10d, agrees qualitatively with the MIM image in Fig. 5.9e. Aided by the numerical analysis described above, our MIM and transport data can be built on solid ground for future investigations of electronic phase transitions in novel material systems.

5.2.6 Conclusions

In summary, we have, for the first time, demonstrated the electrical imaging of local channel conductance in ion-gel-gated oxide EDLTs by cryogenic microwave impedance microscopy. We found that electrons induced by the electrostatic field effect propagate from the source and drain electrodes to the center of the channel. Small fluctuations of the local conductance were also observed during the insulator-metal transition. By applying a large source-drain bias above the glass transition temperature of the gel, an uneven conductance profile was established across the EDLT channel, which was visualized by the MIM and further investigated by transport measurements and numerical simulations. The combination of ultra-thin ion-gel gating and microwave microscopy paves the way for

studying the microscopic evolution of phase transitions in complex materials induced by electrostatic field effects.

Chapter 6: Conclusions and Outlook

In this dissertation, I briefly review the history of near-field scanning microwave microscopy (NSMM) and introduce the recently developed microwave impedance microscope (MIM). Detailed explanation of the MIM working principle is given using the example of standard MIM setup. I then discuss the development of MIM for quantitative measurement and broadband imaging, as well as implementation in cryogenic environment. With these instrumental advances, MIM is used to investigate a range of problems in condensed matter physics including emergent phenomena at ferroelectric domain walls and electrical inhomogeneity in nanodevices, providing rich scientific insights and suggesting great potential in technological application.

This dissertation has included my exploration of both scientific instrumentation of MIM and its applications in condensed matter physics research. The two parts are complementary to each other. Unexpected phenomena observed by MIM forced us to rethink what we have taken for granted about this technique and to go back to the fundamentals to explain the results. On the other hand, with better characterization and expanded capability of MIM, material properties can be quantitatively analyzed with higher precision and the scope of measurements will be broadened. It is very common in scientific research that an experimental technique reaches its full potential only after it is applied to multiple research directions. While we are inspired by all the discoveries with MIM, future improvement to the MIM technique can never be overemphasized.

In the future, several directions of MIM development are foreseeable. Tuning fork-based (TF-based) MIM will become a routine configuration for measurements with higher demand for quantitative analysis and in environments where optical feedback is hard to implement. The metal wire for the TF-based probe will be an additional degree of freedom

and exotic tip-sample interaction can be induced by tip materials with special properties such as magnetism and superconductivity. Broadband impedance imaging will be expanded to frequencies higher than 10 GHz utilizing microwave probes with lower loss, e.g. those built with monolithic metals, and lower than 1 MHz with improved detection electronics. More energy dissipation mechanisms and their spatial distribution can thus be investigated.

Based on MIM techniques either in use or under development, some scientific projects may lead to interesting discoveries. The emergent properties of ferroelectric domain walls (DWs) can be further explored using MIM at extreme conditions, such as low temperatures and high magnetic fields, to reveal details of the underlying mechanisms. Ferromagnetic DWs have been demonstrated in practical applications such as waveguides and nanoelectronic devices. Their electrical counterpart, especially those topologically protected DWs in multiferroic materials, if successfully incorporated into similar devices, will be best characterized and manipulated by MIM. As for encapsulated devices of novel materials, MIM will continue to provide crucial information by direct imaging of electrical conductance distribution.

Appendix A: Additional Data

A.1 DC CONDUCTIVITY OF H-*R*MnO$_3$

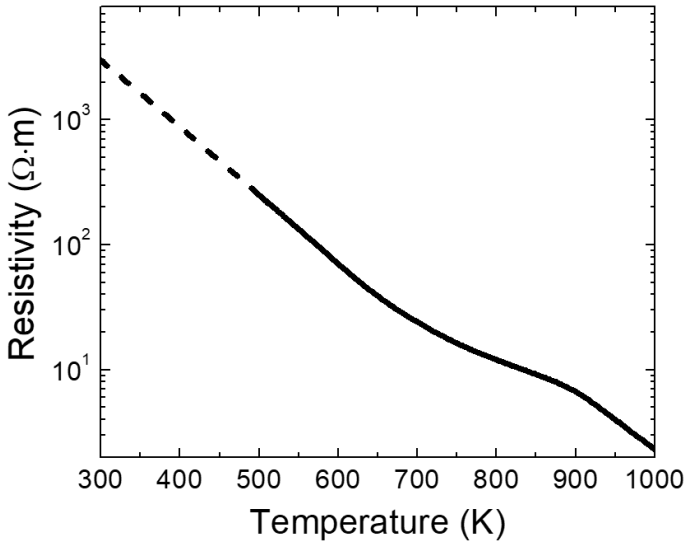

Figure A.1: Measurement of the dc resistivity of $YMnO_3$.

The dc resistivity of our single-crystal $YMnO_3$ samples is measured by a four-probe method using a Keithley source meter. The electrical contacts are made by curing the gold paste at high temperatures between 600 K and 800 K. The results from 1000 K to 500 K are shown in a solid curve because good Ohmic contacts are achieved in this temperature range. The kink at ~ 850 K is likely due to the formation of oxygen interstitials, which effectively dope the surface of the crystals[97]. For temperatures below 500 K, the contact resistance becomes substantially large and the I-V curves are no longer Ohmic-like. An extrapolation from ~ 600 K to ~ 300 K indicates a room-temperature dc resistivity of ~ 3×10^3 Ω·m, or the conductivity of ~ 0.3×10^{-3} S/m, which is consistent with the number (on the order of 10^{-3} S/m) quoted in the literature[77, 114, 115]. Future experiments using samples

with improved Ohmic contacts and instruments with higher input impedance may provide a more quantitative room-temperature dc resistivity of the $YMnO_3$ crystals.

References

1. E. H. Synge, The London, Edinburgh, and Dublin Philosophical Magazine and Journal of Science **6** (35), 356-362 (1928).
2. E. H. Synge, The London, Edinburgh, and Dublin Philosophical Magazine and Journal of Science **11** (68), 65-80 (1931).
3. R. F. Soohoo, Journal of Applied Physics **33** (3), 1276-1277 (1962).
4. E. A. Ash and G. Nicholls, Nature **237**, 510 (1972).
5. S. M. Anlage, V. V. Talanov and A. R. Schwartz, in *Scanning probe microscopy* (Springer, 2007), pp. 215-253.
6. B. Knoll and F. Keilmann, Optics Communications **162** (4), 177-181 (1999).
7. C. A. Bryant and J. B. Gunn, Review of Scientific Instruments **36** (11), 1614-1617 (1965).
8. C. P. Vlahacos, R. C. Black, S. M. Anlage, A. Amar and F. C. Wellstood, Applied Physics Letters **69** (21), 3272-3274 (1996).
9. D. E. Steinhauer, C. P. Vlahacos, F. C. Wellstood, S. M. Anlage, C. Canedy, R. Ramesh, A. Stanishevsky and J. Melngailis, Applied Physics Letters **75** (20), 3180-3182 (1999).
10. M. Fee, S. Chu and T. W. Hänsch, Optics Communications **69** (3), 219-224 (1989).
11. A. Imtiaz and S. M. Anlage, Ultramicroscopy **94** (3), 209-216 (2003).
12. A. Imtiaz, S. M. Anlage, J. D. Barry and J. Melngailis, Applied Physics Letters **90** (14), 143106 (2007).
13. M. Tabib-Azar, D. P. Su, A. Pohar, S. R. LeClair and G. Ponchak, Review of Scientific Instruments **70** (3), 1725-1729 (1999).
14. M. Tabib-Azar, D. Akinwande, G. E. Ponchak and S. R. LeClair, Review of Scientific Instruments **70** (7), 3083-3086 (1999).
15. V. V. Talanov and A. R. Schwartz, IEEE Transactions on Microwave Theory and Techniques **57** (5), 1224-1229 (2009).
16. S.-C. Lee, C. P. Vlahacos, B. J. Feenstra, A. Schwartz, D. E. Steinhauer, F. C. Wellstood and S. M. Anlage, Applied Physics Letters **77** (26), 4404-4406 (2000).
17. M. Tabib-Azar, P. S. Pathak, G. Ponchak and S. LeClair, Review of Scientific Instruments **70** (6), 2783-2792 (1999).
18. D. E. Steinhauer, C. P. Vlahacos, S. K. Dutta, F. C. Wellstood and S. M. Anlage, Applied Physics Letters **71** (12), 1736-1738 (1997).
19. T.-A. Massood and W. Yaqiang, IEEE Transactions on Microwave Theory and Techniques **52** (3), 971-979 (2004).
20. J. Jackson, *Classical Electrodynamics Third Edition*. (Wiley, 1998).
21. C. Gao and X. D. Xiang, Review of Scientific Instruments **69** (11), 3846-3851 (1998).
22. D. M. Pozar, *Microwave engineering*. (Fourth edition. Hoboken, NJ : Wiley, [2012] ©2012, 2012).

23. A. S. Thanawalla, S. K. Dutta, C. P. Vlahacos, D. E. Steinhauer, B. J. Feenstra, S. M. Anlage, F. C. Wellstood and R. B. Hammond, Applied Physics Letters **73** (17), 2491-2493 (1998).
24. M. Golosovsky and D. Davidov, Applied Physics Letters **68** (11), 1579-1581 (1996).
25. H. P. Huber, M. Moertelmaier, T. M. Wallis, C. J. Chiang, M. Hochleitner, A. Imtiaz, Y. J. Oh, K. Schilcher, M. Dieudonne, J. Smoliner, P. Hinterdorfer, S. J. Rosner, H. Tanbakuchi, P. Kabos and F. Kienberger, Review of Scientific Instruments **81** (11), 113701 (2010).
26. A. Gokirmak, D.-H. Wu, J. S. A. Bridgewater and S. M. Anlage, Review of Scientific Instruments **69** (9), 3410-3417 (1998).
27. J. Smoliner, H. P. Huber, M. Hochleitner, M. Moertelmaier and F. Kienberger, Journal of Applied Physics **108** (6), 064315 (2010).
28. S. K. Dutta, C. P. Vlahacos, D. E. Steinhauer, A. S. Thanawalla, B. J. Feenstra, F. C. Wellstood, S. M. Anlage and H. S. Newman, Applied Physics Letters **74** (1), 156-158 (1999).
29. R. Wang, F. Li and M. Tabib-Azar, Review of Scientific Instruments **76** (5), 054701 (2005).
30. A. Imtiaz and S. M. Anlage, Journal of Applied Physics **100** (4), 044304 (2006).
31. C. Gao, B. Hu, P. Zhang, M. Huang, W. Liu and I. Takeuchi, Applied Physics Letters **84** (23), 4647-4649 (2004).
32. M. Tabib-Azar and D. Akinwande, Review of Scientific Instruments **71** (3), 1460-1465 (2000).
33. M. Tabib-Azar, R. Ciocan, G. Ponchak and S. R. LeClair, Review of Scientific Instruments **70** (8), 3387-3390 (1999).
34. M. Tabib-Azar and B. Sutapun, Review of Scientific Instruments **70** (9), 3707-3713 (1999).
35. S. Hyun, J. H. Cho, A. Kim, J. Kim, T. Kim and K. Char, Applied Physics Letters **80** (9), 1574-1576 (2002).
36. H. P. Huber, I. Humer, M. Hochleitner, M. Fenner, M. Moertelmaier, C. Rankl, A. Imtiaz, T. M. Wallis, H. Tanbakuchi, P. Hinterdorfer, P. Kabos, J. Smoliner, J. J. Kopanski and F. Kienberger, Journal of Applied Physics **111** (1), 014301 (2012).
37. M. Abu-Teir, F. Sakran, M. Golosovsky, D. Davidov and A. Frenkel, Applied Physics Letters **80** (10), 1776-1778 (2002).
38. F. Sakran, A. Copty, M. Golosovsky, N. Bontemps, D. Davidov and A. Frenkel, Applied Physics Letters **82** (9), 1479-1481 (2003).
39. B. Friedman, M. A. Gaspar, S. Kalachikov, K. Lee, R. Levicky, G. Shen and H. Yoo, Journal of the American Chemical Society **127** (27), 9666-9667 (2005).
40. K. Lai, M. Nakamura, W. Kundhikanjana, M. Kawasaki, Y. Tokura, M. A. Kelly and Z.-X. Shen, Science **329** (5988), 190-193 (2010).
41. K. Lai, W. Kundhikanjana, M. A. Kelly, Z.-X. Shen, J. Shabani and M. Shayegan, Physical Review Letters **107** (17), 176809 (2011).

42. E. Y. Ma, Y.-T. Cui, K. Ueda, S. Tang, K. Chen, N. Tamura, P. M. Wu, J. Fujioka, Y. Tokura and Z.-X. Shen, Science **350** (6260), 538-541 (2015).
43. X. Wu, U. Petralanda, L. Zheng, Y. Ren, R. Hu, S.-W. Cheong, S. Artyukhin and K. Lai, Science Advances **3** (5) (2017).
44. K. Lai, H. Peng, W. Kundhikanjana, D. T. Schoen, C. Xie, S. Meister, Y. Cui, M. A. Kelly and Z.-X. Shen, Nano Letters **9** (3), 1265-1269 (2009).
45. J.-S. Kim, Y. Liu, W. Zhu, S. Kim, D. Wu, L. Tao, A. Dodabalapur, K. Lai and D. Akinwande, Scientific Reports **5**, 8989 (2015).
46. E. Seabron, S. MacLaren, X. Xie, S. V. Rotkin, J. A. Rogers and W. L. Wilson, ACS Nano **10** (1), 360-368 (2016).
47. S. Berweger, G. A. MacDonald, M. Yang, K. J. Coakley, J. J. Berry, K. Zhu, F. W. DelRio, T. M. Wallis and P. Kabos, Nano Letters **17** (3), 1796-1801 (2017).
48. Z. Chu, M. Yang, P. Schulz, D. Wu, X. Ma, E. Seifert, L. Sun, X. Li, K. Zhu and K. Lai, Nature Communications **8** (1), 2230 (2017).
49. M. Tuteja, P. Koirala, V. Palekis, S. MacLaren, C. S. Ferekides, R. W. Collins and A. A. Rockett, The Journal of Physical Chemistry C **120** (13), 7020-7024 (2016).
50. Y. Ren, H. Yuan, X. Wu, Z. Chen, Y. Iwasa, Y. Cui, H. Y. Hwang and K. Lai, Nano Letters **15** (7), 4730-4736 (2015).
51. D. Wu, X. Li, L. Luan, X. Wu, W. Li, M. N. Yogeesh, R. Ghosh, Z. Chu, D. Akinwande, Q. Niu and K. Lai, Proceedings of the National Academy of Sciences **113** (31), 8583-8588 (2016).
52. M. C. Biagi, R. Fabregas, G. Gramse, M. Van Der Hofstadt, A. Juárez, F. Kienberger, L. Fumagalli and G. Gomila, ACS Nano **10** (1), 280-288 (2016).
53. A. Tselev, J. Velmurugan, A. V. Ievlev, S. V. Kalinin and A. Kolmakov, ACS Nano **10** (3), 3562-3570 (2016).
54. Y. Yongliang, L. Keji, T. Qiaochu, K. Worasom, A. K. Michael, Z. Kun, S. Zhi-xun and L. Xinxin, Journal of Micromechanics and Microengineering **22** (11), 115040 (2012).
55. K. Lai, M. B. Ji, N. Leindecker, M. A. Kelly and Z. X. Shen, Review of Scientific Instruments **78** (6), 063702 (2007).
56. K. Lai, W. Kundhikanjana, M. A. Kelly and Z. X. Shen, Applied Physics Letters **93** (12), 123105 (2008).
57. C. Gao, T. Wei, F. Duewer, Y. Lu and X. D. Xiang, Applied Physics Letters **71** (13), 1872-1874 (1997).
58. D. W. van der Weide and P. Neuzil, Journal of Vacuum Science & Technology B: Microelectronics and Nanometer Structures Processing, Measurement, and Phenomena **14** (6), 4144-4147 (1996).
59. T. Morita and Y. Cho, Applied Physics Letters **84** (2), 257-259 (2004).
60. Y.-T. Cui, E. Y. Ma and Z.-X. Shen, Review of Scientific Instruments **87** (6), 063711 (2016).
61. K. Lai, W. Kundhikanjana, H. Peng, Y. Cui, M. A. Kelly and Z. X. Shen, Review of Scientific Instruments **80** (4), 043707 (2009).
62. F. J. Giessibl, Applied Physics Letters **73** (26), 3956-3958 (1998).

63. F. J. Giessibl, Reviews of Modern Physics **75** (3), 949-983 (2003).
64. E. Y. Ma, M. R. Calvo, J. Wang, B. Lian, M. Mühlbauer, C. Brüne, Y.-T. Cui, K. Lai, W. Kundhikanjana, Y. Yang, M. Baenninger, M. König, C. Ames, H. Buhmann, P. Leubner, L. W. Molenkamp, S.-C. Zhang, D. Goldhaber-Gordon, M. A. Kelly and Z.-X. Shen, Nature Communications **6**, 7252 (2015).
65. Y.-T. Cui, B. Wen, E. Y. Ma, G. Diankov, Z. Han, F. Amet, T. Taniguchi, K. Watanabe, D. Goldhaber-Gordon, C. R. Dean and Z.-X. Shen, Physical Review Letters **117** (18), 186601 (2016).
66. K. Lai, W. Kundhikanjana, M. Kelly and Z. X. Shen, Review of Scientific Instruments **79** (6), 063703 (2008).
67. J. Rychen, T. Ihn, P. Studerus, A. Herrmann, K. Ensslin, H. J. Hug, P. J. A. van Schendel and H. J. Güntherodt, Applied Surface Science **157** (4), 290-294 (2000).
68. M. Jaafar, D. Martínez-Martín, M. Cuenca, J. Melcher, A. Raman and J. Gómez-Herrero, Beilstein Journal of Nanotechnology **3**, 336-344 (2012).
69. E. Inger, W. Erik, C. Dan, O. Håkan and O. Eva, Measurement Science and Technology **10** (1), 11 (1999).
70. I. H. Musselman, P. A. Peterson and P. E. Russell, Precision Engineering **12** (1), 3-6 (1990).
71. Z. Wei, E. Y. Ma, Y.-T. Cui, S. Johnston, Y. Yang, K. Agarwal, M. A. Kelly, Z.-X. Shen and X. Chen, Review of Scientific Instruments **87** (9), 094701 (2016).
72. A. Tselev, S. M. Anlage, Z. Ma and J. Melngailis, Review of Scientific Instruments **78** (4), 044701 (2007).
73. J. Valasek, Physical Review **17** (4), 475-481 (1921).
74. N. A. Spaldin and M. Fiebig, Science **309** (5733), 391 (2005).
75. N. A. Hill, The Journal of Physical Chemistry B **104** (29), 6694-6709 (2000).
76. B. B. Van Aken, T. T. M. Palstra, A. Filippetti and N. A. Spaldin, Nature Materials **3**, 164 (2004).
77. T. Choi, Y. Horibe, H. Yi, Y. Choi, W. Wu and S.-W. Cheong, Nature materials **9** (3), 253 (2010).
78. Y. Kumagai and N. A. Spaldin, Nature communications **4**, 1540 (2013).
79. W. Wang, J. Zhao, W. Wang, Z. Gai, N. Balke, M. Chi, H. N. Lee, W. Tian, L. Zhu, X. Cheng, D. J. Keavney, J. Yi, T. Z. Ward, P. C. Snijders, H. M. Christen, W. Wu, J. Shen and X. Xu, Physical Review Letters **110** (23), 237601 (2013).
80. S. M. Disseler, X. Luo, B. Gao, Y. S. Oh, R. Hu, Y. Wang, D. Quintana, A. Zhang, Q. Huang, J. Lau, R. Paul, J. W. Lynn, S.-W. Cheong and W. Ratcliff, Physical Review B **92** (5), 054435 (2015).
81. L. Lin, H. M. Zhang, M. F. Liu, S. Shen, S. Zhou, D. Li, X. Wang, Z. B. Yan, Z. D. Zhang, J. Zhao, S. Dong and J. M. Liu, Physical Review B **93** (7), 075146 (2016).
82. J. A. Mundy, C. M. Brooks, M. E. Holtz, J. A. Moyer, H. Das, A. F. Rébola, J. T. Heron, J. D. Clarkson, S. M. Disseler, Z. Liu, A. Farhan, R. Held, R. Hovden, E. Padgett, Q. Mao, H. Paik, R. Misra, L. F. Kourkoutis, E. Arenholz, A. Scholl, J. A. Borchers, W. D. Ratcliff, R. Ramesh, C. J. Fennie, P. Schiffer, D. A. Muller and D. G. Schlom, Nature **537**, 523 (2016).

83. S. Song, H. Han, H. M. Jang, Y. T. Kim, N. S. Lee, C. G. Park, J. R. Kim, T. W. Noh and J. F. Scott, Advanced Materials **28** (34), 7430-7435 (2016).
84. M. Fiebig, T. Lottermoser, D. Meier and M. Trassin, Nature Reviews Materials **1**, 16046 (2016).
85. J. Seidel, L. W. Martin, Q. He, Q. Zhan, Y.-H. Chu, A. Rother, M. Hawkridge, P. Maksymovych, P. Yu and M. Gajek, Nature materials **8** (3), 229 (2009).
86. M. Schröder, A. Haußmann, A. Thiessen, E. Soergel, T. Woike and L. M. Eng, Advanced Functional Materials **22** (18), 3936-3944 (2012).
87. J. Guyonnet, I. Gaponenko, S. Gariglio and P. Paruch, Advanced Materials **23** (45), 5377-5382 (2011).
88. R. K. Vasudevan, W. Wu, J. R. Guest, A. P. Baddorf, A. N. Morozovska, E. A. Eliseev, N. Balke, V. Nagarajan, P. Maksymovych and S. V. Kalinin, Advanced Functional Materials **23** (20), 2592-2616 (2013).
89. T. Sluka, A. K. Tagantsev, P. Bednyakov and N. Setter, Nature communications **4**, 1808 (2013).
90. Y. S. Oh, X. Luo, F.-T. Huang, Y. Wang and S.-W. Cheong, Nature materials **14** (4), 407 (2015).
91. A. Crassous, T. Sluka, A. K. Tagantsev and N. Setter, Nature nanotechnology **10** (7), 614 (2015).
92. M. Y. Gureev, A. K. Tagantsev and N. Setter, Physical Review B **83** (18), 184104 (2011).
93. E. Eliseev, A. Morozovska, G. Svechnikov, V. Gopalan and V. Y. Shur, Physical Review B **83** (23), 235313 (2011).
94. E. A. Eliseev, A. N. Morozovska, Y. Gu, A. Y. Borisevich, L.-Q. Chen, V. Gopalan and S. V. Kalinin, Physical Review B **86** (8), 085416 (2012).
95. Y. Du, X. Wang, D. Chen, S. Dou, Z. Cheng, M. Higgins, G. Wallace and J. Wang, Applied Physics Letters **99** (25), 252107 (2011).
96. Y. Du, X. Wang, D. Chen, Y. Yu, W. Hao, Z. Cheng and S. X. Dou, Physical Chemistry Chemical Physics **15** (46), 20010-20015 (2013).
97. S. H. Skjærvø, E. T. Wefring, S. K. Nesdal, N. H. Gaukås, G. H. Olsen, J. Glaum, T. Tybell and S. M. Selbach, Nature communications **7**, 13745 (2016).
98. J. Seidel, P. Maksymovych, Y. Batra, A. Katan, S.-Y. Yang, Q. He, A. P. Baddorf, S. V. Kalinin, C.-H. Yang and J.-C. Yang, Physical Review Letters **105** (19), 197603 (2010).
99. S. S. P. Parkin, M. Hayashi and L. Thomas, Science **320** (5873), 190 (2008).
100. M. Hayashi, L. Thomas, R. Moriya, C. Rettner and S. S. P. Parkin, Science **320** (5873), 209 (2008).
101. E. Saitoh, H. Miyajima, T. Yamaoka and G. Tatara, Nature **432**, 203 (2004).
102. Y.-H. Shin, I. Grinberg, I.-W. Chen and A. M. Rappe, Nature **449** (7164), 881 (2007).
103. S. V. Kalinin, A. N. Morozovska, L. Q. Chen and B. J. Rodriguez, Reports on Progress in Physics **73** (5), 056502 (2010).

104. C. T. Nelson, P. Gao, J. R. Jokisaari, C. Heikes, C. Adamo, A. Melville, S.-H. Baek, C. M. Folkman, B. Winchester and Y. Gu, Science **334** (6058), 968-971 (2011).
105. C. Kittel, Physical Review **83** (2), 458 (1951).
106. M. Maglione, R. Böhmer, A. Loidl and U. Höchli, Physical Review B **40** (16), 11441 (1989).
107. G. Arlt, U. Böttger and S. Witte, Annalen der Physik **506** (7‐8), 578-588 (1994).
108. A. Sidorkin, Journal of applied physics **83** (7), 3762-3768 (1998).
109. J. d. L. S. Guerra and J. Eiras, Journal of Physics: Condensed Matter **19** (38), 386217 (2007).
110. V. Porokhonskyy, L. Jin and D. Damjanovic, Applied Physics Letters **94** (21), 212906 (2009).
111. F. Kremer and A. Schönhals, *Broadband dielectric spectroscopy*. (Springer, Berlin; New York, 2003).
112. S. Gevorgian, (2009).
113. G. Catalan, J. Seidel, R. Ramesh and J. F. Scott, Reviews of Modern Physics **84** (1), 119-156 (2012).
114. G. S. Rao, B. Wanklyn and C. Rao, in *Solid State Chemistry: Selected Papers of CNR Rao* (World Scientific, 1995), pp. 365-378.
115. W. Wu, J. Guest, Y. Horibe, S. Park, T. Choi, S.-W. Cheong and M. Bode, Physical review letters **104** (21), 217601 (2010).
116. K. Lai, W. Kundhikanjana, M. A. Kelly and Z.-X. Shen, Applied Nanoscience **1** (1), 13-18 (2011).
117. Q. Zhang, G. Tan, L. Gu, Y. Yao, C. Jin, Y. Wang, X. Duan and R. Yu, Scientific reports **3**, 2741 (2013).
118. S. Chae, Y. Horibe, D. Jeong, N. Lee, K. Iida, M. Tanimura and S.-W. Cheong, Physical review letters **110** (16), 167601 (2013).
119. H. Myung‐Geun, Z. Yimei, W. Lijun, A. Toshihiro, V. Vyacheslav, W. Xueyun, C. S. Chul, O. Y. Seok and C. Sang‐Wook, Advanced Materials **25** (17), 2415-2421 (2013).
120. D. Tomuta, S. Ramakrishnan, G. Nieuwenhuys and J. Mydosh, Journal of Physics: Condensed Matter **13** (20), 4543 (2001).
121. A. K. Jonscher, Journal of Physics D: Applied Physics **32** (14), R57 (1999).
122. A. Tselev, P. Yu, Y. Cao, L. R. Dedon, L. W. Martin, S. V. Kalinin and P. Maksymovych, Nature communications **7**, 11630 (2016).
123. D. Meier, J. Seidel, A. Cano, K. Delaney, Y. Kumagai, M. Mostovoy, N. A. Spaldin, R. Ramesh and M. Fiebig, Nature materials **11** (4), 284 (2012).
124. W. Wu, Y. Horibe, N. Lee, S.-W. Cheong and J. Guest, Physical review letters **108** (7), 077203 (2012).
125. S.-Z. Lin, X. Wang, Y. Kamiya, G.-W. Chern, F. Fan, D. Fan, B. Casas, Y. Liu, V. Kiryukhin and W. H. Zurek, Nature Physics **10** (12), 970 (2014).
126. S. Artyukhin, K. T. Delaney, N. A. Spaldin and M. Mostovoy, Nature materials **13** (1), 42 (2014).
127. K. Z. Rushchanskii and M. Ležaić, Ferroelectrics **426** (1), 90-96 (2012).

128. R. Peierls, Proceedings of the Physical Society **52** (1), 34 (1940).
129. F. Nabarro, Proceedings of the Physical Society **59** (2), 256 (1947).
130. M. Methfessel, Physical Review B **38** (2), 1537 (1988).
131. X.-B. Chen, N. T. M. Hien, K. Han, J.-Y. Nam, N. T. Huyen, S.-I. Shin, X. Wang, S. Cheong, D. Lee and T. Noh, Scientific reports **5**, 13366 (2015).
132. P. E. Blöchl, Physical review B **50** (24), 17953 (1994).
133. P. Giannozzi, S. Baroni, N. Bonini, M. Calandra, R. Car, C. Cavazzoni, D. Ceresoli, G. L. Chiarotti, M. Cococcioni and I. Dabo, Journal of physics: Condensed matter **21** (39), 395502 (2009).
134. C. J. Fennie and K. M. Rabe, Physical Review B **72** (10), 100103 (2005).
135. F. Garcia-Sanchez, P. Borys, R. Soucaille, J.-P. Adam, R. L. Stamps and J.-V. Kim, Physical review letters **114** (24), 247206 (2015).
136. S. Datta, *Surface acoustic wave devices*. (Prentice-Hall, Englewood Cliffs, N.J., 1986).
137. J. A. Sulpizio, S. Ilani, P. Irvin and J. Levy, Annual Review of Materials Research **44**, 117-149 (2014).
138. A. Ohtomo and H. Y. Hwang, Nature **427**, 423 (2004).
139. A. Brinkman, M. Huijben, M. Van Zalk, J. Huijben, U. Zeitler, J. Maan, W. G. van der Wiel, G. Rijnders, D. H. Blank and H. Hilgenkamp, Nature materials **6** (7), 493 (2007).
140. N. Reyren, S. Thiel, A. D. Caviglia, L. Fitting Kourkoutis, G. Hammer, C. Richter, C. W. Schneider, T. Kopp, A. S. Rüetschi, D. Jaccard, M. Gabay, D. A. Muller, J. M. Triscone and J. Mannhart, Science **317**, 1196 (2007).
141. L. Li, C. Richter, J. Mannhart and R. Ashoori, Nature physics **7** (10), 762 (2011).
142. J. A. Bert, B. Kalisky, C. Bell, M. Kim, Y. Hikita, H. Y. Hwang and K. A. Moler, Nature physics **7** (10), 767 (2011).
143. S. Thiel, G. Hammerl, A. Schmehl, C. W. Schneider and J. Mannhart, Science **313**, 1942 (2006).
144. C. Cen, S. Thiel, G. Hammerl, C. Schneider, K. Andersen, C. Hellberg, J. Mannhart and J. Levy, Nature materials **7** (4), 298 (2008).
145. C. Cen, S. Thiel, J. Mannhart and J. Levy, Science **323**, 1026 (2009).
146. P. Irvin, M. Huang, F. Wong, T. Sanders, Y. Suzuki and J. Levy, Applied Physics Letters **102** (10), 103113 (2013).
147. P. Irvin, Y. Ma, D. F. Bogorin, C. Cen, C. W. Bark, C. M. Folkman, C.-B. Eom and J. Levy, Nature Photonics **4** (12), 849 (2010).
148. G. Cheng, P. F. Siles, F. Bi, C. Cen, D. F. Bogorin, C. W. Bark, C. M. Folkman, J.-W. Park, C.-B. Eom and G. Medeiros-Ribeiro, Nature Nanotechnology **6** (6), 343 (2011).
149. G. Cheng, M. Tomczyk, S. Lu, J. P. Veazey, M. Huang, P. Irvin, S. Ryu, H. Lee, C. B. Eom, C. S. Hellberg and J. Levy, Nature **521**, 196 (2015).
150. M. Tomczyk, G. Cheng, H. Lee, S. Lu, A. Annadi, J. P. Veazey, M. Huang, P. Irvin, S. Ryu and C.-B. Eom, Physical review letters **117** (9), 096801 (2016).
151. M. Basletic, J.-L. Maurice, C. Carrétéro, G. Herranz, O. Copie, M. Bibes, É. Jacquet, K. Bouzehouane, S. Fusil and A. Barthélémy, Nature materials **7** (8), 621 (2008).

152. Y. Xie, C. Bell, T. Yajima, Y. Hikita and H. Y. Hwang, Nano letters **10** (7), 2588-2591 (2010).
153. C. Bark, P. Sharma, Y. Wang, S. H. Baek, S. Lee, S. Ryu, C. Folkman, T. R. Paudel, A. Kumar and S. V. Kalinin, Nano letters **12** (4), 1765-1771 (2012).
154. M. Huang, F. Bi, S. Ryu, C.-B. Eom, P. Irvin and J. Levy, APL Materials **1** (5), 052110 (2013).
155. M. Honig, J. A. Sulpizio, J. Drori, A. Joshua, E. Zeldov and S. Ilani, Nature materials **12** (12), 1112 (2013).
156. B. Kalisky, E. M. Spanton, H. Noad, J. R. Kirtley, K. C. Nowack, C. Bell, H. K. Sato, M. Hosoda, Y. Xie and Y. Hikita, Nature materials **12** (12), 1091 (2013).
157. F. Bi, D. F. Bogorin, C. Cen, C. W. Bark, J.-W. Park, C.-B. Eom and J. Levy, Applied Physics Letters **97** (17), 173110 (2010).
158. M. Andrä, F. Gunkel, C. Bäumer, C. Xu, R. Dittmann and R. Waser, Nanoscale **7** (34), 14351-14357 (2015).
159. J. Robertson, The European Physical Journal-Applied Physics **28** (3), 265-291 (2004).
160. J. Mannhart and D. G. Schlom, Science **327**, 1607 (2010).
161. H. Y. Hwang, Y. Iwasa, M. Kawasaki, B. Keimer, N. Nagaosa and Y. Tokura, Nature materials **11** (2), 103 (2012).
162. M. Imada, A. Fujimori and Y. Tokura, Reviews of modern physics **70** (4), 1039 (1998).
163. P. A. Lee, N. Nagaosa and X.-G. Wen, Reviews of modern physics **78** (1), 17 (2006).
164. M. B. Salamon and M. Jaime, Reviews of Modern Physics **73** (3), 583 (2001).
165. S. M. Sze and K. K. Ng, *Physics of semiconductor devices*. (Wiley-Interscience, Hoboken, NJ, 2006).
166. R. Misra, M. McCarthy and A. F. Hebard, Applied Physics Letters **90** (5), 052905 (2007).
167. H. Shimotani, H. Asanuma, A. Tsukazaki, A. Ohtomo, M. Kawasaki and Y. Iwasa, Applied Physics Letters **91** (8), 082106 (2007).
168. P. Simon and Y. Gogotsi, Nature materials **7** (11), 845 (2008).
169. J. H. Cho, J. Lee, Y. He, B. Kim, T. P. Lodge and C. D. Frisbie, Advanced materials **20** (4), 686-690 (2008).
170. J. H. Cho, J. Lee, Y. Xia, B. Kim, Y. He, M. J. Renn, T. P. Lodge and C. D. Frisbie, Nature materials **7** (11), 900 (2008).
171. Y. Yomogida, J. Pu, H. Shimotani, S. Ono, S. Hotta, Y. Iwasa and T. Takenobu, Advanced Materials **24** (32), 4392-4397 (2012).
172. K. H. Lee, M. S. Kang, S. Zhang, Y. Gu, T. P. Lodge and C. D. Frisbie, Advanced Materials **24** (32), 4457-4462 (2012).
173. H. Yuan, H. Shimotani, A. Tsukazaki, A. Ohtomo, M. Kawasaki and Y. Iwasa, Advanced Functional Materials **19** (7), 1046-1053 (2009).
174. C. H. Ahn, J. M. Triscone and J. Mannhart, Nature **424**, 1015 (2003).

175. C. Ahn, A. Bhattacharya, M. Di Ventra, J. Eckstein, C. D. Frisbie, M. Gershenson, A. Goldman, I. Inoue, J. Mannhart and A. J. Millis, Reviews of Modern Physics **78** (4), 1185 (2006).
176. A. S. Dhoot, C. Israel, X. Moya, N. D. Mathur and R. H. Friend, Physical review letters **102** (13), 136402 (2009).
177. M. Nakano, K. Shibuya, D. Okuyama, T. Hatano, S. Ono, M. Kawasaki, Y. Iwasa and Y. Tokura, Nature **487**, 459 (2012).
178. J. Jeong, N. Aetukuri, T. Graf, T. D. Schladt, M. G. Samant and S. S. P. Parkin, Science **339**, 1402 (2013).
179. Y. Yamada, K. Ueno, T. Fukumura, H. T. Yuan, H. Shimotani, Y. Iwasa, L. Gu, S. Tsukimoto, Y. Ikuhara and M. Kawasaki, Science **332**, 1065 (2011).
180. J. G. Checkelsky, J. Ye, Y. Onose, Y. Iwasa and Y. Tokura, Nature Physics **8** (10), 729 (2012).
181. K. Ueno, H. Shimotani, H. Yuan, J. Ye, M. Kawasaki and Y. Iwasa, Journal of the Physical Society of Japan **83** (3), 032001 (2014).
182. K. Ueno, S. Nakamura, H. Shimotani, A. Ohtomo, N. Kimura, T. Nojima, H. Aoki, Y. Iwasa and M. Kawasaki, Nature materials **7** (11), 855 (2008).
183. J. Ye, S. Inoue, K. Kobayashi, Y. Kasahara, H. Yuan, H. Shimotani and Y. Iwasa, Nature materials **9** (2), 125 (2010).
184. K. Ueno, S. Nakamura, H. Shimotani, H. Yuan, N. Kimura, T. Nojima, H. Aoki, Y. Iwasa and M. Kawasaki, Nature nanotechnology **6** (7), 408 (2011).
185. A. T. Bollinger, G. Dubuis, J. Yoon, D. Pavuna, J. Misewich and I. Bozovic, Nature **472**, 458 (2011).
186. Y. Lee, C. Clement, J. Hellerstedt, J. Kinney, L. Kinnischtzke, X. Leng, S. Snyder and A. Goldman, Physical Review Letters **106** (13), 136809 (2011).
187. D. Kim, S. Cho, N. P. Butch, P. Syers, K. Kirshenbaum, S. Adam, J. Paglione and M. S. Fuhrer, Nature Physics **8** (6), 459 (2012).
188. C. Yin, H. Yuan, X. Wang, S. Liu, S. Zhang, N. Tang, F. Xu, Z. Chen, H. Shimotani and Y. Iwasa, Nano letters **13** (5), 2024-2029 (2013).
189. H. Yuan, X. Wang, B. Lian, H. Zhang, X. Fang, B. Shen, G. Xu, Y. Xu, S.-C. Zhang and H. Y. Hwang, Nature nanotechnology **9** (10), 851 (2014).
190. Y. Zhang, T. Oka, R. Suzuki, J. Ye and Y. Iwasa, Science **344** (6185), 725-728 (2014).
191. E. Dagotto, *Nanoscale phase separation and colossal magnetoresistance : the physics of manganites and related compounds*. (Springer, Berlin; London, 2011).
192. J. Martin, N. Akerman, G. Ulbricht, T. Lohmann, J. v. Smet, K. Von Klitzing and A. Yacoby, Nature Physics **4** (2), 144 (2008).
193. H. Beidenkopf, P. Roushan, J. Seo, L. Gorman, I. Drozdov, Y. San Hor, R. J. Cava and A. Yazdani, Nature Physics **7** (12), 939 (2011).
194. C. Mann, D. West, I. Miotkowski, Y. P. Chen, S. Zhang and C.-K. Shih, Nature communications **4**, 2277 (2013).

195. D. A. Bonnell, D. N. Basov, M. Bode, U. Diebold, S. V. Kalinin, V. Madhavan, L. Novotny, M. Salmeron, U. D. Schwarz and P. S. Weiss, Reviews of Modern Physics **84** (3), 1343 (2012).
196. L. Bürgi, H. Sirringhaus and R. Friend, Applied Physics Letters **80** (16), 2913-2915 (2002).
197. E. M. Muller and J. A. Marohn, Advanced Materials **17** (11), 1410-1414 (2005).
198. C. Sciascia, N. Martino, T. Schuettfort, B. Watts, G. Grancini, M. R. Antognazza, M. Zavelani‐Rossi, C. R. McNeill and M. Caironi, Advanced Materials **23** (43), 5086-5090 (2011).
199. J. Zaumseil, F. Jakubka, M. Wang and F. Gannott, The Journal of Physical Chemistry C **117** (49), 26361-26370 (2013).
200. W. Kundhikanjana, K. Lai, M. A. Kelly and Z.-X. Shen, Review of Scientific Instruments **82** (3), 033705 (2011).
201. H. Yuan, H. Shimotani, A. Tsukazaki, A. Ohtomo, M. Kawasaki and Y. Iwasa, Journal of the American Chemical Society **132** (19), 6672-6678 (2010).
202. H. Yuan, H. Shimotani, J. Ye, S. Yoon, H. Aliah, A. Tsukazaki, M. Kawasaki and Y. Iwasa, Journal of the American Chemical Society **132** (51), 18402-18407 (2010).
203. Y. Hisashi and A. Sadao, Japanese Journal of Applied Physics **36** (10R), 6237 (1997).
204. Y. Zhang, J. Ye, Y. Yomogida, T. Takenobu and Y. Iwasa, Nano letters **13** (7), 3023-3028 (2013).
205. H. Yuan, M. S. Bahramy, K. Morimoto, S. Wu, K. Nomura, B.-J. Yang, H. Shimotani, R. Suzuki, M. Toh and C. Kloc, Nature Physics **9** (9), 563 (2013).
206. I. H. Tan, G. Snider, L. Chang and E. Hu, Journal of applied physics **68** (8), 4071-4076 (1990).
207. I. H. Tan, G. L. Snider, L. D. Chang and E. L. Hu, Journal of Applied Physics **68** (8), 4071-4076 (1990).
208. A. Tsukazaki, A. Ohtomo, T. Kita, Y. Ohno, H. Ohno and M. Kawasaki, Science **315** (5817), 1388-1391 (2007).